New Jersey Institute of Technology

Digital Commons @ NJIT

Summer 8-31-2006

Earthshine : Photometry, modeling, and spectral observations

Jeffrey Patrick Hickey
New Jersey Institute of Technology

ABSTRACT

EARTHSHINE: PHOTOMETRY, MODELING, AND SPECTRAL OBSERVATIONS

by
Jeffrey Patrick Hickey

The Earthshine group has been making sustained observations of the Earthshine from Big Bear Solar Observatory in California since late 1998. There have also been intermittent observations from 1994-5. High and low resolution Earthshine spectral observations have also been under taken at Palomar Observatory since 1999. The group has re-invigorated and modernized a nearly forgotten way of measuring the Earth's albedo, and hence its energy balance, previously studied by Danjon (and his followers) for about twenty-five years early in the last century, using their observations of the Earthshine from France. This is an overview paper covering observations, reductions, simulations, and analysis, of the Earth's reflectance from photometric and spectral observations of the moon. The Earthshine group developed a modern method of measuring, instantaneously, the large scale reflectance of the Earth. From California an observer sees the moon reflecting sunlight from the third of the Earth to the west in the evening (before midnight) which is during the moon's rising phase and from the third of the Earth to the east in the morning (after midnight) which is during the moon's declining phase. The group has precisely measured the scattering from the moon, as a function of lunar phase, which enables the measurement, in a typical night's observations, the Earth's reflectance to an accuracy of 2.0% (equivalent to measuring the Earth's emission temperature to ~0.8 K). The group identified the lunar phase function as the major source of discrepancy between Danjon's estimates of the albedo

and more recent measurements. The albedo variation is due to the interplay of cloud cover and the different landscapes.

EARTHSHINE: PHOTOMETRY, MODELING, AND SPECTRAL OBSERVATIONS

by
Jeffrey Patrick Hickey

A Thesis
Submitted to the Faculty of
New Jersey Institute of Technology
in Partial Fulfillment of the Requirements for the Degree of
Master of Science in Applied Physics

Federated Physics Department

August 2006

APPROVAL PAGE

EARTHSHINE: PHOTOMETRY, MODELING, AND SPECTRAL OBSERVATIONS

Jeffrey Patrick Hickey

Dr. Philip R. Goode, Dissertation Advisor   Date
Distinguished Professor of Physics, NJIT

Dr. Haimin Wang, Committee Member   Date
Distinguished Professor of Physics, NJIT

Dr. Carsten J. Denker, Committee Member   Date
Assistant Professor of Physics, NJIT

Blank Page

BIOGRAPHICAL SKETCH

Author: Jeffrey Patrick Hickey

Degree: Master of Science

Date: August 2006

Undergraduate and Graduate Education:

- Master of Science in Applied Physics,
  New Jersey Institute of Technology, Newark, NJ, 2006

- Master of Science in Astronomy,
  San Diego State University, San Diego, CA., 1987

- Bachelor of Science in Astronomy,
  San Diego State University, San Diego, CA., 1980

Major: Applied Physics

Presentations and Publications:

Goode, P.R., J. Qiu, V. Yurchyshyn, **J. Hickey**, M.C. Chu, E. Kolbe, C.T. Brown, and
S.E. Koonin.
> "Earthshine observations of the Earth's reflectance", Geophys. Res. Lett., 28 (9),
> 1671-1674, 2001.

Qiu, J., P.R. Goode, E. Pallé, V. Yurchyshyn, **J. Hickey**, P. Montañés Rodriguez, M.C.
Chu, E. Kolbe, C.T. Brown, and S.E. Koonin,
> "Earthshine and the Earth's albedo I: Precise and large-scale nightly
> measurements", J. Geophys. Res., 108, ACL 12-1, 2003.

Pallé, E., P.R. Goode., V. Yurchyshyn, J. Qiu, **J. Hickey**, P. Montañés Rodriguez, M.C.
Chu, E. Kolbe, C.T. Brown, and S.E. Koonin,
> "Earthshine and the Earth's albedo II: Observations and simulations over three
> years", J. Geophys. Res., 108, ACL 13-1, 2003.

For my Mother and Father who made this possible

ACKNOWLEDGMENT

TABLE OF CONTENTS

TABLE OF CONTENTS
(Continued)

LIST OF FIGURES

LIST OF FIGURES
(Continued)

CHAPTER 1

INTRODUCTION

It is important to know whether there is an on-going global change in the Earth's climate. To answer this, one needs precise, global/integrated measures of relevant quantities. The Earth's climate is driven by the net sunlight deposited in the terrestrial atmosphere, and is critically sensitive to the solar irradiance and the Earth's albedo. Precise measurements of the solar irradiance have been made by various satellites and by using ground-based proxies (for a review, see Fröhlich, 2000, and references therein). The spectrum of efforts to determine the Earth's global albedo is not so rich. There have been efforts using systems of satellites (Buratti et al., 1996, and references therein), but virtually no efforts from the ground. Nonetheless, the Earth's energy balance is determined in large part by its global albedo—the fraction of the incident sunlight that is directly reflected back into space without altering the internal energy budget of the atmosphere. The Earth's surface, aerosols in the atmosphere and clouds all reflect some of the incoming solar short-wavelength radiation, preventing that energy from warming the planet. Further, about 13% of the solar radiation incident on the atmosphere is Rayleigh scattered, half of this reaching the Earth's surface as diffuse radiation and the other half being returned to space (Houghton, 2002). Short-wavelength radiation, usually defined as having wavelengths between 0.15 and 4.0 μm, includes about 99% of the sun's radiation; of this energy, 46% is infrared (> 0.74 μm), 9% is ultraviolet (< 0.4 μm) and the remaining 45% is visible, with wavelengths between 0.4 and 0.74 μm (Liou, 2002). A significant portion of the solar energy is absorbed by the Earth (~ 70%), where it drives

terrestrial phenomena before being radiated back into space through the atmospheric window as infrared radiation peaking at about 10 μm.

The power going into the Earth's climate system is;

$$P_{in} = C\pi R_e^2(1 - A)$$

(1.1)

Where C is the solar constant (adjusted for the sun-Earth distance), R_e is the Earth's radius and A is the short-wavelength Bond albedo (the amount of sunlight reflected back to space by the atmosphere and surface of the Earth). Subsequently, this incoming power is re-radiated back into space at long-wavelengths;

$$P_{out} = 4\pi R_e^2 \sigma T_e^4$$

(1.2)

Where σ is the Stefan-Boltzmann constant and T^4_e ($\sim$ 255 K) is the effective temperature of the Earth. This is a physical averaged long-wave emission temperature at about 5.5 km height in the atmosphere (depending on wavelength and cloud cover, altitudes from 0 to 30 km contribute to this emission).

One can relate the effective temperature of the Earth to a more global climate parameter like the globally averaged surface temperature T_s. With this parameter, one must introduce a greenhouse forcing parameter G [W/m^2] defined as the difference between the emission at the top of the atmosphere and the surface. The forcing G increases with increasing concentration of greenhouse gases. After Raval and

Ramanathan (1989), one can define the normalized greenhouse effect g, with $g = G/\sigma\, T^4_s$.

Then the outgoing power can be written as;

$$P_{out} = 4\pi R_e^2 \sigma (1 - g) T_s^4 \qquad (1.3)$$

If the planet is in radiative equilibrium, $P_{in} = P_{out}$, then one has;

$$T_s^4 = \frac{C}{4\sigma(1-g)}(1-A) \qquad (1.4)$$

This means that the Bond albedo, together with solar irradiance and the greenhouse effect, directly controls the Earth's temperature. Global warming would result if either A decreased or g increased. The possibility of increasing greenhouse forcing due to an anthropogenic increase of atmospheric CO_2 over the past century, has been treated in detail in scientific literature over the past few decades (IPCC,1995; Houghton, 2002 and references therein). The scope of this work, however, is the Earth's short-wavelength albedo (0.15 to 4 micron), which could also play a role. A solar irradiance increase or albedo decrease has also the potential to produce a global warming. By measuring the sunlight reflected and radiation emitted by the Earth, one can determine A and g, respectively.

It has been known for some time that the so-called solar constant varies. In particular, data from the Active Cavity Radiometer (ACRIM I) on board the Solar Maximum Mission have shown for one cycle (~11 years) that the solar irradiance is about 0.1% greater at activity maximum than at activity minimum (Wilson and Hudson 1988,

1991), and now this result from a series of satellites covers two solar cycles (Fröhlich, 2000). The precise origin of the changing irradiance is generally attributed to a competition between two components of the sun's magnetic field—dark sunspots and bright faculae, but an unambiguous description remains elusive. Based on climatological models of heat storage and thermal inertia of the oceans (Jayne and Marotzke, 2001) it is widely accepted in the climate community that a 0.1% (0.3 Wm^{-2}) change is several times too small to be climatologically significant over the 11-year solar cycle (Lean, 1997), particularly if it is to be further obscured by a steady increase in greenhouse forcing. It has been suggested that there may have been two to three times larger, sustained excursions in the recent past (Lean, 1997), like during the "Maunder Minimum" (1650-1710) when a sunspot was rare (Eddy, 1976). Still, there is evidence of a solar cycle influence on climate going back more than 100,000 years (Ram and Stoltz, 1999). If the 0.1% increase in the mean solar irradiance between the mid-1980s and 1990 were typical, then one is led to consider more carefully the possibility of a variation in the Earth's albedo. After all, the Earth's reflectance seems to show considerable variation (Goode et al. 2001).

It is not unreasonable to expect that global changes in the Earth's climate would be manifest in changes in the Earth's albedo. Potential parameters affecting the albedo are volcanic eruptions, surface vegetation and/or desertification (Betts, 2000), snow and ice coverage (Randall et al. 1994), and atmospheric constituents such as aerosols, water vapor and clouds (Cess et al. 1996; Ramanathan et al. 1989; Charlson et al. 1992). Albedo changes will be determined by the total effect of the changes in all these parameters. However, these changing parameters will bring along multiple climate

feedbacks, which make assessing the exact change in albedo a hard task (Cess et al. 1996). During the past decades there have been some efforts to measure the Earth's albedo from space.

The Earth Radiation Budget Experiment (ERBE) instruments were flown on the ERBS, NOAA-9 and NOAA-10 satellites from late 1984 to 1990. ScaRab/Meteor and ScaRaB/Ressur also measured the albedo during 1994-95 and 1998-99 respectively. More recently, in 1998, the Clouds and the Earth's Radiant Energy System (CERES) has begun taking measurements, and the Geostationary Earth Radiation Budget Experiment (GERB), the first broad-band radiometer on a geostationary satellite, is in operation since December 2002. In the future, the TRIANA mission may also contribute by observing the full Earth disk reflectance from a privileged deep-space position at the L1 Lagrangian point; although at present the mission is on hold. However, a long-term data series of the Earth's albedo is difficult to obtain due to the complicated inter-calibration of the different satellite data and the long gaps in the series.

To derive ideally perfect estimates of the Earth's reflectance it would be necessary to observe reflected radiances from the Earth, from all points on the Earth and at all angles. Therefore, all measurements from which albedo can be inferred require assumptions and/or modeling to derive a good measurement. The availability of different albedo databases and their inter-comparisons can help to constrain the assumptions necessary to derive estimates. In this sense, long-term ground-based estimates of the Earth's reflectance complementary to those from satellites would be an advantage.

Here, the focus is on a terrestrial determination of the Earth's global albedo from an old and largely forgotten method. That is, global albedo can be determined by measuring the

amount of sunlight reflected from the Earth and in turn, back to the Earth from the dark portion of the face of the Moon (the "Earthshine" or "ashen light"). The most important historical program of Earthshine measurements was carried out by Danjon (1928, 1954) from a number of sites in France. He used a "cat's-eye" photometer to produce a double image of the Moon, allowing the visual comparison of the intensities of two well-defined patches of the lunar surface - one in sunlight and the other in Earthshine - at various lunar phases. Using the "cat's-eye" mechanism, he stopped-down the light from the sunlit portion to match the brightness of the ashen portion. This differential measurement removed many of the uncertainties associated with varying atmospheric absorption and the solar constant, allowing Danjon to achieve his estimated uncertainty of roughly 5%, ignoring his appreciable systematic error from an incorrect determination of the Moon's reflectivity. The Big Bear Solar Observatory (BBSO) measurements are about an order of magnitude more precise than Danjon's estimates, in large part because current observations have better measurement technologies. The BBSO group has also solved the problem of the uncertainty in the scattering from the Moon as a function of the phase of the Moon (see Chapter 4). At about 1% precision on individual nights, BBSO terrestrial estimates of the Earth's albedo have a precision comparable to that from satellites like ERBE with around the same value (Harrison et al. 1990) and to those of the CERES instrumentation, of around 1% (Kato et al. 2002).

Note that the 1% precision applies to the Earth's reflectance for a given night, the precision stated for ERBE products apply in most cases to monthly means for 2.5° latitude-longitude regions or larger and in some cases to daily values. A quasi instantaneous regional flux or albedo value is far less accurate than the corresponding

radiance (specific intensity) measurements from which it is derived, because of the notorious uncertainty in radiance-to-flux conversion. The bi-directional reflectance distribution functions used in ERBE only have statistical validity. Those being developed with CERES data may be better, but they remain largely statistical.

From 1926 to 1930, Danjon made 207 measurements of Earthshine. Dubois (1947) continued the program through 1960 from the observatory at Bordeaux using a Danjon-type photometer. Danjon's and Dubois' results show a number of interesting features. The daily mean values of the observations vary more widely than would be expected on the basis of the variation of measurements on a single night. This can plausibly be attributed to daily changes in cloud cover or changes in the reflection because of changes in the sun-Earth-Moon alignment during a lunar month. The typical lifetime of large scale cloud systems (1000's of km) is 3 days (Ridley, 2001), but from one night to the next the Earth's area contributing to the Earthshine changes (see Figure 1.1). Unfortunately, extensive cloud-cover data were not available at the time of Danjon's and Dubois' observations.

Danjon (1928) also examined his observations to determine whether there was a long-term trend in albedo, but found none. Dubois' observation for some 20 years ending in 1960, showed considerable annual variability, which Dubois speculated was due to solar activity. Dubois' published monthly variations from 1940-1944 also show a strong correlation with the 1941-42 El Niño. In the past forty years, there have been observations of Earthshine by Huffman et al. (1989) and one-time observations by Franklin (1967) and Kennedy (1969).
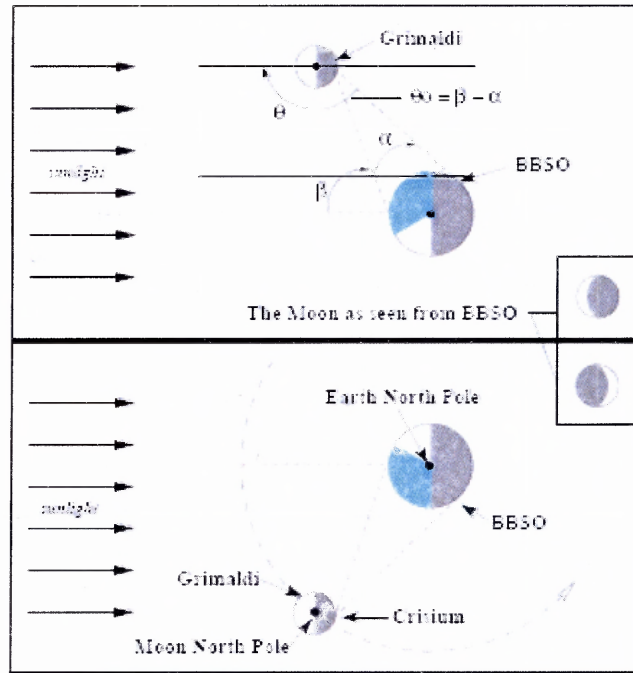
Figure 1.1 A not-to-scale cartoon of the sun-Earth-Moon system viewed from the pole of Earth's orbit. In the top panel, the Earth's topocentric phase angle, α, with respect to BBSO is defined. The plot also shows the Moon's selenographic phase angle, θ, with respect to one of the fiducial points (Grimaldi) used in the observations made from BBSO (also indicated). β is the angle between the sunlight that is incident somewhere on the Earth and reflected, as Earthshine, to Grimaldi. $\Theta o (= \beta - \alpha)$ is the angle between the Earthshine that is incident, and reflected from the Moon. The path of the Earthshine is indicated by the broken lines. Θo is of order 1o, or less. In the lower panel the same diagram is drawn for a negative lunar phase angle, and extra features like the Moon's orbit around the Earth are indicated. On both panels the aspect of the Moon as would be seen from BBSO is also indicated in a box. The light-shaded areas of the Earth indicate the approximate longitudes range that contributes to the Earthshine. Note how for positive lunar phases (top panel) the Earthshine contribution comes from longitudes east of BBSO while for negative phase (lower panel) angle it comes from longitudes west of BBSO.

Danjon used his observations to estimate the mean global albedo. Since the observations are only at visible wavelengths, they must be corrected for the balance of the short-wavelength radiation, most of which is in the near IR. Estimates of this

correction were made by Fritz (1949), after taking into account the decrease of the Earth's albedo with increasing wavelength ("blue planet"). Fritz also attempted to correct for the geographical bias in Danjon's observations. The Earth eastern hemisphere (Asia, Russia), which was most frequently observed by Danjon, has a greater fraction of land than does the globe as a whole, implying that Danjon's value would be high because the sea is dark compared to land. Combining the decreases from the absence of the IR and geographical bias, Fritz found that Danjon's visual albedo of 0.40 corresponds to a Bond albedo (considering all the wavelengths and directions) of 0.36.

Flatte et al. (1991) noted that a correction must be made for the "opposition effect" present in lunar reflectance properties. Observations of the Moon show that the Moon's reflectivity has a strong angular dependence, which was unknown in Danjon's time. This enhancement was once thought to be due to the porous nature of the lunar surface (Hapke, 1971). More modern work has shown it to be caused by both coherent backscatter of the lunar soil and shadow hiding in roughly equal amounts (Hapke et al. 1998; Hapke et al. 1993; Helfenstein et al. 1997). In fact, as shall be seen in Chapter 4, an incorrect lunar phase function is the primary source of Danjon's overly large visual albedo. The group has been steadily observing the Earthshine from Big Bear since 1998 to determine the Earth's reflectance and its variations. The photometric observations cover the spectral range from 400 to 700 *nm*. In this thesis, the method that was used to determine reflectance from Earthshine is discussed in detail. As mentioned, the first such observations were made by Danjon (1928), and considerable modernization was required to make this method sufficiently precise to usefully complement satellite measurements. Beyond developing the methodology, the purpose of the next six Chapters is to

demonstrate the reliability of the technique. This is followed by a presentation and analysis of the results of the observational work and simulations of the observations. The final Chapter covers spectral observations of the Earthshine in the visible range (500-800 nm) from the 60" (1.5 m) telescope on Mt. Palomar, taken with the Echelle spectrograph in long slit mode.

CHAPTER 2

DETERMINING THE EARTH'S REFLECTIVITY FROM EARTHSHINE

Ground-based measurements of the short-wavelength (visible light and near infrared) albedo of a planet in this solar system are relatively straightforward—except for the Earth. However, the albedo can be determined from the ground by measuring the Earthshine. From a terrestrial perspective, the Earthshine is the sunlight reflected from the day side of the Earth to the night side of the Moon, and finally back to an observer on the Earth. At any moment, the Earthshine can provide an instantaneous, differential cross-section of the sunlight reflected from the Earth, see Figure 1.1.

The Earth's differential cross-section is defined as the ratio between the scattered radiation per unit solid angle and the incident radiation of a given surface, and depends on its geometrical albedo and its phase function. The geometrical albedo (the ratio between the intensity of normally incident radiation reflected from a surface and the incident intensity) is independent on β, the Earth's phase angle; rather, it is proportional to the backscattered cross-section. At the top of the atmosphere (taken by convention as being 30 km high by the ERBE data processing), the differential cross-section of the reflected sunlight for scattering by an angle β (note that β is the supplement of the usual scattering angle) is given by;

$$\frac{d\sigma}{d\Omega} \equiv p_e f_e(\beta) R_e^2$$

(2.1)

11

Where R_e is the radius of the Earth, p_e is the geometrical albedo of the Earth and β is the Earth's phase function, defined such that $f_e(0) = 1$, as is done for the case of the Lambertian phase function given in Equation (2.4).

One can note from Equation (2.1) that the Earth's sunlight reflectance is bi-directional. This is a recognized central difficulty of satellite-based albedo estimates, where the solar zenith angle (function of latitude, date and time), the viewing zenith angle, and the relative sun-Earth scene satellite azimuth must be taken into account with different instruments and satellites providing different samples in the viewing and illumination angles, and with more or less reliable angular models (Loeb et al. 2003; Wielicki and Green, 1989). The sampling is necessarily different, with Earthlight on the Moon, but the problem does not go away because the measurements are restricted to the light scattered to the orbital plane of the Moon around the Earth. For the Earthshine, no attempt is made to correct for the anisotropy of the sunlight reflected by the Earth.

From an Earthshine perspective, using Equation (2.1), the total scattering cross section is

$$\sigma = \int \frac{d\sigma}{d\Omega} d\Omega = \pi R_e^2 p_e \int_{-\pi}^{\pi} f_e(\beta) \mid \sin(\beta) \mid d\beta$$

(2.2)

where p_e and f_e depend on the Earth's weather, season, and climate. Additionally, f_e depends on the Earth's phase as seen from the Moon. From the total cross-section, one can define the Bond albedo—the fraction of solar energy incident on the planet that is reflected as;

$$A = \frac{\sigma}{\pi R_e^2} = p_e \int_{-\pi}^{\pi} f_e(\beta) \mid \sin(\beta) \mid d\beta$$

(2.3)

Using Earthshine data, one can integrate over the phases of the Moon to determine, say, a seasonally or yearly averaged Bond albedo. β varies between 0 and $\pm\pi$, with 0 to π being the waning Moon and $-\pi$ to 0 being the waxing Moon. This averaging is done over a series of measurements, which comprise a wide range of geographical and temporal coverage. When doing Earthshine observations the Earth as seen from the Moon changes day to day due to the Moon's declination, the Earth's phase, and meteorological reasons. By averaging observations over lunar phases, and thus time, stable estimates of the Bond albedo are obtained for seasonal and yearly time scales.

If it is assumed that the Earth is a Lambert sphere, one can do the integrals in Equations (2.2) and (2.3) exactly. A Lambert sphere isotropically reflects from its surface, which is assumed to be fully diffusive. Then, f_L, the Earth's Lambert phase function, is determined by;

$$f_L(\beta) = \frac{(\pi - \mid \beta \mid) \cos \beta + \sin \mid \beta \mid}{\pi}$$

(2.4)

The Earth's phase function is observed to be very roughly Lambertian for $\mid \beta \mid \leq \frac{2}{3}\pi$ (Goode et al., 2001). Under this assumption, one can determine a simple proportionality between the geometric albedo and the global or Bond albedo, namely;

$$p_{e,L} = \frac{2}{3} A_{B,L}$$

(2.5)

Modeling confirms that the Earth's phase function is approximately Lambertian for $|\beta| \leq \frac{2}{3}\pi$ (Flatte et al. 1991). Thus, a conveniently normalized, differential measure of the Earth's reflectivity is the apparent albedo, p^*, where;

$$p^* \equiv \frac{p_e f_e}{p_{e,L} f_{e,L}} A_{B,L} = \frac{3}{2} \frac{p_e f_e}{f_{e,L}}$$

(2.6)

which is the albedo of a Lambert sphere that would give the same instantaneous reflectivity as the true Earth at the same phase angle, and where an unchanged p^* as a function of phase angle would imply a Lambertian Earth.

One may think of p^* as a sort of generalization to nonzero phase angle of what Allen (1973) calls simply p, with p being "the ratio of a planet brightness at phase angle 0 to brightness of a perfectly diffusing disk with the same position and apparent size as the planet". The Bond albedo is then defined as $A = pq$, where q "is a factor that represents the reflection law."

An observer on the Moon in the region illuminated by the sun and visible from the Earth would see both the direct sunlight and some part of the sunlit Earth. The solar flux (or irradiance) seen by that observer would be;

$$I_s = \frac{C}{R_{ms}^2}$$

(2.7)

where C is the solar constant and R^2_{ms} is the Moon-sun distance measured in astronomical units. Similarly, the irradiance of the Earthlight would be;

$$I_e = \frac{C}{R^2_{es}} p_e f_e(\beta) \frac{R^2_e}{R^2_{em}}$$

(2.8)

where R_{em} and R_{es} are the Earth-Moon and Earth-sun distances, respectively. Thus, the Earth's reflectivity can be expressed as;

$$p_e f_e(\beta) = \frac{I_e}{I_s} [\frac{R_{em}}{R_e}]^2 [\frac{R_{es}}{R_{ms}}]^2$$

(2.9)

In the observations, pairs of diametrically opposite fiducial patches are observed, five in the Earthshine and the other five in the sunlit part of the Moon, both near the night-time lunar limb. Hereafter when referring to radiances, the term 'Earthshine' will refer to the radiances measured for the five fiducial patches on the Earthshine side of the Moon, and the term 'Moonshine' will refer to the radiances measured for the fiducial patches located on the bright side of the Moon bathed in sunlight. The term 'crescent' radiance will also be used in following Sections, indicating the measured radiance averaged over the whole sunlit area of the Moon.

Representative pairs of opposing fiducial patches "a" and "b" will be treated as unit projected areas. If a is illuminated only by the Earthshine, the radiance observed by an observer on the Earth at a distance R_{oa} would be;

$$I_a = I_\epsilon \frac{p_a f_a(\theta_0)}{R_{oa}^2} T_a$$

$$(2.10)$$

where T_a is the transmission of the Earthshine through the atmosphere, and $f_a(\theta_0)$ is the *lunar* phase function for the near retroflection from patch a. Therefore the θ_0 value is almost always $\leq 1°$, see Figure 1.1. Thus, I_a/T_a is the observed radiance corrected for airmass. Similar to Equation (14), the radiance of the sunlit portion, b, would be;

$$I_b = I_s \frac{p_b f_b(\theta)}{R_{ob}^2} T_b$$

$$(2.11)$$

where θ is the lunar phase angle and θ, like α and β, varies between $0°$ and $\pm 180°$ (where positive angles correspond to a waning Moon and negative to a waxing Moon), and where the lunar phase function, $f_b(\theta)$ embodies the dependence of the fiducial patch on the angle between the sunshine and the Moonshine, see Figure 1.1. The available nights of Earthshine observations are those with lunar phase angle between $\pm 40°$ to $\pm 150°$. Thus;

$$\frac{I_a/T_a}{I_b/T_b} = \frac{I_\epsilon}{I_s} \frac{p_a f_a(\theta_0)}{p_b f_b(\theta)} \frac{R_{ob}^2}{R_{oa}^2}$$

$$(2.12)$$

and

$$p_e f_e(\beta) = \frac{I_a/T_a}{I_b/T_b} \frac{p_b f_b(\theta)}{p_a f_a(\theta_0)} [\frac{R_{es}}{R_e}]^2 [\frac{R_{oa}}{R_{ob}}]^2 [\frac{R_{em}}{R_{ms}}]^2 \qquad (2.13)$$

Although there is a small difference between the Earthshine and Moonshine spectra (mainly due to Rayleigh scattering in the Earth's atmosphere, which translates in a 5 *nm* shift of the peak of the Earthshine spectrum toward the blue), Equation (2.13) is independent of lunar reflectance provided all quantities labeled by "a" are derived from the Earthshine, and all labeled "b" come from Moonshine. However, one ultimately takes p_a and $f_a(\theta_o)$ from Moonshine data, which introduces a dependence on the lunar reflectance. This effect is small compared to the spread among the p_b/p_a, and is treated as being subsumed into that ratio, see Chapter 4 Section 4. Also, $(R_{oa}/R_{ob})^2$ is so close to unity that it can safely set in Equation (2.13) to unity. Thus, it is shown that;

$$p_e f_e(\beta) = \frac{I_a/T_a}{I_b/T_b} \frac{p_b f_b(\theta)}{p_a f_a(\theta_0)} [\frac{R_{em}}{R_e}]^2 [\frac{R_{es}}{R_{ms}}]^2 \qquad (2.14)$$

The Earthshine group measures I_a and I_b in the nightly observations, and correct for airmass (e.g., I_a/T_a). The lunar phase function has been measured quite accurately over the last three years. The group uses the total lunar eclipse data from November 29, 1993 to measure the ratio of the geometrical cross-sections of the two fiducial patches, p_b/p_a. For the five fiducial regions, this ratio ranges between 0.9 and 1.1. In Chapter 5, Equations (2.6) and (2.14) are combined to define the measure of the Earth's reflectivity, p^*, in terms of measured quantities. The variations of the Earth-Moon distance are accounted for.

CHAPTER 3

DATA REDUCTION

3.1 Image Analysis

The Earthshine and Moonshine (sunlit part of the Moon) intensities are measured by integrating the brightness of a pair of fiducial patches—one from the bright side and the other from the dark side of the lunar disk. In this study, ten physically fixed fiducial patches were used with five in the Earthshine and five in the Moonshine, see Figure 3.1. In selenographic (lunar) coordinates, the center latitudes and longitudes of the five patches on the Crisium side are (-17.5, -70.), (-11.2, -71.5), (-5., -76.), (0., -75.), and (7.5, -76.5), and those of the five patches on the Grimaldi side are (28.5, 72.5), (12.5, 75), (0., 77.), (-7.5, 75.), and (-13., 75.). Each patch covers a longitudinal range of about 10 degrees and latitudinal range of 3 to 5 degrees, the surface area being about 0.1% of the lunar surface, which corresponds to about 100 camera pixels. These patches are located in the "highlands" of the lunar surface, and the physical reflectivity of each is roughly comparable.

One of the patches on the Grimaldi side is very close to Danjon's choice, while the patches on the Crisium side are all closer to the limb than Danjon's patch (Figure 3.1).
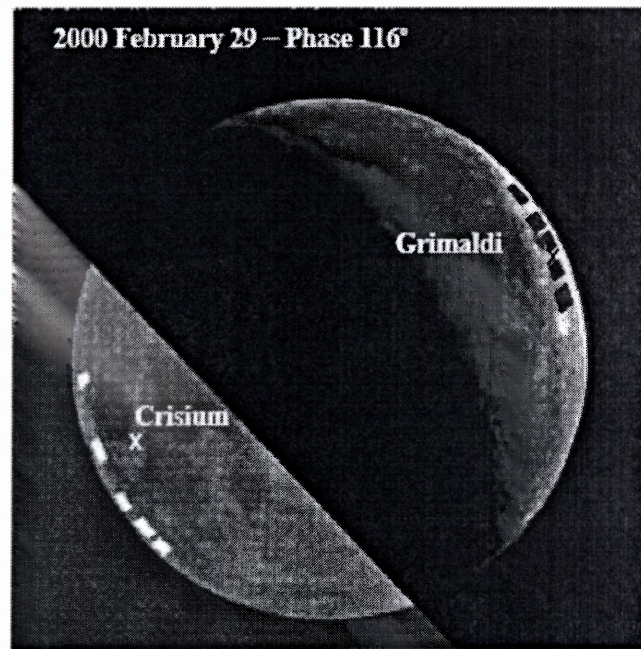
Figure 3.1 The Moon showing the bright side and the Earthshine. The Grimaldi side is in the Moonshine and the Crisium side is in the Earthshine. The ten fiducial patches used in the observations made from BBSO are indicated. The crosses give the approximate positions of Danjon's fiducial patches. Goode et al. (2001) used one fiducial patch on each side, and on the Crisium side it is the one closest to the white cross, while on the Grimaldi side, it is the one immediately above the black cross. In the image, the lunar phase is 116o, near a declining quarter Moon. Unlike the Moonshine, the Earthshine is flat across the disk. The flatness is due to the uniform, incoherent back-scattering (non-Lambertian) in contrast to the forward scattering of sunlight occurring in the sunlit lunar crescent surface.

To locate the patches in each lunar disk image taken every night, the transformation was established between the CCD image coordinate system and the selenographic coordinate system. Once the transformation between the image plane and the selenographic system was made, the five pairs of fiducial patches were precisely located on the lunar disk image.

The apparent areas of these patches change from night to night because of lunar libration. The intensity is read out as an average of the whole area, and the difference

due to the geometric effect of the reflectivity arising from libration is accounted for in the next step of data reduction (see Chapter 3.2). All the data reduction is done automatically by a software package specially developed for this purpose. The process of Earthshine data reduction and calibration is illustrated in Figure 3.2.
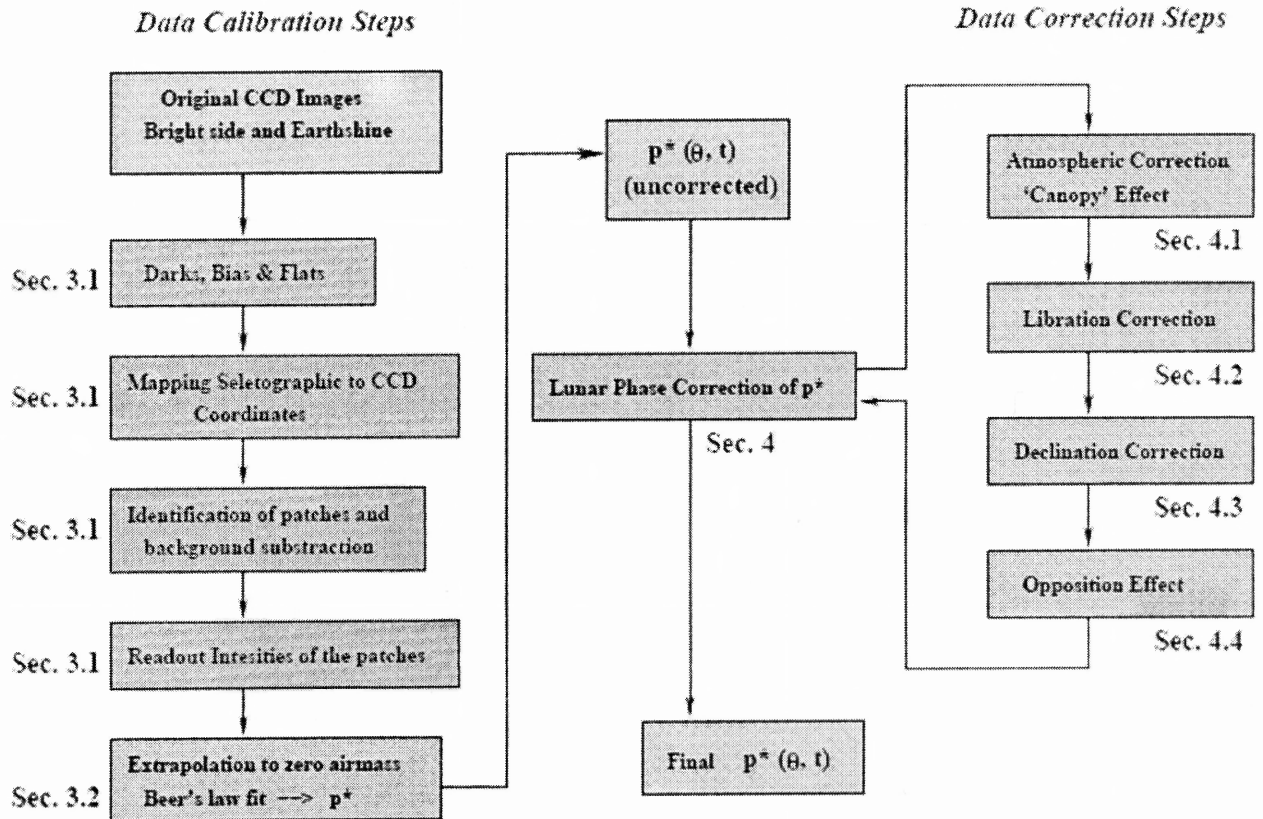
Figure 3.2 A schematic diagram of the Earthshine data reduction procedure. On the left are the standard astronomical steps followed to correctly retrieve the intensity of the lunar dark and bright side patches. On the right are the steps necessary to correct the retrieved values for the lunar phase function. The thin white boxes correspond to image treatment procedures, while the grey boxes correspond to calculations done with readout intensity values or p^* data. The end result is a calibrated series of p^* depending on lunar phase, θ, and on time along one night. Also obtained is an averaged $p^*(\theta)$ for the night by taking the mean of $p^*(\theta, t)$. Indicated in the chart are the sections (Chapters in this thesis) in which each data reduction step is explained in detail.

To ensure accurate photometry, flat-fielding and dark current subtraction, are performed on each image. For Earthshine images, one needs to subtract the background scattering from the bright side of the Moon due to the Earth's atmosphere and the telescope. The background scattering should be a function of both the inclination of the vector connecting the lunar center and the background point with respect to the lunar equator, and the distance from the background point to the crescent. After experimentation, it was found that one could safely assume that on the Earthshine side, where the background points are not too close to the crescent, at a fixed inclination with respect to the lunar equator, the background intensity falls off linearly with the distance of the background point to the lunar center. Such a linear relation holds for the points that are not too far from the lunar equator. So, for each fiducial patch centered on the vector connecting the lunar center and the patch, a small cone is defined with an angular size of 5°, and fit the intensities of the background points which are beyond the lunar limb and inside the cone, as a function of their distance to the lunar center. In this way, one can extrapolate the scattering intensity to the position of the fiducial patch (inside the lunar disk) using the parameters obtained from the least-square fit, and then subtracting the linearly extrapolated value from the intensity of the fiducial patch. This procedure is illustrated in Figure 3.3.
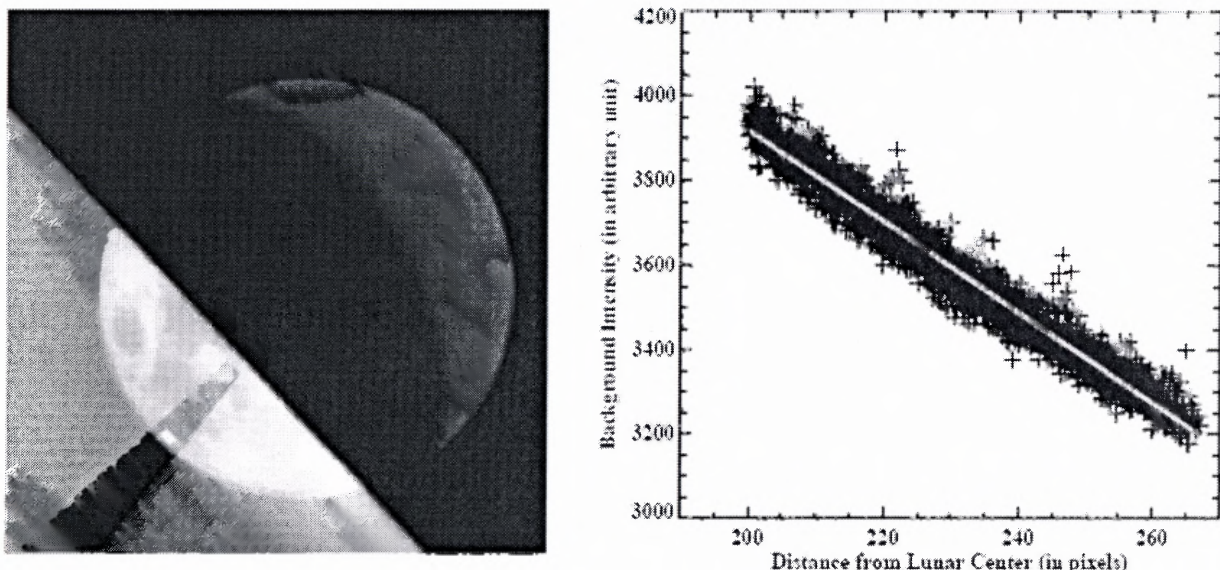
Figure 3.3 Illustration of the background subtraction for Earthshine images. The image on the left shows a background cone around a fiducial patch, within which the intensity of the background points outside the lunar disk are read out to make a fit as a linear function of the distance from the lunar center. For the image shown, the intensity inside the cone has the background subtracted already by extrapolating the linear fit to points inside the lunar disk. The plot on the right shows the decline of the off-limb intensity as the background point gets further from the lunar center, and the overplotted thick gray line indicates the least-square linear fit.

In accordance with Equation (2.14), the intensity obtained from above is also corrected by scaling to a set of standard distances between the sun, Moon and Earth, before the successive calibration steps described in subsequent Chapters are executed. Precise distance parameters are obtained from an ephemeris.

3.2 Atmospheric Extinction

To eliminate the effect of the atmospheric extinction, observations are carried out for as long as possible during the night, so that a measurement of the intensity at varying airmass can be obtained. For the bright side of the Moon, one expects the variation of the intensity to follow Beer's law:

$$I = I_0 e^{(-\alpha\eta)}$$

(3.1)

where I is the observed intensity, α is the atmospheric extinction coefficient, η is the local airmass and I_0 is the intensity at zero airmass—the intensity if the Earth had no atmosphere.

The airmass, η, is determined from the angular altitude of the Moon in the sky at different times in such a way that when φ_c (the zenith angle of the ground observer's view of the Moon, which is the complement of the Moon's angular altitude) is smaller than $60°$, $\eta = 1/\cos(\varphi_c)$; otherwise η is interpolated from a standard airmass table.

The standard airmass table lists the airmass at sea level with the pressure $p_o = 760$ mmHg and temperature $t_0 = 10°C$, and the real airmass at the observer's location must be corrected by a multiplicative factor of $p/p_0/(0.962+0.0038t)$ (Allen, 1973). BBSO is 2067m above sea level, and the pressure scale height at this altitude is 8200m, which yields $p = p_o \, exp \, (-2067/8200)$. Incorporating the calculated η into the Beer's law fitting determines α and I_o.

During the night, the evolving lunar phase function can also contribute to the changing intensity. The maximum phase change in a long night is less than two degrees, within which the intensity change is negligible compared to the change due to the airmass. Nevertheless, the group employs a quasi-iterative way to correct this minor effect, in that an initial fit of the phase function is used to correct the data, and after the airmass correction, the phase function is fit again. See the following Chapter on how to obtain the phase function. After a few iterations, the data converge to a stable result. The

observed intensity at each moment, I_i, is corrected, using the airmass, to the intensity at zero airmass, $I_i^o = I_i exp(\alpha\eta)$. The I_o variable from the fitting is further used as the intensity for that night's lunar phase function.

The goodness of the fit to Beer's law offers a ready criterion by which each night's local sky can be judged—the "good" night's data can be separated from that of the "bad" (noisy) night's (see Figure 3.4). In practice, unless it is cloudy, the data from almost all observable nights are preserved, and the standard error in the fitting for each night is further used as the input error for the lunar phase function fit. Figure 3.4 shows an example of a typical good night and bad night, as judged by fitting to Beer's law. Experience from the observations shows that the data usually follow Beer's law quite well, and the accuracy of the Moonshine fitting is often better than 1%. Among all the datasets collected for 340 nights from November 28, 1998 to March 31, 2002, the accuracy of the fitting is better than 1% for 110 nights, and the accuracy is between 1% and 2% for 139 nights, and between 2% and 3% for 52 nights.
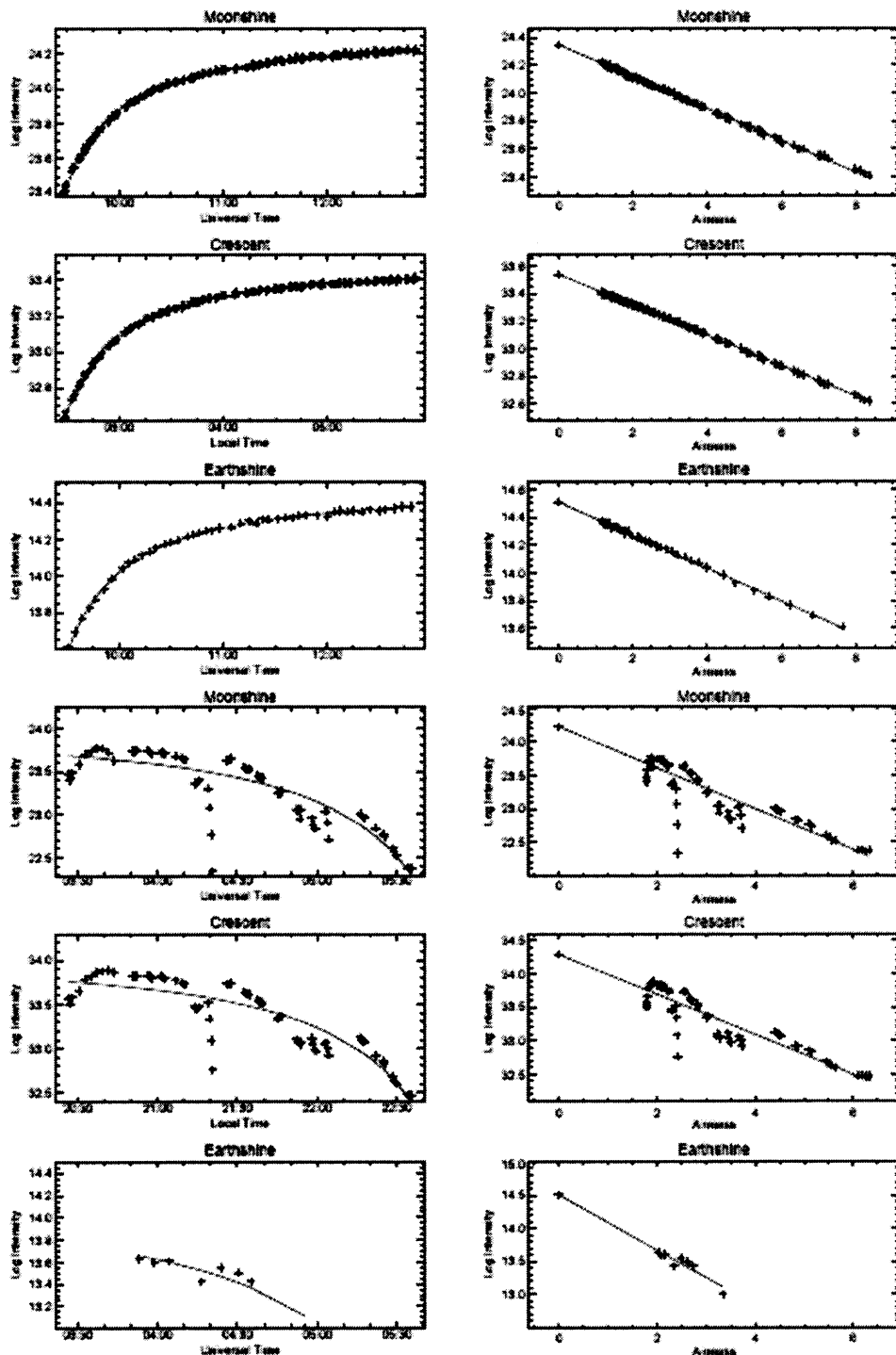
Figure 3.4 In each of the four groups of three graphs is shown the intensity per unit area of the Moonshine (top), the crescent (middle), or the Earthshine (bottom), is plotted against time (left) and airmass (right). Intensities are values read from the CCD, corrected for all the steps indicated in Chapter 3.1, and divided by the lunar phase function. For Moonshine and crescent intensities, the value has been also divided by the transmission of the bright side filter. The "+"'s indicate observed data points, and the solid lines are the fits to Beer's law. The top six panels are a good night, the bottom six a bad night.

In the case of Earthshine intensity, apart from the atmospheric transmission, the evolution of the Earthshine is also influenced by changing of the Earth during a given night; e.g., the sun rising over a cloudy China. In addition, almost every month, on a few nights, it is observed that the evolution pattern of the Earthshine intensity does not track Beer's law in an unambiguous way, even though the Moonshine intensity closely follows Beer's law. An example of such a case is shown in Figure 3.5. In general, the fit to the Earthshine yields a standard deviation that is larger than that for the Moonshine fitting by one-half to one percent. This latter difference contains the signal of the Earth's albedo variations. On such nights when the evolution of the Earthshine is significantly controlled by real changes in the Earth's reflectance, apart from the atmospheric extinction, as illustrated in Figure 3.5c, the atmospheric extinction coefficient α obtained from the Beer's law fitting of the Earthshine observations may deviate from the true value. That is, some part of the Earthshine signal may be subsumed into the atmospheric extinction, and vice versa, so that the correct atmospheric attenuation cannot be properly determined from the standard Beer's law fitting.
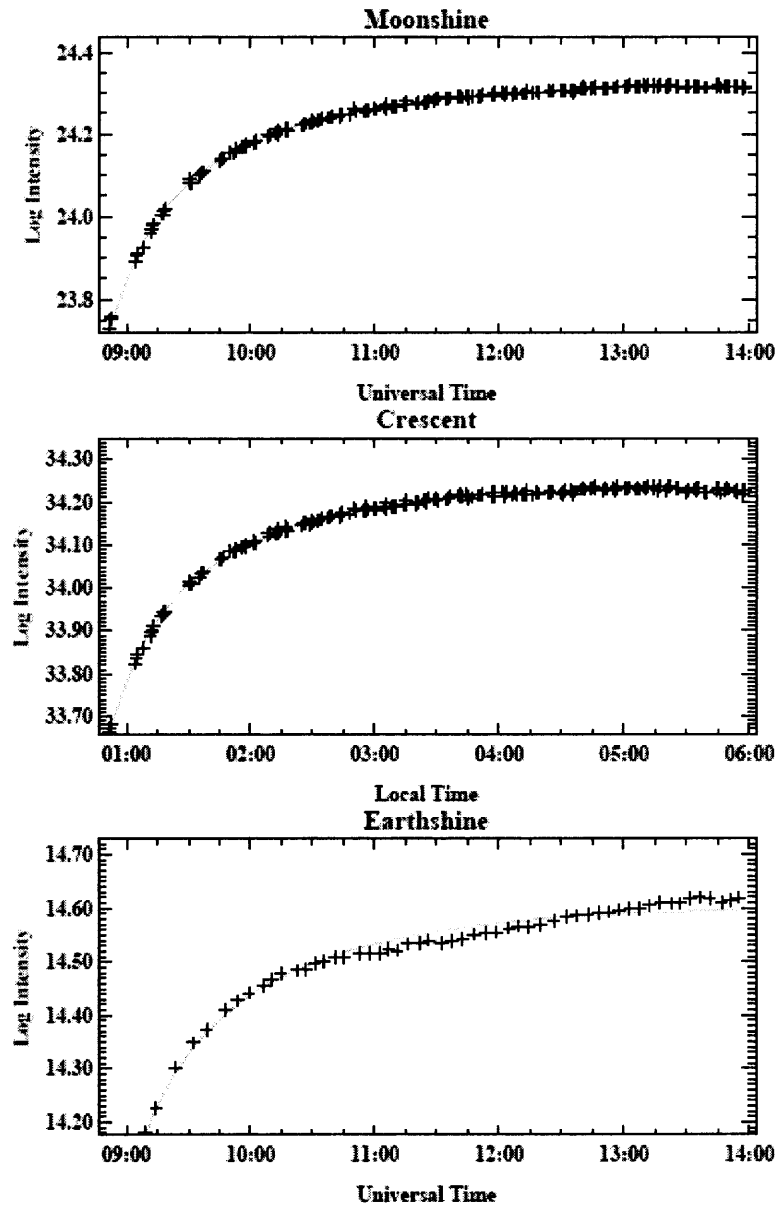
Figure 3.5 The Moonshine, crescent and Earthshine intensities and their Beer's law fit for the night of Jan. 28, 2000 showing that while the Moonshine and crescent intensities follow Beer's law very well, the Earthshine intensity evolution deviates from Beer's law. The standard deviations of the fits are 0.004, 0.005, 0.014, respectively. The fact that the fit is poor only for the Earthshine implies sizable short-term variations in the Earth's apparent albedo as seen from BBSO due to a combination of factors including, among others, the Earth's rotation, anisotropic reflectance and weather changes.

To deal with this problem, the group investigated the relationship between the atmospheric extinction coefficients for radiances measured at the five patches on the Earthshine side of the Moon (α_e^i; i = 1, 2, 3, 4, 5), the radiance of the five patches on the bright side or Moonshine (α_m^i) and the radiance of the total area of the crescent (α_c). Figure 3.6 (a) and (b) show the relationship between α_c and the α_m^i for all five fiducial patches. Least-square fits reveal that the α_m^i (i = 1, 2, 3, 4, 5) can be regarded as being identical to one another, and to α_c. This is not a surprise, even though the atmospheric attenuation is also a function of the wavelength, as the light from a Moonshine fiducial patch is assumed to have the same spectrum as the light from the whole bright side. Similarly, the Earthshine extinction coefficient, α_e, is linearly correlated with α_c (Figure 3.6 (d)), but the absolute value of α_e is systematically larger than that of α_c, indicating a stronger atmospheric attenuation in Earthshine than in Moonshine. This is because the Earthshine and the Moonshine have different spectra, specifically; the Earthshine is bluer than the Moonshine (Tikhoff, 1914; Arnold et al. 2002; Woolf et al. 2002), because the bluer the light the more effectively the Earth's atmosphere scatters it away by Rayleigh scattering.
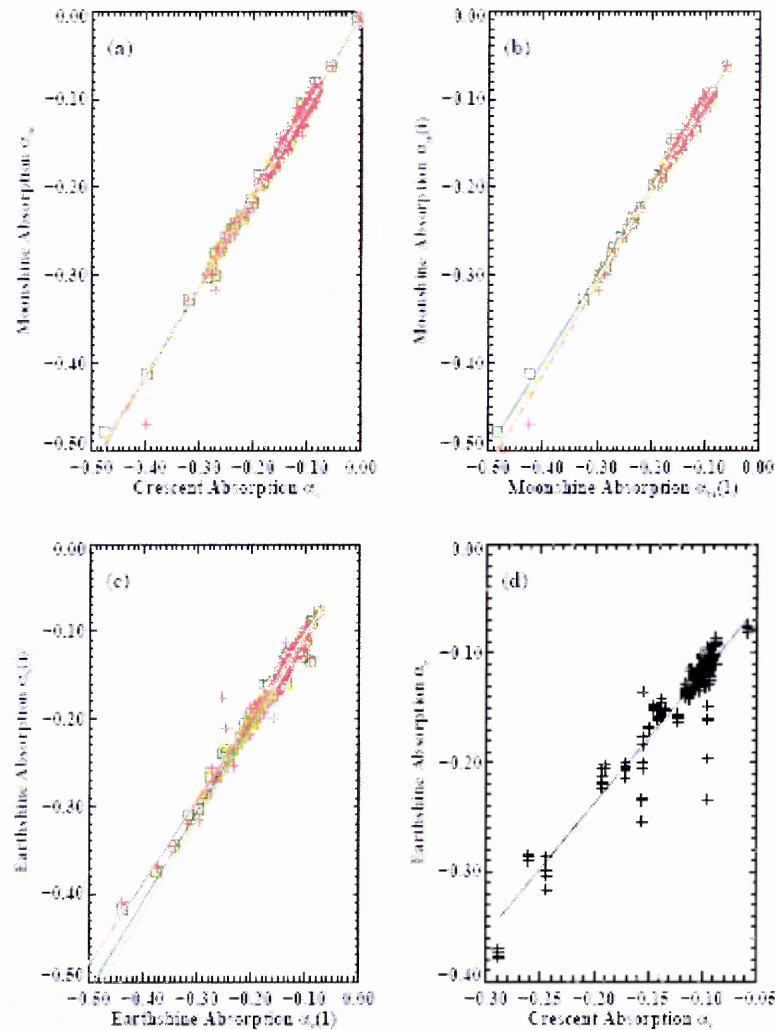
Figure 3.6 The variation of the atmospheric extinction coefficients for the crescent, (α_c) Moonshine (α_m) and Earthshine (α_e). Panel (a) illustrates α_m (for five fiducial patches as indicated by different symbols) against α_c from which it is clear that the crescent and Moonshine patches are very much alike; (b) shows α_m of four out of five fiducial patches (as indicated by different symbols) vs. the fifth fiducial patch, illustrating that α_m is virtually the same for different patches (note the equivalence of each linear, least squares fits to the data for each patch); (c) shows α_e for four out of five fiducial patches (as indicated by different symbols) vs. the other fiducial patch, showing that α_e is also the same for different fiducial patches in the Earthshine; and (d) shows α_e (of all fiducial patches in Earthshine) against α_c, which is consistent with the Earthshine being bluer than the Moonshine. The various straight lines in each panel indicate a least squares fit to the appropriate data.

The solution to fitting nights like those shown in Figure 3.5 lies in exploiting the linear scaling law that one finds between α_e and α_c. This scaling enables one to make a better determination of α_e from α_c for the nights when the usual, local airmass changes leading to a good Beer's law fit for the Moonshine, are compounded by sharp Earthshine variations. In those cases, the mixture yields observational Earthshine data that deviate sufficiently from Beer's law, so that one cannot be confident of the fit obtained in the usual way. The solution lies in using α_c to fix α_e for the problematic nights, beginning with;

$$\alpha_e = a \times \alpha_c + b \tag{3.2}$$

where the scaling parameters a and b are obtained by a linear least-square fit of the above relation using α_e and α_c from the nights that do not show apparent Earthshine evolution that strays strongly from the Beer's law fit. For the nights of significant Earthshine change, the standard deviation of the Beer's law fitting of the Earthshine (σ_e) must be a lot larger than that of the crescent (σ_c), given that the local atmosphere is reasonably stable throughout a single night. For this reason, a further assumption is made that when σ_e is less than a cutoff value q times σ_c, i.e., $\sigma_e < q\sigma_c$, the global change is not significant during this night, and α_e from the Beer's fitting for this night is reliable. Only then are these nights used to make the fit to determine a and b.

CHAPTER 4

THE LUNAR PHASE FUNCTION

4.1 Introduction

The lunar phase function is defined as the normalized change in the Moonshine intensity

as a function of lunar phase, which represents the geometric reflectance of the Moon. It is

measured from the readout intensity of each of the fixed fiducial patches (five on the

Crisium side and five on the Grimaldi side) used throughout the observations, after

carrying out all the corrections described in the previous Chapter to the raw data. When

the observed intensity readout is plotted against the lunar phase for all nights, the data are

quite scattered around different means for each branch, as illustrated in Figure 4.1, for the

Crisium and Grimaldi pair used in Goode et al. (2001). This figure, and that pair, is

treated in detail in this Section. The raw results for all pairs take the same form as the

chosen pair that is used for Figure 4.1. On the face of it, the large scattering of data in

Figure 4.1 would seem to preclude a precise determination of the Earth's albedo from

measuring the Earthshine. However, most of the scattering of data is due to known

physical effects which can be systematically accounted for and removed.

The first factor is the night-to-night change of the local atmosphere, apart from

the nightly atmosphere attenuation which follows Beer's law. Such a change affects the

measured crescent as a whole, and Moonshine and Earthshine from the fiducial patches in

precisely the same way, and hence, the raw phase function can be corrected by treating

the crescent as a standard star (see Section 4.2). This correction does not alter the

determination of p^*, because the correction applies to both the Earthshine and Moonshine, while p^* is given by the ratio of the Earthshine to the Moonshine.

The second factor is the sun's position, namely the declination and right ascension, due to the changing angle of the sunlight into the Earth-Moon system at the same lunar phase, but in different synodic months. This changes the range of well-illuminated latitudes both on Earth and the Moon from one month to the other. To first order, one fits out the alteration of the scattering introduced into the phase function (see Section 4.3). As it turns out, this is a very small correction to the Moonshine intensities and consequently to p^*.

The third known source of the scatter in Figure 4.1 is the Moon's libration, which changes the observed intensity from the Moonshine fiducial patches, but does not affect the Earthshine intensity (see Figure 3.2 in which the non-uniformity of the Moonshine near the limb is apparent, but there is no such non-uniformity in the Earthshine). To first order, one models this effect as a linear function of the libration and correct it for both the phase function and in the Moonshine intensity I_b, when using I_b to calculate p^* (Section 4.4).

The results of these corrections are developed in this Chapter, one step at a time. It shall be seen that one can determine the lunar phase function to 0.5%, which gives real confidence that observing the Earthshine can yield a precise reflectance for the Earth.

In the last part of this Chapter (4.5), the overall lunar phase function is normalized to connect the right and left branches of the lunar phase function by treating the opposition surge that occurs at small phase angles (Hapke, 1971; Flatte et al. 1991; Helfenstein et al. 1997). The data here are from the fullest of full Moons and the one total

lunar eclipse observed from Big Bear. The total eclipse enabled the group to determine the ratio of the geometrical albedos of the opposing pairs of fiducial patches.
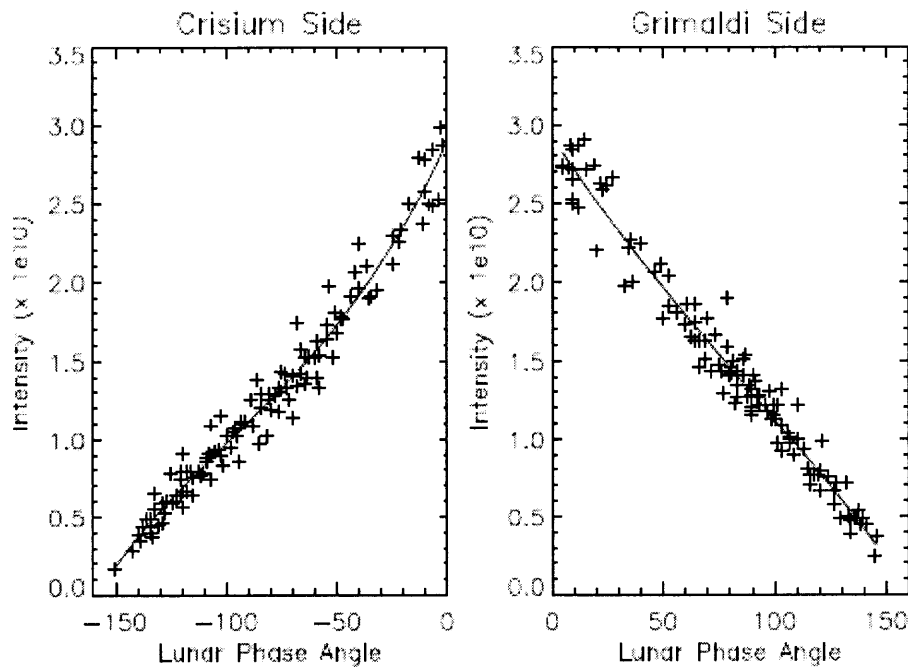
Figure 4.1 The intensity of the Moonshine for the Crisium side and Grimaldi side fiducial patches of Goode et al. (2001) with a third order polynomial (including higher order terms has no noticeable effect) fit for each. Clearly, there is a roughly linear decrease in the intensity of the reflected light going from full Moon to new Moon.

4.2 Atmospheric Correction

The nightly fits of the Moonshine intensity to Beer's law are quite good, and so the extrapolation to zero airmass would seem quite reliable. However, there is an appreciable change in the lunar phase function (see Figure 4.1), for the same phase, month-to-month. As shall be seen, the prime cause of this variation is that, even after

extrapolation to zero airmass, the resultant intensity is subject to changes in the local atmospheric conditions. It seems that the local atmosphere is not a uniform plane parallel gas, but rather something more like a canopy superposed on a plane parallel atmosphere. The canopy mutes the intensity by the same amount for all airmasses, and therefore its effect remains after extrapolation. Because of this, there is a deviation in the intensity measured from the same fiducial patch at the same lunar phase, but on different nights (that is, successive lunar cycles). To solve this problem, the common practice of nighttime photometry observations of standard stars was used to account for the muting. It was found that the crescent of the Moon (the total area illuminated by sunlight) was the best standard "star".

In the extrapolation to zero airmass, a fifth degree weighted polynomial fit was used for both the fiducial patch intensity and the average crescent intensity over the area of the bright portion as the way to determine the average of the intensity at each lunar phase. In removing the canopy effect, double weight is given to nights for which the lunar phase is less than ±5°. This is done because of the pronounced opposition effect that gives a sharp increase in the Moonshine intensity when lunar phase approaches zero degrees (see Section 4.5). The deviation of the measured intensity at each data point from the fitting curve for the lunar phase function, in both the Moonshine case and the crescent case are obtained, and the cross correlation between these deviations is calculated. For the morning observations, in which the lunar phase is positive, one gets a cross correlation of 0.73. For the evening when the lunar phase is negative, one obtains a quite similar value of 0.77 (Figure 4.2). The relative correlations are determined from a

simple least-square linear fit between the Moonshine deviation and crescent deviation using;

$$\frac{I_i - \bar{I}_i}{\bar{I}_i} = a_0 \times \frac{C_i - \bar{C}_i}{\bar{C}_i} + b_0 + \sigma_i,$$

(4.1)

where I_i is the observed fiducial patch intensity, C_i is the crescent intensity, $\bar{I}_i$ and $\bar{C}_i$ are the average fiducial patch intensity and crescent intensity, respectively, at the same lunar phase, and σ_i is the scatter about the linear least-squares fit. Note that throughout this Section $\bar{I}_i$ is the final, fitted intensity, which is derived by iterating the steps described in Sections 4.2-4.4. The coefficients a_0 and b_0 are derived from the least square fitting of Equation (4.1). From Figure 4.2, it is clear that a_0 is close to unity (morning/Grimali:0.81±0.08 and evening/Crisium:0.74±0.07, error is ±1σ), while the respective b_0's are essentially zero -- 0.002 and 0.001 -- more than two orders of magnitude smaller than a_0. That makes the second term on the right side of Equation (4.1) much smaller that the first. Therefore, one gets the correct relative zero airmass intensity, I_i', by removing the canopy effect. This is done by subtracting the linear term in Equation (4.1) from the Earthshine data;

$$I_i' = I_i - a_0 \times \bar{I}_i \times \frac{C_i - \bar{C}_i}{\bar{C}_i}.$$

(4.2)

The scattering among the data points is much reduced after this correction (see Figure 4.5b at the end of the Chapter). This correction is of comparable significance for the evening data (lunar phase < 0) and the morning data (lunar phase > 0), as the comparable cross-correlations imply.
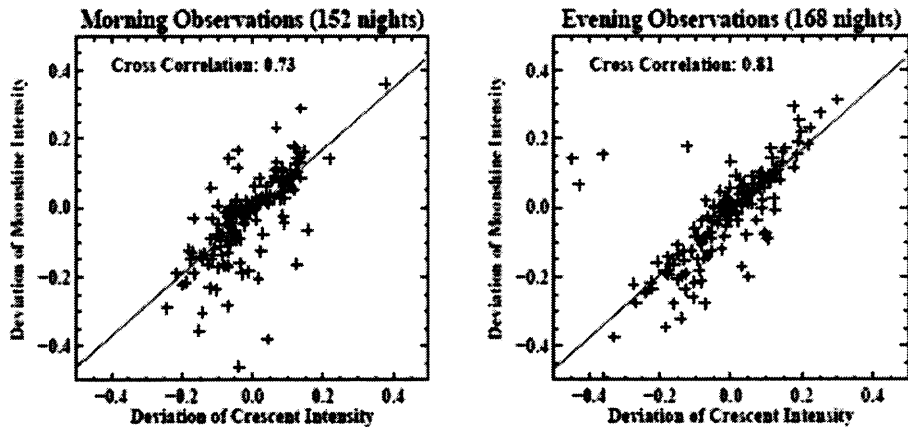
Figure 4.2 The deviation of the Moonshine fiducial patch intensity from average against the deviation of the overall intensity of the crescent. Left: data points from morning observations of Grimaldi; right: data points from evening observations of Crisium. The solid lines in each panel show the linear fit to each cluster of points.

4.3 Declination Correction

The second step in correcting the deficiencies in the apparent lunar phase function is to remove variations arising from the systematic change of relative position of the Moon to the plane of the Earth's orbit about the sun. The difference in right ascension between the sun and the Moon (hereafter, the "relative right ascension") changes from 180 to -180°, which essentially determines the lunar phase, defined as the angle from between the Moon-Earth line and the sun-Moon line, see Figure 1.1. However, there is an ambiguity in the lunar phase angle that makes the apparent lunar phase function multi-valued. In

detail, the difference in the declination between the sun and the Moon (hereafter "relative declination") changes as well, since the orbital plane of the Moon around Earth is inclined to that of the Earth around the sun. Toward the full Moon, the relative declination also becomes important in determining the lunar phase. Then, at the same lunar phase, but on different nights (that is, different months), the position of the Moon may be different, and this difference alters the readout intensity of the fiducial patches. To correct for this effect, for a given lunar phase near the full Moon, one chooses a standard position of the Moon and normalizes the readout intensity of different positions to this standard position. The standard position is the one for which the relative declination is zero, i.e., the Moon is in the plane of ecliptic, and the lunar phase is equal to the relative right ascension, i.e., a total lunar eclipse. The normalization is made as follows;

$$I_i - \bar{I}_i = a_1(P_i - P_{i,RA}) + b_1 D_i + c_1 + \sigma_i$$

(4.3)

where I_i is the observed intensity, $\bar{I}_i$ is the average intensity at the same lunar phase as I_i (from the ultimately determined lunar phase function), $(P_i - P_{i,RA})$ is the difference between the lunar phase and the relative right ascension, D_i is the relative declination, and a_1, b_1, and c_1, are fitting parameters, which are determined from the least-square fitting using all the observed intensities. The fitted parameters, a_1 (morning/Grimaldi: -0.003±0.002 and evening/Crisium: $3.4*10^{-5} \pm 7.0*10^{-5}$), b_1 (morning/Grimaldi: -0.47 $*10^{-5} \pm 0.0002$ and evening/Crisium: 0.0007 ± 0.0002) and c_1 (morning/Grimaldi: 0.009 ± 0.008 and evening/Crisium: 0.009 ± 0.009) are all quite small. All quoted errors

are $\pm$ 1σ. The normalized intensity, I'_i, is derived by removing the relative right ascension and declination;

$$I'_i = I_i - [a_1(P_i - P_{i,RA}) + b_1 D_i]$$ (4.4)

The c_1 term is regarded as part of the errors (σ_i).

This correction is only made for lunar phase between -15 and +15 degrees since the effect of the relative position of the Moon is only important around the full Moon. However, the modest improvement due to this correction reveals barely apparent changes in the data points.

4.4 Libration Correction

The third step in rectifying the apparent lunar phase function requires removing the effects of latitudinal and longitudinal lunar libration. Since the orbit of the Moon around the Earth is not in the equatorial plane of the Earth, a terrestrial observer alternatively sees the north pole and south pole of the Moon during each orbit. This is the latitudinal libration. Further, the slightly elliptical orbit of the Moon has the consequence that the Moon moves more slowly at apogee than at perigee, and therefore is seen to be wobbling around its axis of rotation. This is longitudinal libration. An additional, very small dynamical libration arises because the Moon is prolate, and it's pointing wanders. The dynamical libration adds to both the latitudinal and longitudinal librations. These librations allow an Earth bound observer to see about 60% of the Moon's surface. As a result of both kinds of libration, for different cycles of the lunar orbit, at the same lunar

phase, one would expect changes in the positions of the fiducial patches on the lunar disk. The readout intensity thus changes as a function of the geometric position of the fiducial patches on the lunar disk. The longitudinal and latitudinal librations cause the apparent lunar phase function to be multi-valued. To first order, a description was derived of the deviation of the observed intensity from the averaged intensity as a linear function of the longitudinal and latitudinal librations, which goes as:

$$I_i - \bar{I_i} = a_2 L_i^\alpha + b_2 L_i^\beta + c_2 + \sigma_i \tag{4.5}$$

where the $I_i - \bar{I_i}$ are the deviations of each night from the mean, and where L_i^α is the longitudinal libration and L_i^β is the latitudinal libration. Here, L_i^α and L_i^β really measure the position of the lunar pole in the sky with respect to its mean position, so that all the kinds of libration are taken into account. From a least-squares fit, one obtains the coefficients a_2 (morning/Grimaldi: 0.0019 ± 0.0004 and evening/Crisium: -0.0018 ± 0.0004) and b_2 (morning/Grimaldi: $4.2*10^{-5} \pm 0.0003$ and evening/Crisium: -0.0003 ± 0.0004), while c_2 is 1-2 orders of magnitude smaller than a_2. Again the third term on the right side of Equation (4.5) is small compared to the first and second. All quoted errors are $\pm 1\sigma$. Since the magnitude of the a_2's are about an order of magnitude greater than the b_2's, the longitudinal libration is more significant than the latitudinal libration. Figure 4.3 shows the result of fit, and, in particular, that the fit describes the data, in that it can be seen that the observed scattering at this step is mainly accounted for by the libration. For the determination of Figure 4.3, 152 mornings and 168 evenings were used, and the correlation between the fit and the data is 0.44/0.52, respectively. Using the parameters

from the fit, the intensities were normalized at all lunar phases to the case of zero libration with the equation;

$$I_i' = I_i - (a_2 L_i^\alpha + b_2 L_i^\beta)$$ (4.6)

To check the validity of the libration correction, one performs the libration correction again—but doing it before performing the atmospheric correction described in Section 4.2. Next the atmospheric correction was done (which still dominates), and the declination correction was done. At that point, the libration correction was done again. It was found that $I_i - \bar{I}_i$ does not have a significant correlation with the libration. In particular, the parameters from the linear fit of Equation (4.5) are reduced by an order of magnitude. This test not only confirms the validity of the libration correction performed above, but also guarantees that the three-step corrections can be performed in any order. However, it still remains to determine the lunar phase function for small phase angles.
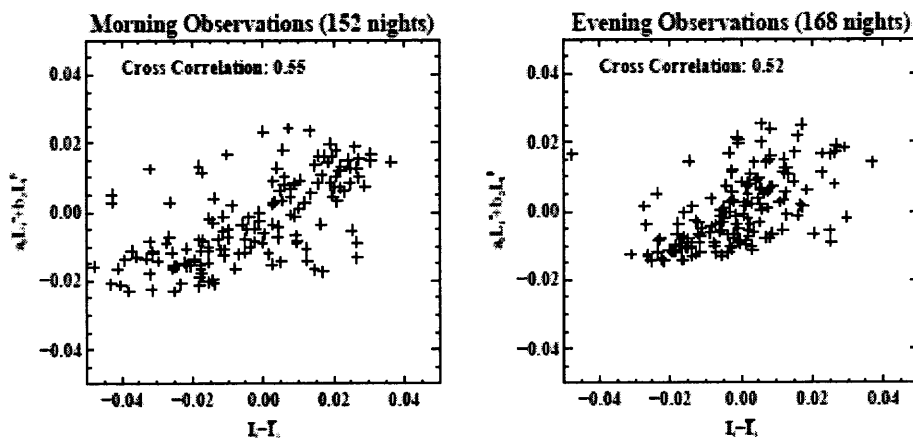
Figure 4.3 The deviation of the Moonshine fiducial patch intensity (after the first and second step corrections). Left: data points from morning observations; right: data points from evening observations.

4.5 Opposition Effect

To this point, the lunar phase function is incomplete because it is not normalized, and the functional form for the smallest phase angles have not been determined. To do these, one needs to know the phase function for small phase angles, and that means that the final lunar phase function for each fiducial patch needs to be normalized to the full Moon opposition peak. In reality, the Moon is not observable at zero lunar phase because the shadow of the Earth would occult the Moon, as the Earth's shadow occupies about ±0.8°. So far, the smallest phase the group has reached is ±1.0° on the night of November 29, 1993, when a total lunar eclipse occurred over Big Bear. On that night, the sky was clear and stable throughout, and observations were made both before and after the total eclipse covering lunar phase angles of magnitude ranging between about 1° and 2°, which offers a unique dataset to investigate the slope of the opposition surge effect for all fiducial patches on both the Grimaldi and the Crisium sides.

The images taken during the eclipse were processed, and the intensities of the fiducial patches were read out as described in Section 4.2. The atmospheric attenuation had to be corrected to obtain the real Moonshine intensity. However, throughout the night, the evolution of the Moonshine intensity was controlled not solely by the changing airmass, but also by the changing phase angle. This latter effect is appreciable because of the strong opposition effect at small lunar phase angles. As a result, the shape of the intensity evolution for the two patches deviates strongly, compared to the precision in the data, from Beer's law (see Figure 4.4a and c). Thus, Equation (3.1) can no longer produce a reasonable fit.

A simple solution to this problem was developed under the reasonable assumption that the opposition effect is linear for very small phase angles, say, from 0 to 5° (Hapke, 1971 and 1998). During the eclipse, the phase angle changes by less than two degrees for either the Crisium branch or the Grimaldi branch. To determine the slope of the opposition peak for each of the ten fiducial patches, one can represent the observed intensity by;

$$I_i = I_0 \times (1 - \gamma|P_i|) \times e^{-\alpha \eta_i}$$

(4.7)

where I_i is the observed intensity at phase angle $|P_i|$ (in degrees) and airmass . In contrast to Equation (3.1), I_o describes the intensity at both zero airmass and zero phase angle. The second term on the right side describes the linear increase of the phase function as the lunar phase goes to zero. The last term describes the exponential atmospheric attenuation; i.e., Beer's law, where α is the atmospheric extinction coefficient for the Moonshine.
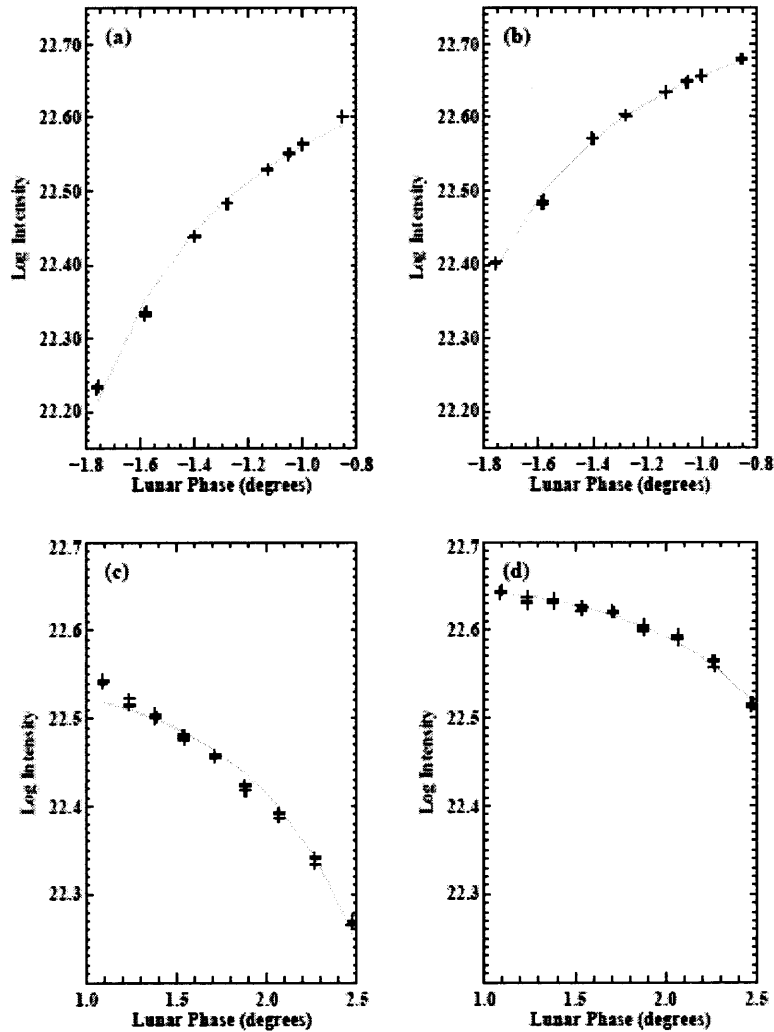
Figure 4.4 Fit of lunar eclipse data obtained on November 29, 1993. (a) Beer's law fit of the Crisium side (Equation 19); (b) Composite Beer's law plus opposition effect fit on the Crisium side (Equation 27); (c) same as (a) on the Grimaldi side; (d) same as (b) on the Grimaldi side.

In applying Equation (4.7), the observed I_i was used after correcting for libration (Section 4.4) at lunar phase P_i and airmass η_i in Equation (4.7) above, and made a least-squares, non-linear fit to obtain α, I_o, and the linear opposition effect coefficient, γ. While dealing with the very smallest phase angle data, the group made sure that all the points were outside the penumbral shadow of the Earth. The fit was made for all ten fiducial

patches. Correction was not made for the declination because the Moon was in total

eclipse, and that correction should be quite small. About 40 data points for the fit on

each side of the Moon were observed; i.e., before and after totality and the standard

deviation of the final fit was at the level of 0.5%. Figure 4.4b and d reveal the

improvement in fitting results for one pair of fiducial patches using Equation (4.7) instead

of Equation (3.1). The improvement is typical of that for all ten patches. From Figure

4.4, it is also clear that Equation (4.7) accurately describes the composite effect of the

opposition surge and Beer's law. The fitted opposition peak slope parameter, γ, was then

used to normalize the phase function for each of the fiducial patches. Figure 4.5 shows an

example of the final lunar phase function normalized to the opposition peak. Of course,

each fiducial patch has its own lunar phase function. In detail, for lunar phase of 5° in

Figure 4.5, the slope γ, was determined for very small angles to extrapolate to the

intensity at zero lunar phase from that at 5° $\left(I(0) = \frac{I(5)}{1 - \gamma \times 5} \right)$. Then, that branch of

the phase function was normalized using its γ and *I(0)*=1 to fix *I(5)*. Combining the

knowledge of *I(5)* with the relative phase function indicated by the +'s in Figure 4.5, the

right branch of that figure was obtained. The normalization removes the ratio of the

geometrical albedos between the two patches, which is restored in Equation (4.8). The

eclipse does not give data for lunar phase 2° < |θ| < 5°, where a linear form for the phase

function has been assumed. Nights at these small phase angles occur at the fullest of full

Moons, and there are as yet only a few observations. Special emphasis has been made to

observe at these phases so that the phase function in this range can be better defined. If

there were a systematic error here, it would shift all of the Bond albedos by the same

amount. One expect that such a systematic error is actually quite small, but would be better able to re-calibrate present results in the light of future data.

The value of γ, the derived opposition coefficient for all fiducial patches is approximately 0.08 per degree, indicating that when lunar phase changes from six degrees to zero degrees (full Moon), the intensity doubles. This is the well-known opposition surge which had not been quantitatively determined previously but already estimated by Hapke (1971) and other more recent works. The standard deviation in the determination of γ is about 0.5%.

In Figure 4.5, the lunar phase function is shown with final fit in the lowest panel. The same fit is shown in the other three panels, as well. The points in the top panel represent a normalized version of Figure 4.1. The second panel shows the result after correction for local atmospheric effects, which is the largest correction. The third and fourth panels show the effects of lunar declination and libration, respectively. The lunar phase function is produced from a fifth degree weighted polynomial fit to the corrected data. After each step of correction, the standard deviation of the fit is reduced from originally 0.05/0.05 (evening/morning) to eventually 0.01/0.01, with the phase function normalized to unity. A restricted regularized fitting is performed as well, which parameterizes the intensities at 181 bins (corresponding to lunar phase 0° to 180°).

These 181 parameters from the fitting describe the lunar phase function, in that the intensity of any lunar phase is the linear interpolation between the values at the two grids into which the lunar phase falls. Note that since there are no data points beyond 150°, the phase function fit beyond this range is not reliable. Similarly, there are not enough data points within ±5°, and so, the eclipse data was used to determine the fitted

peak in Figure 4.5 by treating opposition effect at small phase angles (near the full Moon). From the final fit, the estimated error of the mean is at the level of 0.5%; thus, the lunar phase was measured to 0.5%.

One may ask how does the phase function in the lowest panel of Figure 4.5 compare with earlier efforts to determine it, like those of Danjon? Figure 4.6, is a plot of Danjon's fitted phase function against the ES group's corrected one. The smallest lunar phase angle measured by Danjon was only 11°. Danjon used slightly different fiducial patches, but that is not the source of differences, because the phase function shown is about the same for all of the modern fiducial patches. Rather, the primary source is the opposition surge which was unknown in Danjon's time. There is a clear offset in the Danjon phase function which would yield uniformly higher albedos than the true phase function. For the modern phase function, the erroneous overestimate has been eliminated (on the order of ~20%).
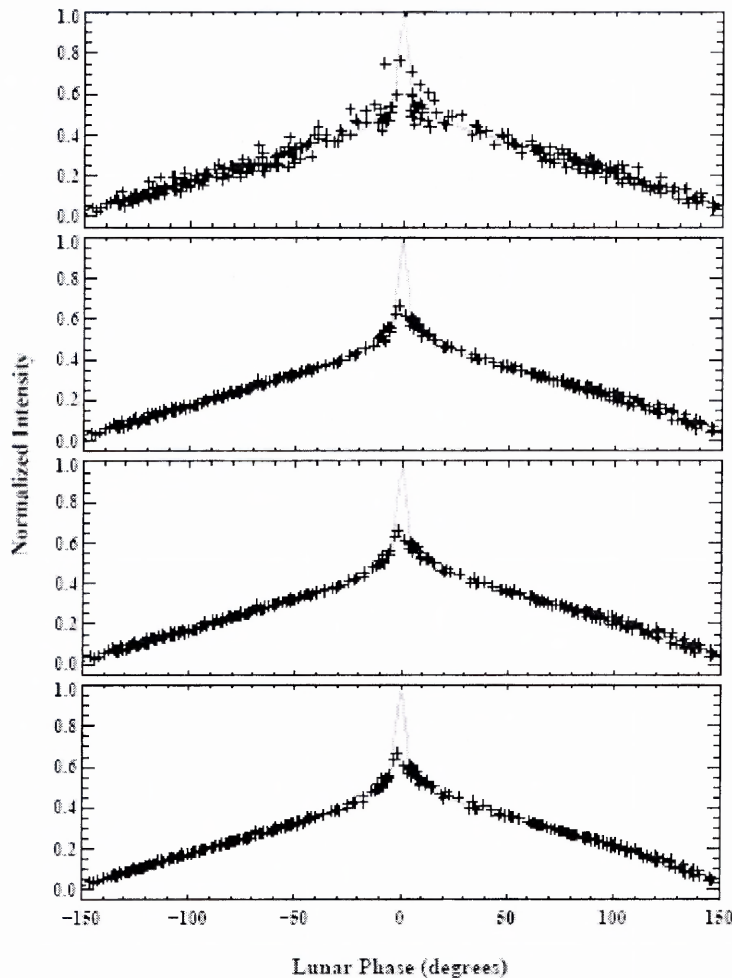
Figure 4.5 The top panel shows the apparent, relative lunar phase function from the raw data, for which there are points down to 2°. The function is made relative by normalizing it to unity at phase angle 0°, which means that the ratio of the true right and left branch intensities yields the ratio of the geometrical albedos between Crisium and Grimaldi. The peak near small phase angles represents the opposition effect. Data from a total eclipse are used to connect the positive and negative phase branches of the lunar phase function. No eclipse data are shown in this figure, but the result of the eclipse data is the opposition peak. The second panel from the top shows the result after including correction for the local atmospheric effects using the lunar crescent as a photometric reference star. The third panel also includes the correction for lunar declination. The fourth panel includes the correction for lunar libration. The fit shown in each panel is the final fit to the data after all the corrections described in Section 4.5 have been performed.
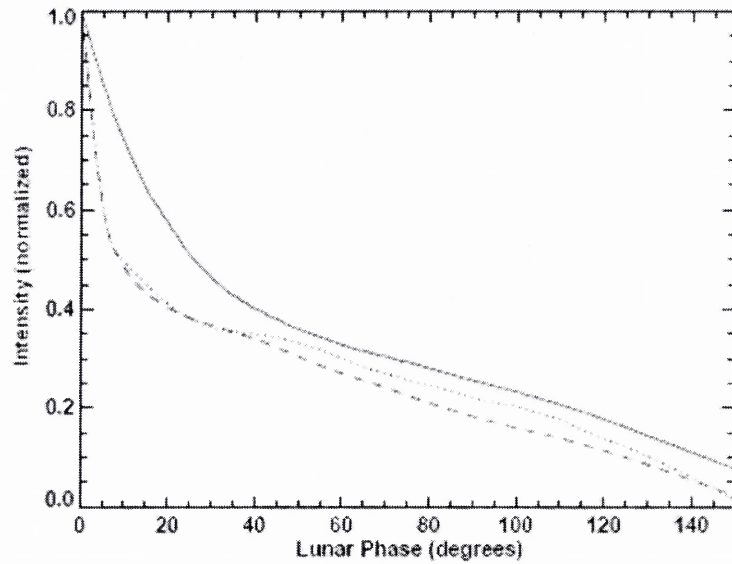
Figure 4.6 Danjon's phase function (solid line) is plotted against lunar phase. Using Figure 4.5d, the dashed line is the modern phase function for evening observations and the dotted line for morning for the fiducial patch of Figure 4.5.

CHAPTER 5

PRECISION OF THE DETERMINATION OF THE NIGHTLY EARTHSHINE MEASUREMENTS

The apparent albedo for an individual night is calculated from the Earthshine measurement for that night by combining equations (4.2) and (2.13):

$$p^*(\beta) = \frac{3}{2f_L} \frac{p_b f_b(\theta)}{p_a f_a(\theta_0)} \frac{I_a/T_a}{I_b/T_b} \frac{R_{em}^2}{R_c^2} \frac{R_{es}^2}{R_{ms}^2} \qquad (5.1)$$

where $\frac{I_a/T_a}{I_b/T_b}$ is the ratio of the Earthshine intensity to the Moonshine intensity in two opposing fiducial patches, after correcting for airmass. The ratio between the physical reflectivity of the two opposing fiducial patches, p_b/p_a, is determined from the lunar eclipse data taken at BBSO on November 29, 1993, as discussed in the previous Chapter. The lunar phase function for the bright side, $f_b(\theta)$, is used in the formula to account for the geometrical dependence of the reflectivity of the Moon, while $f_a(\theta_o)$ accounts for the fact that the Earthshine is not exactly retro-reflected from the Moon ($\theta_o \leq 1°$). In the analysis, θ_o is taken as the angle between the observer's position and the mean of the sub-solar point (position on the Earth's surface of the solar zenith) and the sub-lunar point (position on the Earth's surface of the Moon's zenith) with the apex of the angle being defined with respect to the fiducial patch under consideration, see Figure 1.1. It is assumed that the Moonshine and Earthshine have the same lunar phase function for each fiducial patch. Thus, taking $f_a(\theta_o)$ from the appropriate Moonshine phase function. The

Earthshine is slightly bluer than the Moonshine because of Rayleigh scattering by the Earth's atmosphere. This small effect is subsumed in the lunar geometrical albedos.

From Equation (5.1), one may surmise that the observational errors arising from measuring p^* from two opposing fiducial patches come from the errors in the readout intensity from the Moonshine and Earthshine fiducial patches, the error in the transmission of the bright side filter (about 0.8%, see Chapter 7 for details), and the error in the determination of lunar phase function. The ratio p_b/p_a can be regarded as the relative normalization of the phase functions of the opposing fiducial patches. The standard deviation of the lunar phase function can be determined down to 0.5% from a co-variance calculation with a comparable uncertainty for the ratio p_b/p_a. The standard deviation of the Beer's law fitting of the Moonshine for each night is taken as the error of the Moonshine intensity. This gives a value of 1.1%. For the case of the Earthshine, the scattering of the data is due to both the noise and the real physical changes in the terrestrial albedo. The average standard deviation from Beer's law fitting of the Earthshine intensities is 1.9%. Conservatively speaking, if half the amount of such scattering comes from the real physical change on average, the error (σ) in nightly Earthshine intensity measurement is about 1.0%. Adding up all the errors and assuming they are independent, one gets a nightly measurement error of nearly 2%. Regarding the measurements from different pairs as being independent, the 2% is reduced to about 1%.

The precise determination of the apparent albedo for one night cannot yield a bond albedo; rather, one needs to integrate the apparent albedo for many nights (over as wide a range of lunar phase angles as possible). Combining nights to obtain, say, a seasonal average, then the total error will be smaller, but no smaller than that associated

with the mean values of the various lunar phase functions and their relative normalizations. The determination of the ratio p_b/p_a is regarded as being the most likely source of systematic errors. Measurements of the opposition effect in future eclipses will allow the group to determine if there are systematic errors, and correct the albedos in retrospect.

To determine the Bond albedo, A, from the Earthshine observations one needs to integrate $p^*(\theta)$ over all phases of the Moon. Combining Equations (3.5), (3.6) and (4.2), it is found that;

$$A = \frac{2}{3} \int_{-\pi}^{\pi} d\theta p^*(\theta) f_L(\theta) \sin\theta$$

(5.2)

With the single Earthshine station at Big Bear, the 'global' albedo covers an area slightly larger than 2/3 of the Earth. This partial coverage will increase when more Earthshine stations are in operation.

There are two basic problems using this approach to determine the Bond albedo. The first, and more significant problem, is that one cannot measure the Earthshine for all phases of the Moon. This becomes a problem mainly for lunar phases near the new Moon, where the sunlight reflected by the Earth is primarily in the direction of backward scattered radiation. Later it will be shown that one can obtain a quite reliable Bond albedo from the Earthshine data with the help of the simulations. The second basic problem in using the Earthshine to determine the albedo arises because the orbit of the Moon traces

out an ellipse in the full three dimension space surrounding the Earth, so one cannot measure the Earthshine in all directions. Therefore, the Earthshine observations are insensitive to any azimuthal anisotropy that might be present in the Earth's albedo. It will be shown that, according to the ES group models, the anisotropy may not be significant, and one can account for it. This is done by taking advantage of full spatial coverage provided by the simulations. It is possible however that at present the ES group models are not sensitive enough to detect the anisotropy effect.

CHAPTER 6

EARTHSHINE INSTRUMENTATION AND DATA ACQUISITION

6.1 Hardware

Earthshine observations are currently being carried out at BBSO. The author was the primary observer at BBSO from October 1998 to January 2002. The Earthshine telescope is aligned with, and mounted atop the 65 cm solar telescope. Figure 6.1 shows a schematic of the Earthshine telescope.

The basic optical components of the Earthshine telescope consist of an f/15 telescope primary, which is a 15 cm diameter air-spaced doublet. The telescope tube is attached and aligned with the 65 cm solar telescope, which enables the use of the large telescope's drive software, permitting tracking following the Moon's variable rate. The tracking rate is updated, via software, every thirty minutes to match the changing lunar motion in the east-west direction. Minor north-south corrections are done with the telescope control paddle as needed during the course of the night's observations. The 65 cm telescope is regularly re-balanced for equipment changes so that tracking stability is not a problem even with long exposures. At the end of the tube is a stray light field stop. The incoming Moonlight passes the field stop, and then enters a light-tight optical assembly box that holds the filters and camera optics.

In the box, just behind the tube field stop and just before prime focus, is the Earthshine neutral density filter switcher. Two filters are placed in the switcher. The first neutral density filter is a Schott NG3 2mm. The laboratory measured transmission of this filter used for the first two years of observations was 0.0115, integrated from 4000-7000 ´ for the bright side (BS) measurements. The BS or Moonshine filter covers

the entire field of view and is used to prevent camera saturation, and to provide a reasonably long exposure time (several 100 ms) compared to the smallest exposure time for the camera (10 ms). Thus, to determine the absolute value of the Earth's reflectance, one needs to know precisely the transmission of this filter. The second filter is a Schott NG10 2mm. This filter's transmission is about 2×10^{-5} over 4000-6000 $'$, although it's precise value is irrelevant for the observations. The NG10 is essentially a blocking filter to cut off the bright side of the Moon to permit the dark side or Earthshine (ES) observations. The blocking filter covers the bright side of the Moon to permit long, dark side exposures (~60-150 s) to get optimal signal to noise for the ES images. The blocking filter is carefully placed within the filter holder, by hand, at the beginning of each observing session. Its location is designed to cover the terminator, depends on the phase and libration of the Moon. Quickly setting the position of the blocking filter was a very necessary skill especially in the "morning" observations. When the Moon rose in the east crucial high airmass information could be lost if the observer spent too much time adjusting the angle and position of the blocking filter.

The prime focus is after the filter holder, and it is closely followed by a flat field lens. Next in the optical train are two near IR filters, which stop any light beyond 7000 $'$ from reaching the camera. An iris behind the near IR filters acts as a further stray light (Lyot) stop. Behind the iris is a camera lens that focuses the lunar image on the CCD. Between this lens and the camera is a space for a second filter wheel (not shown), which can be used for narrow band measurements. All elements are rail mounted for linear adjustments, and lens elements are in movable *y-z* mountings for fine adjustments. All fine-tuning was done in the fall of 1998, and nothing has been changed on the system

since the start of data acquisition in December 1998. The system was "frozen" to limit possible errors in calibrating the lunar phase function. The one exception was the replacement of the BS filter in October 2000 (see Chapter 7). Flat field images help to point out the location of occasional dust particles that get into the optics. Compressed air removes most particles, and when necessary, elements are removed for cleaning, and then are carefully replaced to preserve optical alignment.
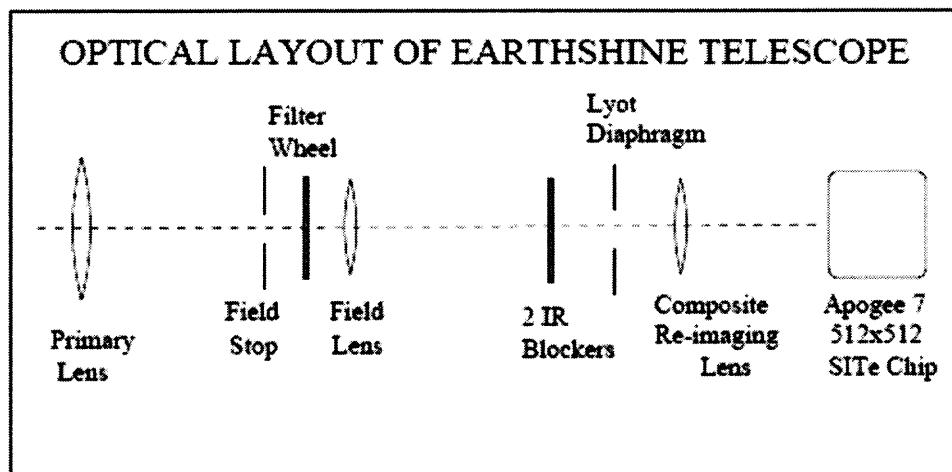
Figure 6.1 The optical set-up of the Earthshine telescope.

The CCD camera used in the current Earthshine observations is an Apogee 7. The camera is a 512 X 512 16-bit scientific system with a SITe back-illuminated, thinned silicon chip. This chip, which is one of SITe's highest grade, is designed for higher quantum efficiency than un-thinned front illuminated chips—this advantage is most apparent toward the blue. One drawback of the higher efficiency SITe chip is its sensitivity to "after-images" caused by image persistence. The SITe chips were known to suffer from Residual Surface Image. Signal charge is trapped in the Silicon/Silicone Oxide interface. Testing the Earthshine system to limit this effect resulted in the following observing procedures: 1) The UV from the BS images is reduced by the BS

(NG3) filter. 2) The worst after-images show up in the ES images on the unfiltered half of the image—which are of long exposure. It was found that a series of subsequent, short BS images, the residual image was removed before the next long Earthshine exposure. 3) Careful examination of dark current and flat field images taken during the course of observations is done to confirm this, night by night.

Initial testing demonstrated a linear response over the camera's entire 16-bit range. To check for change in the camera's response with time, a calibrated radiometer was purchased to check the camera's response during each new Moon. Dome flats are taken in varying illumination to get pixel count versus intensity. The radiometer is an IL 1700, a NIST traceable Silicon photodiode radiometer. Every couple of years, the radiometer is returned to International Light for re-calibration.

6.2 Observations

After initial tests, the current round of Earthshine observations began in December 1998. A typical raw image is shown in Figure 3.1. The five pairs of fiducial patches used in the data reduction (see Chapter 3) are also indicated. The camera's graphical user interface, in C code, was supplied by the manufacturer, and it was modified to efficiently handle the routine Earthshine observations. The nightly observations follow a simple set of procedures, which are mostly automated. During the course of observations BS, ES, dark current and flat field images are taken regularly.

The first eight months of observations covered lunar phases between 0° and 140°, which is about 21 days a month. The initial observation over this wide range of phases was necessary to determine the lunar phase function and prove its repeatability. During

the first eight months, for the phases near the full Moon (-40° through 0° to +40°), ES images were not taken because both fiducial patches were in, or so near to sunlight that ES measurements were unreliable (see Figure 1.1). On these long nights only BS, dark current, and flat fields, were taken to determine the scattering of light from the fiducial patches as a function of the phase of the Moon. The lunar phase function was determined by July 1999, so that the BS only nights were dropped except for observations of the full Moon. Full Moon observations are still taken to determine the role of the opposition effect (Flatte' et al. 1991) in the lunar phase function (phases -15° to +15°). Current Earthshine observations cover about 14 days per month. Observations cover lunar phases between ±40° to ±150° centered on the first and last quarters of the Moon when one has optimal conditions for measuring the Earthshine close to full-Earth with a few hours of observations being possible. Data rates vary depending on phase. An average night will give about 1 image per minute. This means that the number of raw images saved for data reduction, varies from 100 to 600 per night.

CHAPTER 7

MEASURING THE TRANSMISSION OF THE BRIGHT SIDE FILTER

A precise determination of the Earth's reflectance from observing the Moon depends on an accurate measurement of the ratio of the true Earthshine intensity to the true Moonshine intensity. This determination is complicated by the fact that the Moonshine is so bright that when it is measured, one must use a filter (see Figure 3.1) that reduces the intensity of the Moonshine by about 99%. The reduction enables a reasonably long exposure time (on the order a few 100 ms) compared to the shortest possible exposure time of the camera (10 ms). When observing the Earthshine, the Moonshine or BS filter is removed and the much stronger, blocking filter is inserted to block the Moonshine to prevent camera blooming during the much longer exposures. Thus, to know the true ratio of the Earthshine to Moonshine intensity, one must also precisely determine the transmission of the Moonshine filter at the point through which the Moonlight passes (point-to-point variations could well be significant). This fact became abundantly clear after October 13, 2000 when the original filter was destroyed (dropped), and was replaced by one that was comparable in the lab specifications for the transmission over the whole filter. Initially, it was assumed that the transmission of the new filter was the same as the old one. However, it was soon found that the observed Moonshine intensity noticeably increased, indicating that the new filter had a significantly larger transmission than the old filter.

In the observations, the Moonshine filter (BS) is placed at a fixed position in the focal plane covering the entire lunar image, so that the light always passes through the

same point on the filter. This is important because there is some point-to-point variation in the transmission of the filter. In the effort to precisely determine the transmissions of the old and new BS filters at the focal point of the lunar image, identical approaches were employed for both of the filters. To measure the transmission of the old filter, the group re-analyzed thirty nights of Moonshine and Earthshine data that were reduced for nights near the new Moon - where the Earthshine signal is most intense. To illustrate the re-analysis procedure, see Figure 7.1. For that night, with the old filter, the total Earthshine intensity in five parallel strips was measured. These strips were somewhat wider than the fiducial patches and ran from the Earthshine fiducial points toward the Moonshine crescent. In Figure 7.1, the five strips are shown together as a striped, bright, four-cornered patch. Each strip in the bright patch runs from the edge of the Moon and is 5° wide in latitude and 30° long in longitude. That way, each strip would have a statistically significant number of counts in the Earthshine region, even for the relatively short exposure times of a few hundred milliseconds. The lunar phase in Figure 7.1 is +134°. Large magnitude phase angles are chosen so that the Earthshine is the brightest, while the stray light the smallest. The determination of the transmission of the old BS filter is shown for that typical night in Figure 7.2. The dark side of the Moonshine and the Earthshine intensities are each extrapolated to zero airmass and corrected for the small effect of stray light, and their ratio yields a transmission of 0.0114 ± 0.005 for that night. The error weighted mean transmission for all thirty nights is 0.01127 ± 0.00011 for the old filter. Implicit in this approach to determining the broadband transmission of the filter is the assumption that the spectrum of the Earthshine and Moonshine are roughly the same; this assumption works here because the transmission curve of the filter is flat over visible

wavelengths. Most of the noise in the result arises from the short exposure time for the BS filter covered observations. The 0.01127±0.00011 is within the factory quoted value of the 0.0115 given by Schott. The tolerance range over the 4000-7000 ′ range of the observations is ±2%.
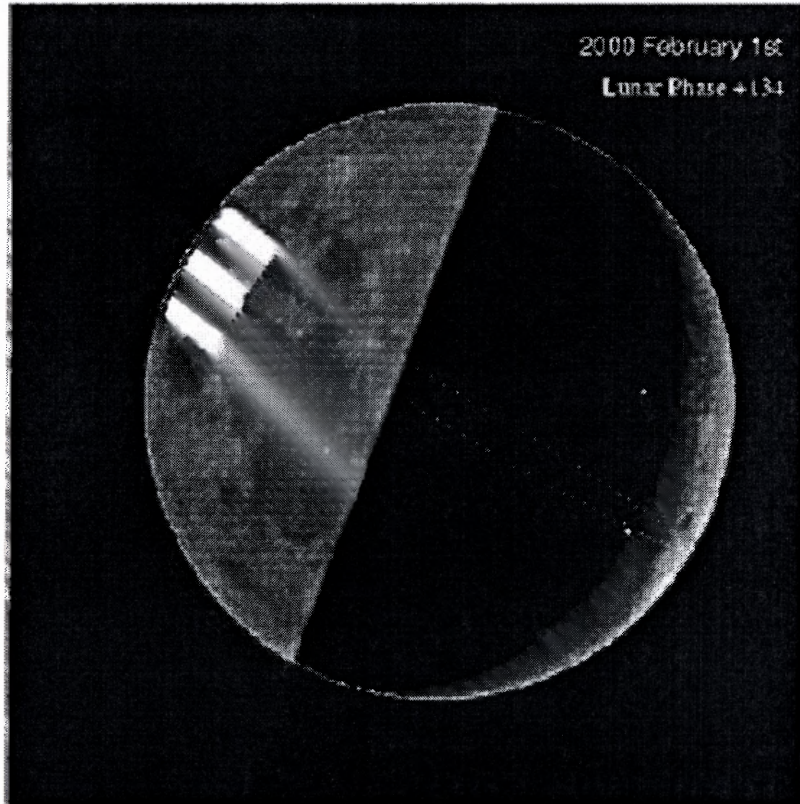
Figure 7.1 This image of the Earthshine on the night of February 1, 2000 shown is one with the blocking filter, which enables long exposures of the Earthshine. The bright, rectangular patch indicates the area of five strips used to compare the Earthshine intensity with and without the Moonshine filter (BS filter), so as to determine the transmission of the BS filter. The lunar phase was +134° that night, and so the Earthshine signal is relatively strong. The crescent is not visible through the strong blocking filter in the original image, but has been restored here for reference.

For the new filter, twelve nights of data were re-analyzed in the same way and a transmission of 0.01338±0.00017 was found for the focal point, whereas the factory-reported average across the filter was 0.0114. The latter transmission is nearly identical

to that of the old filter, but quite far from 0.01338±0.00017. The larger transmission at the focal point accounts for the apparent rise in Moonshine intensity after October 13, 2000. The group will continue collecting more information on the transmission using future data.
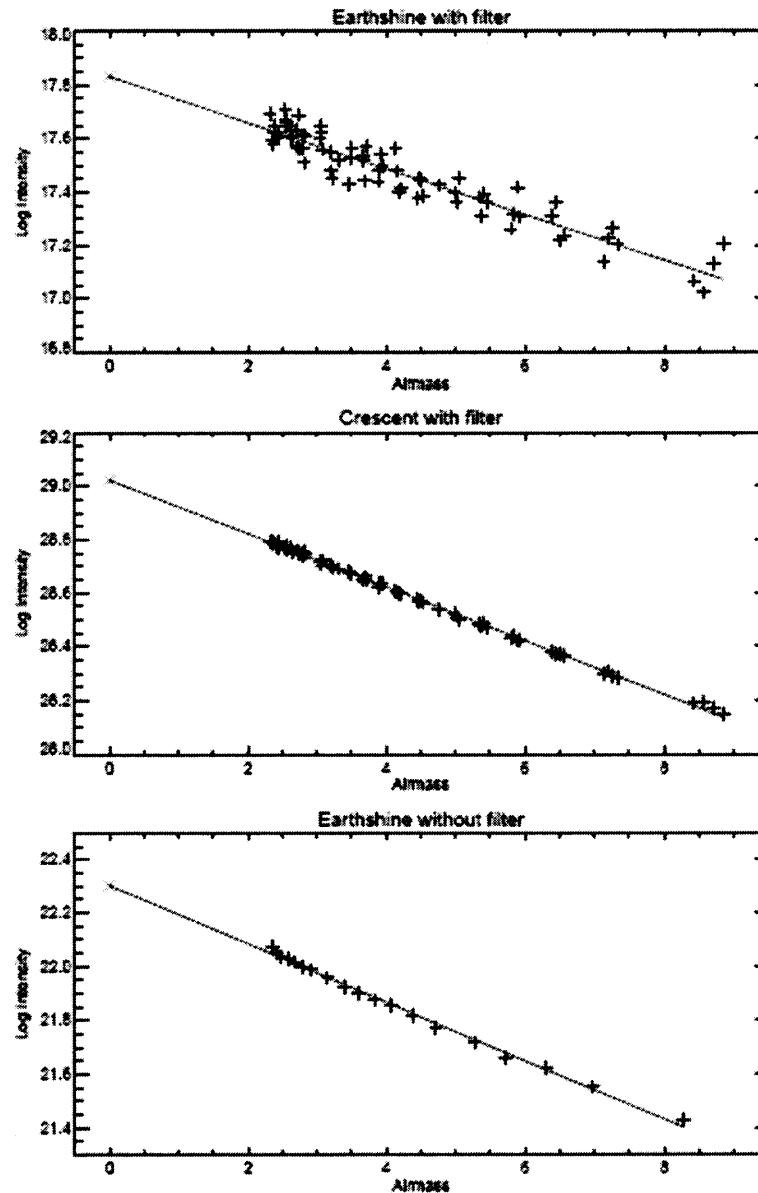
Figure 7.2 The upper panel shows the BS filter-blocked Earthshine intensity as a function of airmass on Feb. 1, 2000. The "+" signs represent the intensity of one of the stripes. The linear fit to the data has been extrapolated to zero airmass. The lower panel shows the same type of data, but without the BS filter. The ratio of the two intensities, implies a BS filter transmission of 0.0114±0.0005.

However, there is a more powerful and more precise cross-check using lunar phase function data on the crescent and Moonshine, which as mentioned before is known to 0.5%. Analyzing all of the good nights of Moonshine observations, with the new and old new filter, at all phases, a "test" lunar phase function was constructed. From all the good old filter nights, a second-degree polynomial was fit to the lunar phase data. The data for these nights was reduced using a transmission value of 0.01127. After that, the phase function for the nights taken with the new filter are used to calculate the standard deviation of the values to the lunar phase function fit to the old data, but leave the new filter transmission as a variable.

The procedure consists of multiplying the intensities of the new phase function data by a factor between 0.9 to 1.4 in steps of 0.0001, and for each case calculating the standard deviation to the old data fit. The agreement of the new data with the fit to the old data will be optimal when the standard deviation is minimized.

It was found that the best agreement between the two lunar phase functions was when the transmission of the new filter was 0.0132 (0.01319 for the Moonshine and 0.01322 for the crescent). This is excellent agreement with the transmission determined from the first method. Thus, the transmission of the new filter has been determined to the same precision as the old filter, so that 0.0132±0.0001 is used as the transmission after including errors in the phase function. As more data is gathered on the new filter, one can determine its transmission to the same precision to which the lunar phase function is known. Then the error on the transmission can be reduced to about ±0.00005.

CHAPTER 8

MODELING THE BOND ALBEDO

8.1 The Bond Albedo

Since late 1998, the group has been making sustained measurements of the Earth's reflectance by observing the Earthshine from Big Bear Solar Observatory. During that time, the group has also simulated the Earth's reflectance -- for both the parts of the Earth in the Earthshine and the whole Earth. The simulations employ scene models of the Earth from the Earth Radiation Budget Experiment (ERBE), simulated snow/ice cover, and near real-time satellite cloud cover data. Broadly, the simulations and observations agree. However, there are important and significant differences, with the simulations showing more muted variations.

In principle, there is sufficient information to determine a Bond albedo from the simulations by using scene models of the Earth and adding cloud cover data from satellites and snow/ice cover from models. However, a precise determination is no easy task. In particular, the treatment of the clouds is probably a bit oversimplified, and other climate parameters, beyond snow and ice, are ignored that might contribute to changes in albedo. Further, the ERBE model contemplates only 12 different scenes and 4 cloudiness levels (0-5%, 5-50%, 50-95% and 95-100%). Beyond the appreciable binning of the cloud cover, changes in cloud type or cloud optical thickness, for example, will also affect the albedo, but these are not accounted for in the models. Thus, the albedo models presented here need to be considered only as a first order, or starting, approximation to the problem.

In general, the Bond albedo is given in terms of the albedo of each element of the Earth's surface by;

$$A = \frac{1}{\pi R_e^2} \int d^2 R (\hat{R} \cdot \hat{S}) a$$

<div align="right">(8.1)</div>

where d^2R is an element of the Earth's surface, $\hat{R}$ is a unit vector pointing toward the local zenith, and $\hat{S}$ is a unit vector pointing toward the sun. The albedo of each surface element, a, depends on the surface type, cloud and snow/ice cover and solar zenith angle. Further, there is an anisotropic factor that gives the angular distribution of the reflected radiation and depends upon the reflected zenith angle and azimuth. The integral is over all portions of the globe illuminated by the sun (i.e., $\hat{R} \cdot \hat{S} \geq 0$). However, to compare the simulations with the observations, one has to consider the ratio of the Earthlight to sunlight, Γ, that would be seen by an observer on the Moon.

There is a systematic variation of Γ throughout the lunar month. When the Moon is nearly new (lunar phase $\theta \approx \pm\pi$), the Earth is nearly full, and so Γ is relatively large ($\approx 10^{-4}$). Conversely, when the Moon is nearly full ($\theta \approx 0$), the Earth is a thin crescent and Γ becomes vanishingly small. Fluctuations of Γ about its systematic behavior are caused by varying terrestrial conditions, including weather, the seasons and climate change. The lunar phase θ is defined in Figure 1.1. After correction for the dependence of the reflectivity on lunar phase, one obtains;

$$\Gamma = \frac{1}{\pi R_{em}^2}[\frac{R_{ms}}{R_{es}}]^2 \int_{(\hat{R}\cdot\hat{S},\hat{R}\cdot\hat{M})\geq 0} d^2R(\hat{R}\cdot\hat{S})a(\hat{R}\cdot\hat{M})L$$

(8.2)

where $\hat{M}$ is the unit vector pointing from the Earth toward the Moon, and the integral is over all of the Earth's surface for which the sun and Moon are simultaneously above the horizon (i.e., $\hat{R}\cdot\hat{S}$ and $\hat{R}\cdot\hat{M} \geq 0$). The anisotropy function, L, generally depends on surface type, cloud cover, and the zenith angles and relative azimuth of the sun and Moon. L is defined so that it is unity for a Lambert surface (see Equation (4.1)). The apparent albedo, p^*, of the partly sunlit Earth disk observed by way of the Moon can be related to the normalized bi-directional reflectance factor $R = \pi N/M$ used in Earth radiation budget studies from satellite data, where N is the reflected radiance observed in a particular direction from a small region and M is the reflected flux through a horizontal surface in that same region, so that the Earthshine-derived p^*, is a sort of weighted average of R. In terms of Equation (4.3);

$$p^* = \frac{3}{2f_L}\Gamma\frac{R_{em}^2}{R_e^2}\frac{R_{es}^2}{R_{ms}^2}$$

(8.3)

Because Γ is the ratio of the Earthshine to Moonshine intensity that would be seen by an observer on Earth looking at the Moon, there is no dependence on lunar reflectivity.

Thus, the models enable one to simulate for a given night (or a subset of time during one night) the Bond albedo of the Earth, and the apparent albedo that would be seen from BBSO.

8.2 The Models

In modeling the reflectance properties, a and L, of the Earth, scene models developed for the ERBE observations (Suttles et al., 1988) were used. As mentioned, a and L are tabulated for twelve model scenes, varying from "desert" (areas for which the annual precipitation is less than 26 cm) to "mixed land-ocean" areas, which are cells bordered by two land and two ocean cells. For the snow/ice cover, simulations from the Canadian Center for Climate Modeling and Analysis (CCCM II; www.cccma.bc.ec.gc.ca) were used. This Gaussian grid spacing is roughly 2.8°x 2.8° in longitude and latitude. The model gives the monthly mean snow/ice cover for each grid cell. The simulations of the Earth's albedo were performed using two different cloud cover data sets.

The primary dataset for the model calculations is uncalibrated images of the global cloud cover produced by the Weather Services International (WSI) Corporation. This data is used in the simulations of the BBSO observations. The WSI Corporation is the only place known that is currently producing near real-time, on-line publication of global cloud cover maps. WSI maps (www.intellicast.com) are composed of data from both geostationary and polar orbiting satellites. Data from multiple orbits are mosaiced together to provide wide-scale global and full Earth views in a single image. To allow for continuous night and day viewing of cloud patterns, infrared imagery is used. The group downloads and calibrates WSI images daily.

The daily (D2) and monthly (D2) mean fractional cloud cover data from International Satellite Cloud Climatology Project (ISCCP) is also being used. The presently released ISCCP dataset covers 18 years over the period July 1983 through September 2001. The ISCCP dataset makes use of visible and infrared radiances; total

cloudiness is determined using both of them, whereas the various cloud types are determined using infrared radiances only. For further details on the ISCCP data see Rossow et al. (1996). All ISCCP data products are archived at the ISCCP Central Archive (isccp.giss.nasa.gov).

Where the ISCCP cloud data is given in percentage cloud coverage, the WSI images download from the web are given in arbitrary units, and it is necessary to translate them into fractional coverage. The daily WSI images are each placed on a ``T42" square grid (2.8°x 2.8°), as are the ISCCP data. The group uses the ``T42" square grid because this is the format for snow and ice data, albeit one of the most common formats for climatological data. WSI monthly mean cloud cover maps (values are in arbitrary units) have been generated, and compared to the ISCCP monthly mean maps (in units of fractional cloud cover). Primarily, the search is for completely overcast areas. The program finds those areas with the minimum number of counts in the WSI images and assigns 100% cloud cover for any number of counts equal or greater to this minimum. The program also looks for clear sky scenes and assigns a maximum number of counts in WSI images below which are considered to be 0% cloud cover. The values between the maxima and minima are converted to percentage coverage units using a simple polynomial parameterization. This yields an empirical non-linear calibration curve between the two cloud datasets, by which WSI daily maps in arbitrary units are converted into ISCCP fractional coverage, although this does not translate into a one-to-one correspondence between the two datasets. Important differences between the two still occur. The use of a different calibration curve can altogether increase or decrease the mean albedo, but cannot increase the muted seasonal variations derived from the models.

CHAPTER 9

COMPARING DAILY OBSERVATIONS AND MODEL RESULTS

Figure 9.1, shows evening and morning Earthshine observations overlaid on model calculations covering the entire day. The two lower panels show the Earthshine as a function of time. The solid curve shows the variation of the calculated apparent albedo p^* during the twenty-four hour period and the solid boxes are the observed apparent albedo. These results come from near to a quarter Moon, and are compared with the Earth-wide WSI cloud cover from the same day in the top panel.

The top panel shows the cloud cover maps, illustrating which parts of the Earth contribute to the Earthshine. Highlighted (the large bright areas) are those parts of the Earth that are the source of the Earthshine. The cloud cover is also shown as secondary grayscale, for instance, the east-west dark bands just north and south of the equator illustrate cloudless areas. Also indicated with boxes is the point of equal angles, where the angle of incidence is equal to the angle of reflection.
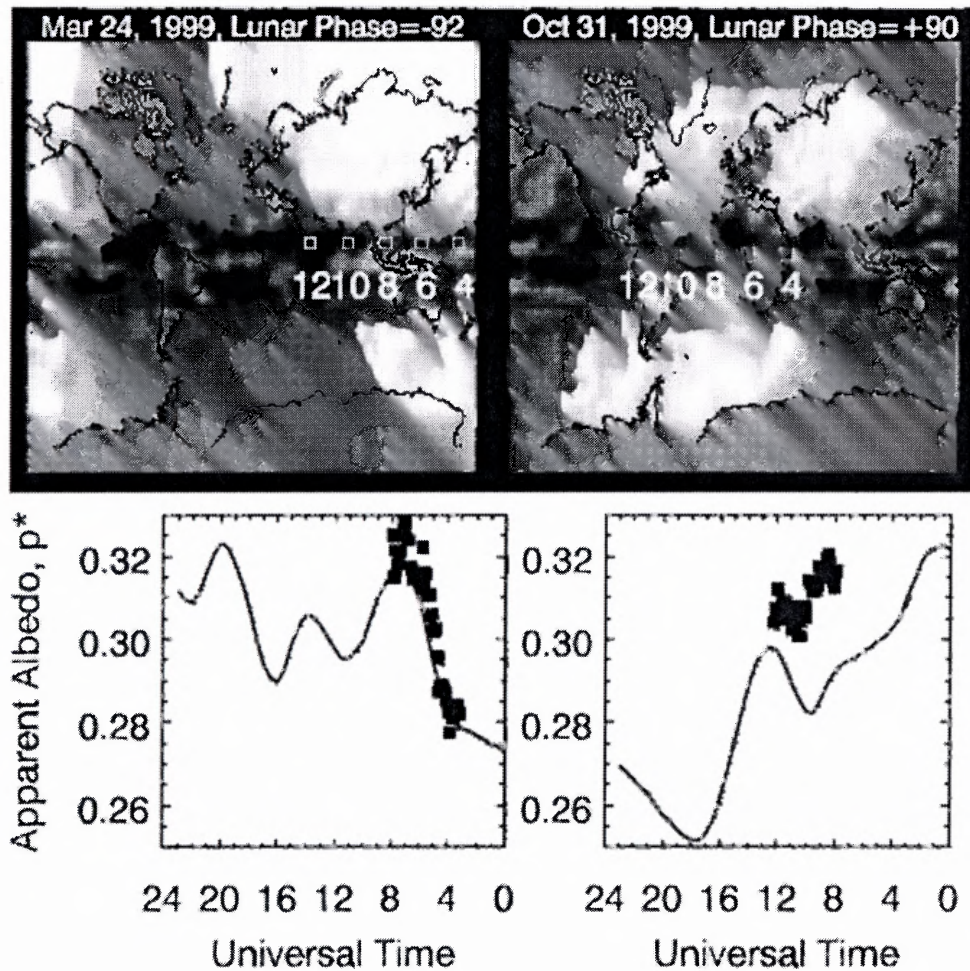
Figure 9.1 In the top panels, the extended bright areas highlight those parts of the Earth that are the source of the Earthshine. The satellite-derived WSI cloud cover maps are shown in a secondary gray-scale with brighter areas indicating greater cloud cover. For October 31, 1999, note that the northernmost regions are not sunlit, and the southernmost regions do not contribute to Earthshine because the Moon is fairly far north in the sky. The empty white boxes in the top panels indicate the longitudes of maximal contribution to the Earthshine at the Universal Time (UT) shown. The solid boxes in the lower panels show the observed apparent albedo as a function of time (note that the time axis is reversed), while the solid line indicates the simulated p^* values for the night.

The ES observations are consistent with the simulations for March 24, 1999, which is one of the nights for which the agreement is quite good. On October 31, 1999, a more typical night, there is a discrepancy of about 5% relative (or 0.015 absolute) in the

apparent albedo. One may notice offsets between the simulations and observations in the lower panels, but must bear in mind that the cloud cover data are a composite of many observations that are taken over about six hours (and sometimes up to 24). Thus, a precise timing between the observations and simulations is not possible. It is simply assumed that the cloud cover is invariant from one posting to the next and no effort is made to smooth the transition. If there were a rapid cloud formation or movement, it could result in observational and simulated results which do not have the same form. However, this does not account for the apparent offset in the albedo.

At high geographical latitudes above 45°, the cloud cover is fairly steady. Thus, the short timescale variations in reflectance in Figure 9.1 are due primarily to irregularities in the fractional cloud cover at low latitudes, and secondarily to the scene type. In the lower left panel of Figure 9.1, one sees that the observed and calculated maxima in p^* at 7:00 UT are due to a relative cloud excess over the Far East, while the calculated local minimum in p^* at 11:00 UT arises from the cloudless area above India and the Arabian Sea. In the lower left panel, there is a more than a 10% change in p^* over about two hours. This sharp increase is due to the increasing contribution of a cloudy Asia to the Earth's reflectance as the Earth rotates. An offset between the observed and calculated apparent albedos is evident in the lower right panel. Typically, the observed results vary more about the mean than do the simulated ones.

CHAPTER 10

SEASONAL CHANGES IN APPARENT ALBEDO, P^*

There are nearly 400 nights of observations covering the period from December 1998 to January 2003. For each of these nights, a mean apparent albedo, p^*, was measured. Here observations and simulations were used to probe the Earth's albedo by determining its seasonal variability (or anomalies). The seasonal variation of the Earth's reflectance is not well known. In fact, Goode et al. (2001) have shown that over a year and a half (1999.0-2000.5), the Earth's seasonal variation is more than 10%. This surprisingly large value was twice that determined from the simulations covering the same nights and the same parts of the Earth.

To determine seasonal anomalies, a fit to the lunar phase dependence of p^* is calculated for all the available data. Then, for each night the difference between the p^* for that night (and lunar phase) and the mean value given by the fit to all nights is determined; this constitutes the anomaly for that night.

Starting with Equations (2.6 & 2.14), the fractional seasonal variation depends only on the observed intensities corrected for airmass. That is;

$$\sum_{i=1}^{N} \frac{p^*_{\text{seas}}(\theta_i) - \overline{p^*}(\theta_i)}{\overline{p^*}(\theta_i)} = \sum_{i=1}^{N} \frac{(\frac{I_a/T_a}{I_b/T_b} \frac{R^2_{em} R^2_{es}}{R^2_{ms}})_{\text{seas},i} - \overline{(\frac{I_a/T_a}{I_b/T_b} \frac{R^2_{em} R^2_{es}}{R^2_{ms}})_i}}{(\frac{I_a/T_a}{I_b/T_b} \frac{R^2_{em} R^2_{es}}{R^2_{ms}})_i} \tag{10.1}$$

where N is the number of nights for which there data in a particular season, θ_i is the lunar phase on the ith night of that season, and $\overline{p^*}(\theta_i)$ is the fit shown in Figure 12.2. The average for a particular season is computed from each night's data by determining the fractional change for that night's phase angle with respect to the mean for that phase angle for all nights, irrespective of season. With this formulation, possible systematic errors associated with the Moon's geometric albedo have been largely eliminated. In the formulation of Equation (10.1), the dependence on lunar phase is minimized by removing effects, in the mean, arising from the fact that p^* is a strong function of lunar phase.

In the next step, the data are averaged in time in bins containing 11 nights each to get a mean anomaly for each period. With this method, one cannot derive an absolute measurement of the Bond albedo, but rather obtain a measurement of its variability.

These seasonal anomalies, which are formulated as fractional changes in p^*, carry information about variations in weather, climate and surface type. The fractional seasonal variation of the Earth's reflectance over almost four years (1999-2002), as determined from the Earthshine observations, is shown in Figure 10.1, together with the simulations from WSI and ISCCP data. An increasing trend in the albedo of about 1% per year is apparent and significant during the full period of measurements.
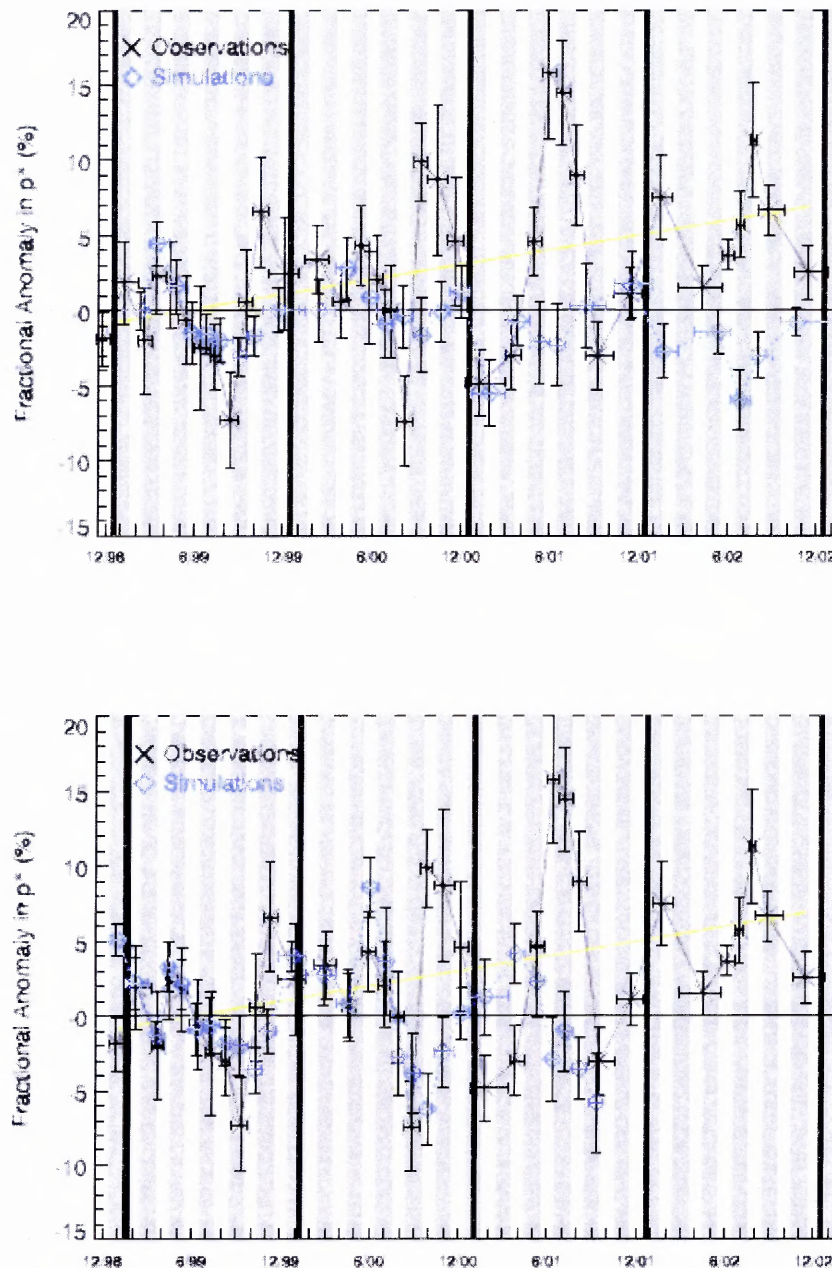
Figure 10.1 Shows seasonal anomalies in the apparent albedo p* from December 1998 through January 2003. From January 1999 onward, there are 308 nights for which there are both observations and contemporaneous WSI satellite and ISCCP cloud cover data, which have been averaged in bins with 11 nights in each. The x's show the mean of the observations, and the vertical bars are the standard deviation of the mean. The size of the standard deviation is from the large night-to-night variations in the cloud cover. The horizontal bars indicate the time span of each average. The diamonds indicate the corresponding simulated results. Anomalies are with respect to the mean for 1999. Top: Observations compared to WSI models. Bottom: Same but for the ISCCP simulations. The straight line in both panels represents a linear fit to the observational anomalies.

One can see in Figure 10.1 a clear seasonal trend for 1999 and 2000, with the Earth being brightest in the spring in the northern hemisphere and fall generally, when it is also the cloudiest (according to WSI satellite data). The seasonal trends can be seen in spite of the fact that the variations within each bin are a significant fraction of the seasonal trends. It must be emphasized that the large vertical error bars in Figure 10.1 arise from the large variations in the cloud cover, rather than from any errors in the data. In fact, the variations within each bin are large compared to the formal error bars for one night. With all of this considered, there is about 15-20% variation in p^* from season to season. However 2001 and 2002 do not show the same seasonal pattern. In the early months of the year, they show a dip in the albedo that is also visible in the simulations (WSI), and it has a maximum in summer time, although this is only reflected by monthly mean ISCCP data (see Figure 10.2).

Note that the agreement between measured and modeled anomalies is remarkable from the beginning of the measurements until the end of 2000, particularly for the ISCCP simulations, for which all nights coinciding with observations have data available. However, since the end of 2000, although the simulations maintain the same seasonal cycle, the observations start to deviate.

The observations show about twice the variability as the simulations, with the differences being greatest at the points with larger departure from the mean. The muted seasonal amplitude of the simulations may well derive from the coarse binning of the scene models and/or the use of simulated snow and ice cover. But the oversimplified

treatment of the clouds is a stronger candidate than any other climate parameter that may contribute to changes in albedo.

In Figure 10.2, the daily modeled 24-hour Bond albedo simulations for the whole Earth are plotted. The bottom panel of the figure reveals a clear offset between albedos obtained using different data sets. The WSI albedo is significantly lower than the ISCCP albedo. The computed averaged ISCCP (1983-2001) albedo $\overline{A}$, is 0.313 and the WSI (1999-2002) averaged albedo $\overline{A}$ is 0.300. This difference is well within what can be measured. However, ISCCP data for 1999 and 2000 are the lowest of the 1983-2001 period in cloudiness and albedo, $\overline{A}$ = 0.307, and so the offset between the two datasets in the common years is reduced by half (0.007). This offset changes with time (Figure 10.2), even disappearing for short periods. T this point it is useful to remind the reader that the WSI data posted on the Internet is uncalibrated from one day to the next, while the ISCCP data undergoes a detailed calibration process.

It is also seen in Figure 10.2 how the seasonal variation of the two cloud (or deduced albedos) datasets are not equivalent. The WSI simulations show the expected seasonal variation with an August minimum and November and May maxima (Danjon, 1928; Dubois, 1942; Dubois, 1947, Gibson et al. 1990). The ISCCP data has a broader peak during the summer months, which generally increases the albedo for the year. The dominant source of the seasonal variability is the interplay of the annual cycle of cloud cover and snow/ice cover; the land surfaces play only a small role. The seasonal cycle of the modeled 24-hour Bond albedo of the Earth and that of the modeled apparent albedo at the time of observations are closely similar, although the geographical areas contributing

to the latter vary slightly along the year due to changes in the inclination of the Earth's and Moon's orbit.
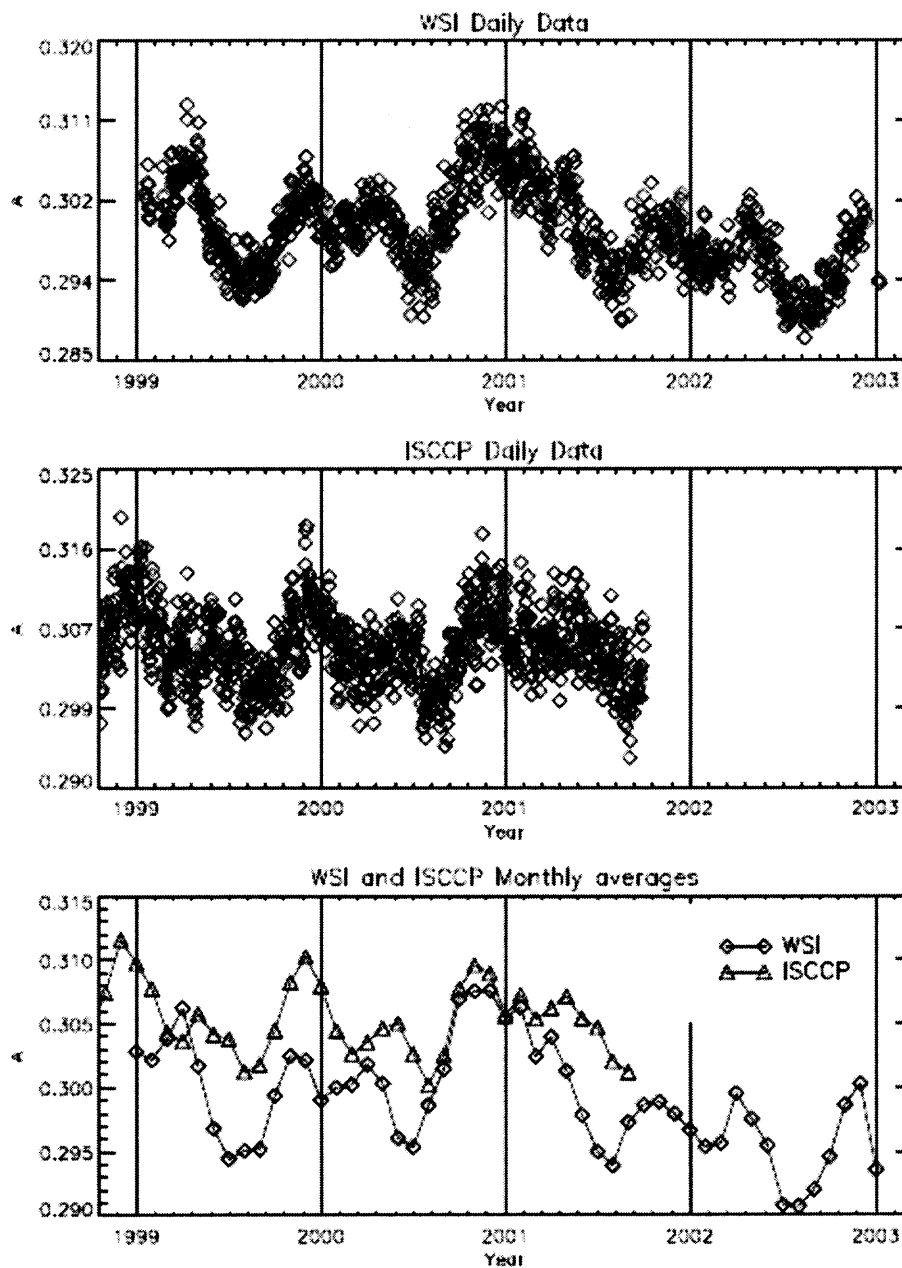

Figure 10.2 Top Panel: Daily mean Bond albedo over the entire Earth, simulated using daily WSI cloud data maps. Middle panel: Same as top but, this time using daily mean ISCCP cloud cover maps as input to the models. Bottom Panel: The daily means in the two upper panels are averaged to monthly values of the Earth's albedo for the whole Earth (24-hour).

In Figure 10.3 is repeated the 24-hour whole Earth simulations of the Earth's Bond albedo, but this time, rather than averaging daily means into monthly means, the model inputs monthly mean cloud cover maps given by the ISCCP D2 dataset. The observed seasonal anomalies have been also plotted in Figure 10.3. Note that the ISCCP-derived Bond albedos from Figure 10.2 and Figure 10.3 are different, particularly in 2001. It is also striking that during 2001 the p^* observations do not agree with the simulations, but agree with the Bond albedo derived in Figure 10.3.

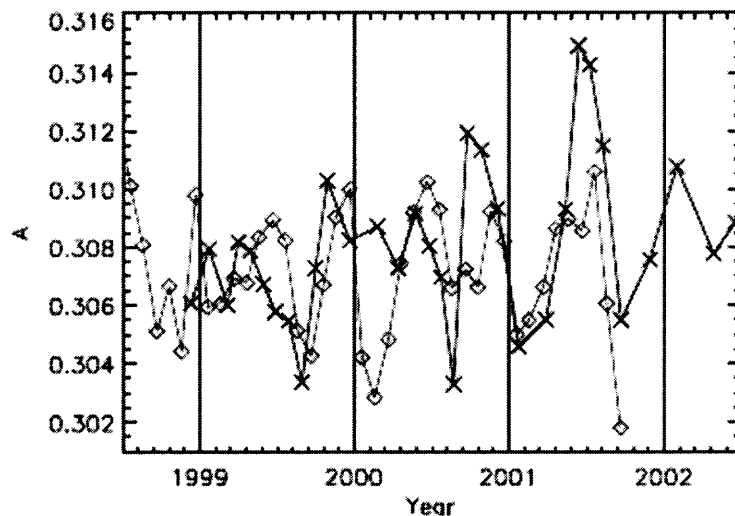**Figure 10.3** Bond albedo simulations of the whole Earth. In this case the monthly mean ISCCP cloud cover maps are used as input to the monthly simulation, as opposed to Figure 10.2 where daily values were used which were then averaged to form a monthly value. The observed seasonal anomalies are over plotted (crosses), and arbitrarily scaled for comparison. Note the good agreement on both curves for the year 2001.

CHAPTER 11

THE EARTH'S BOND ALBEDO

11.1 Determining the Bond Albedo

To determine the Bond albedo, A, from the Earthshine observations one needs to integrate the apparent albedo, $p^*(\theta)$, over all phases of the Moon (as covered in Chapter 2);

$$A = \frac{2}{3} \int_{-\pi}^{\pi} d\theta\, p^*(\theta) f_L(\theta) \sin\theta$$

(11.1)

where θ is the lunar phase angle, $f_L(\theta)\sin\theta$, is the Moon's Lambert phase function and p^* is the apparent albedo associated with a particular night.

The kernel of the integrand, $f_L(\theta)\sin\theta$, is plotted in Figure 11.1. The figure illustrates one of the two basic problems in using the Earthshine to determine the Earth's Bond albedo. The first, and more significant problem, is that one cannot measure the Earthshine for all phases of the Moon. However, it is clear from Figure 11.1 that this becomes a problem for determining A predominately for lunar phases near the new Moon. Further, it can be seen in Figure 11.1 that the integrand in Equation (11.1) peaks near the quarter Moon ($|\theta| \sim 130°$), when the Moon shows a relatively sizable Earthshine, while its phase is not so large that the Earthshine is visible only briefly near sunset or sunrise. More precisely, to evaluate Equation (11.1) to an accuracy of 0.002 requires data for $|\theta| \geq 30°$. Thus, Earthshine observations for most lunar phases are needed for an

absolute value of the albedo, while observations near the full Moon are most sensitive to variations in the albedo because so little of the Earth is visible. The second basic problem in using the Earthshine to determine the albedo arises because the orbit of the Moon traces out an ellipse around the Earth, so one cannot measure the Earthshine in all directions. Therefore, the observations are insensitive to any azimuthal anisotropy that might be present in the Earth's reflectance. Later in this Chapter, simulations are used to show that the effect of the anisotropy might not be significant, but it is systematic and one can account for it. This is done by taking advantage of full spatial coverage provided by the simulations.
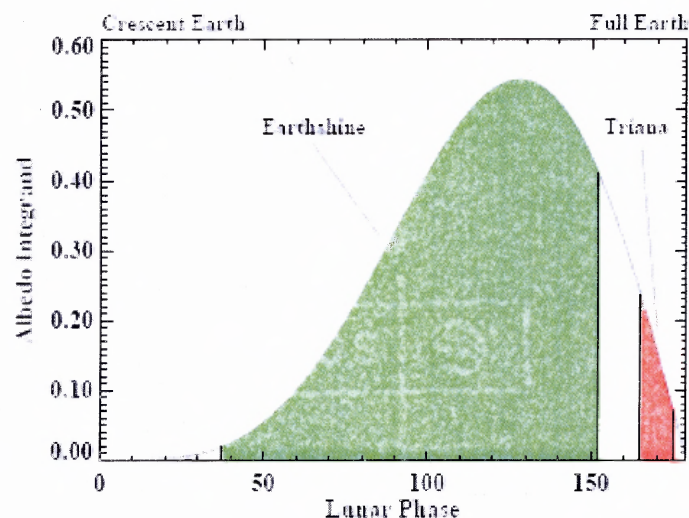
Figure 11.1 The kernel ($f_L(\theta)\sin\theta$) from which the Bond albedo is determined (see Equation (11.1) is shown as a function of lunar phase. Its behavior is dominated by the Lambert phase function for small phase angles, and by $\sin\theta$ for large phase angles. In green, is shown the contribution to the Bond albedo that arises from the range of lunar phases over which one measures the Earthshine. In red, is shown the approximate contribution from a satellite orbiting about L1, assuming the proposed orbit of Triana. If the orbit were to make larger loops around L1, as proposed by Lockwood (2002), all phase angles above 140° could be covered.

11.2 Determining A from p^*

The ES group uses a two-step approach in determining the Bond albedo from the Earthshine apparent albedos. The first step is utilizing the simulations. Simulations for the three years of data for all nights that have concurrent cloud cover are shown in both panels of Figure 11.2 (including all phase angles). The left and right panels show the same data. The left panel shows a least-squares fit in which the apparent albedo is determined for 180 bins of 1° apiece. The least-squares fit is made using;

$$\chi^2 = \frac{1}{(N - N_f)} \sum_{j=1}^{N} \left(\frac{\Delta p_j^*}{\sigma_j} \right)^2$$

(11.2)

where N and N_f are the number of nights simulated and the number of degrees of freedom in the solution, and where Δp^* and σ_j are the deviation of P_j^* from the fit and the error in the determination of P_j^*, respectively.
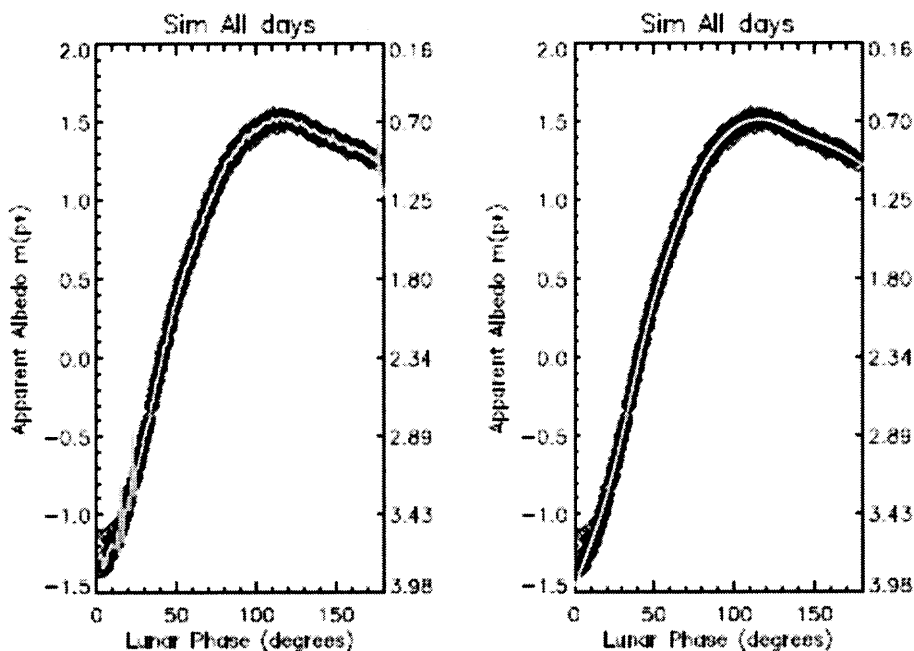
Figure 11.2 Each simulated, single night whole Earth apparent albedo is represented by an empty box. Since there are 898 nights, individual boxes cannot be resolved. The nights span the period from December 1998 to March 2002, and are the nights for which there is cloud cover data. Left panel: A least-squares fit to the data is shown, with the apparent albedo being determined in individual bins that are 1° wide. Note the oscillations at short angular scale for all phase angles. Right panel: The regularized fit to the same data. On the right hand y-axis, the units are of p*.

There are oscillations at short angular scale in p^*, which are largest at the extreme phase angles. The extreme phase angles do not contribute to the Bond albedo, which is 0.2939±0.0001 for the least-squares fit. The oscillations are an unpleasant artifact of the least-squares method. One could, instead, perform a least-squares fit with a low degree polynomial, which would suppress the oscillations. However, the meaning of the stiffening would be unclear. The ES group believes that the apparent albedo should be a smoothly varying function, and has imposed this in a mathematically meaningful way -- regularization (Goode, 1995) -- in which the following is minimized;

$$\chi^2(1 - \frac{N}{N_f}) + \lambda \int_{-\pi}^{\pi} [\theta^2 \frac{d^2}{d\theta^2}(\frac{\Delta p_j^*}{p^*})]^2 d\theta$$

(11.3)

where Δp_j^* is the difference between the jth data point and the fit to the data (the quantity being determined) in the right panel of Figure 11.2. While λ is the regularization parameter which is, in reality, a smoothing constraint. In principle, the parameter is adjusted until χ^2 per degree of freedom is unity, so that the errors in the data are converted to comparable errors in the fit. However, the χ^2 space is relatively flat, so one typically weakens λ until oscillations at short angular scale almost begin to appear in the fitted p^* function. Other forms of the constraint are certainly possible, but a second derivative constraint seems to work best here. In applying the regularization to the right panel, one has the advantage of being able to directly compare the obtained value of 0.2937±0.0003 to that obtained by simple least-squares (0.2939±0.0001). The two results are consistent, and known with about an order of magnitude greater precision than for the observations. The error in the Bond albedo from regularization is about three times greater than that from the least-squares determination. This is due to the non-physical variation introduced by the short angular scales variation. Still, the regularization introduces a point-to-point correlation in the errors, but it shall be seen that this effect is small, and the errors very nearly take the standard meanings.

Note that in Figure 11.2 the observations are for all lunar phase angles, averaged over the whole day, which give a large number of points and a small spread of the modeled values, as the models are overly smooth. Hence, the determination of the albedos with such small errors from the integration. Those errors do not correspond to

the measurement precision for the albedo from observations. The measurement errors are about an order of magnitude larger.

Next, regularization was applied to the subset of nights shown in the left panel of Figure 11.3, and using essentially the same regularization parameter as in Figure 11.2, and after assuming the left panel and right panel have the same values at phase angles of 0 and 180°. The left panel is the subset of 24-hour simulations for which observational data have been taken on the same calendar day. The resulting fit is shown in both the left and right panels of Figure 11.3. It can be seen that the fit to the subset of the data fits the whole of the data quite well, especially for the range of phase angles that is so important in determining the Bond albedo. With this fit, one finds a Bond albedo of 0.298 ± 0.001, which is regarded as being consistent with the pure least-squares and regularization results of Figure 11.2, after recognizing the fact that 2/3 of the nights in the right panel of Figure 11.3 are absent in the left panel. The fit is fairly insensitive to the choice of λ over nearly an order of magnitude.
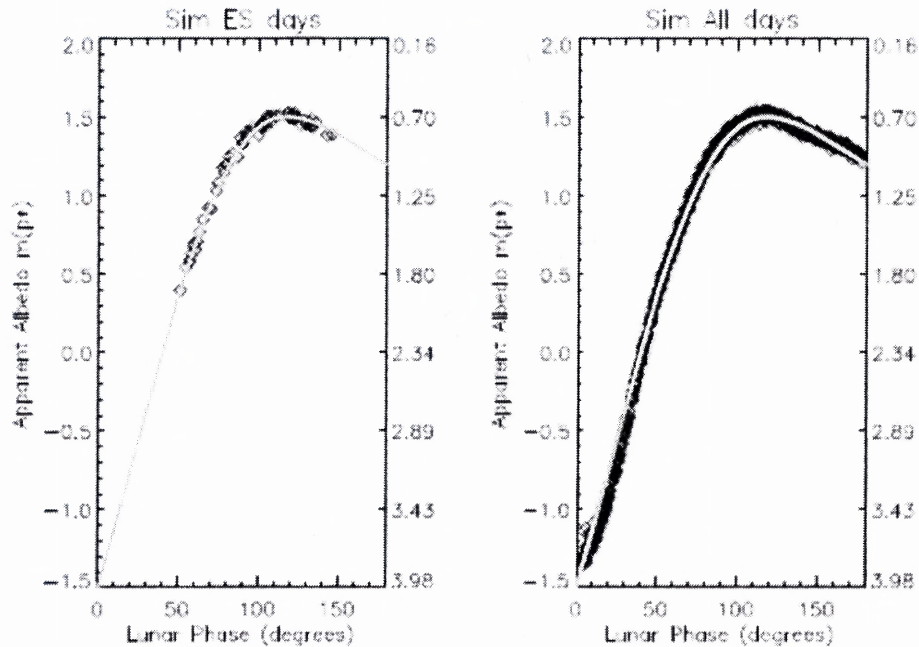
Figure 11.3 Each box represents a whole Earth (i.e., covering a twenty-four hour period) simulated albedo. Left panel: Whole Earth simulations for which the twenty-four hour period includes nights for which there is Earthshine data and cloud cover (268 nights). The 268 nights span the period from December 1998 to March 2002. Right panel: Whole Earth simulations for all twenty-four hour periods, during the same period, for which there is cloud cover data (898 nights -- 466 during the waxing Moon and 432 during the waning phase). The yellow curve in both panels is derived from the constrained or regularized least-squares fit to the left panel. On the right hand y-axis are used units of p^*.

The second step in determining the Bond albedo for the observations is a further effort to account for the fact that the observational data do not span all phase angles. For this, one next examines p^* simulations for the daytime region of the Earth visible from the Moon, for phase angles between 60 and 120° -- the regime for which there is the most confidence in the data. In Figure 11.4, a scatter plot is shown of the Bond albedo for a twelve month running mean vs. the contribution to that integral coming from phase angles between 60 and 120°. To construct the 12-month running mean, one starts from the period December 1998 to November 1999 and then removes the first month and add a

new one until the period April 2001-March 2002. The correlation between the total and "partial" integration values is 0.98. To test this method it was repeated using the interval 90-120°, a correlation was seen between total and "partial" integration of 0.99. The linear fit shows a way of converting a partial integral to a total integral. The albedos obtained by converting the partial integrals and from the total integrals are practically indistinguishable. After experimentation, it was found that this approach returned more reliable values for the albedo than a simple regularization fit as used in the left panel of Figure 11.3 and in Goode et al. (2001).
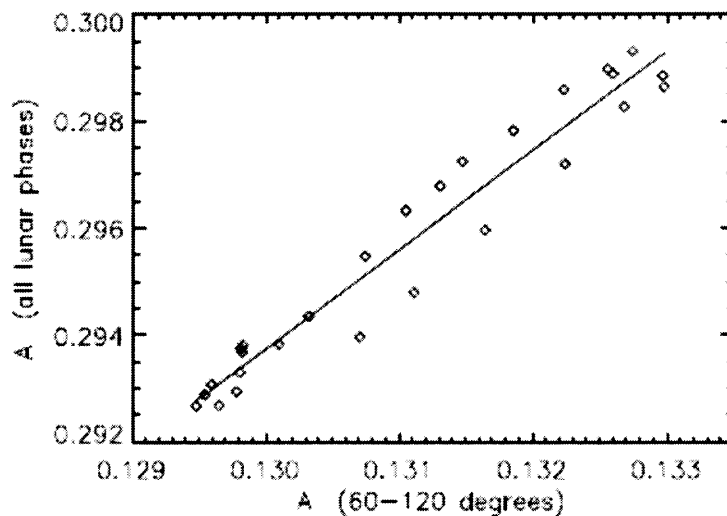
Figure 11.4 Scatter plot of the mean bond albedo for whole Earth simulations, integrated over all lunar phases angles, and the integration value over lunar phase angles from 60° to 120° only. Each point is a 12-month mean, starting with the period December 1998-November 1999 for the first point, January-December 1999 for the second, and so on until April 2001-March 2002 for the last point. The correlation coefficient between these two integrations is 0.98.

One uses this linear relation to determine a Bond albedo from the observational data. Again, using the daytime Earth's region visible from the Moon simulation points at

0 and 180° to fix the regularization, and then determine the Bond albedo by scaling the fit between 60 and 120° by the same linear factor as used in determining the Bond albedo for the simulations at all available lunar phases. Applying the same regularization to the observational data, which contains as a subset the 268 nights in the left panel of Figure 11.3, over a 3+ year period it was found that the mean Bond albedo for the Earth was 0.295±0.002 (0.293±0.003 for the evening observations and 0.296±0.002 for the morning). The deviations will contain not only the noise, but also any seasonal and long-term albedo variability that might have occurred during this period. The fit is shown in the left panel of Figure 11.5. The right panel shows the corresponding fit for the simulations covering the same times and parts of the Earth that contribute to the Earthshine, for which an albedo of 0.298±0.001 was calculated. The larger deviations in the observational results are indicative of the greater spread of the observational points about the mean (compare the left and right panels of Figure 11.5).
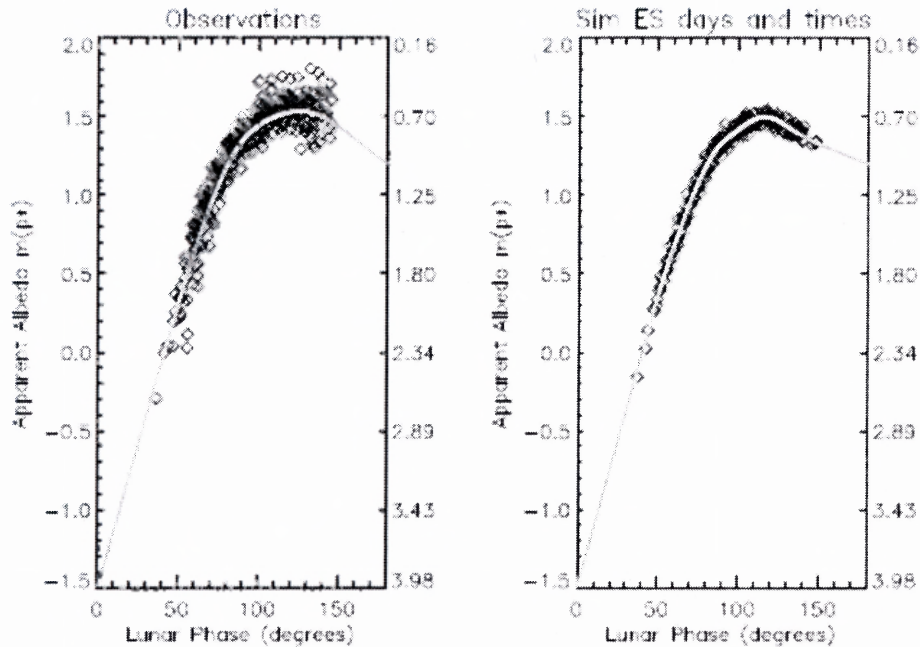
Figure 11.5 Observed (left panel) m(p*)'s(defined as = -2.5log p*) plotted against the absolute value of the lunar phase from 225 clear observing nights from December 1998 through March 2002. Simulations (right panel) are shown covering the time intervals and parts of the Earth that contribute to the Earthshine signal for the 268 nights for which there were observations and contemporaneous cloud cover data. Each data point represents a nightly average of a series of 0.5-3.0 minute Earthshine measurements taken once every five minutes with 0.1-5.0 second Moonshine observations interspersed. Error bars for each night would be within the symbols. For the 268 nights for which there are observations and simulations, constrained least-square fits to the data and simulations are shown by the yellow curves. On the right y-axis, are units of p*.

11.3 Effect of Anisotropy

As mentioned at the beginning of this Chapter, one concern about measuring the Earthshine to precisely determine the Earth's albedo is the amount of anisotropy in the Earth's scattering. At any instant, the Moon subtends 0°.5 as seen from the Earth, and the obliquity of the Moon's orbit extends this coverage over the lunar month to only 6° on either side of the ecliptic. Therefore the Earthshine is not sensitive to light scattered out of the ecliptic. One can directly test the sensitivity by comparing the result of simulating

the Bond albedo for the whole Earth to that using the simulated Earthshine. For the case of the Earth that is in the sunshine, Equation (8.1) was used to calculate an average for the more than three years of data, A=0.3001±0.0002. For the whole of the Earth in the Earthshine, one is effectively assuming that for all lunar phases the Earthshine does not depend on the azimuthal scattering angle. Testing Equation (11.1) by using $p^*(\theta)$ from the least-squares fit in the left panel of Figure 11.2, from which was determined an equivalent 3+ year average Bond albedo of 0.2939±0.0001. This discrepancy arises because the relatively brighter polar regions are sometimes in the sunshine, but not in the Earthshine. For this reason the Bond albedo values obtained from the Earthshine observations and the A* simulations should be increased by 0.006. This effect is illustrated in the right panel of Figure 9.1 for which the Moon is northerly in the sky and doesn't receive light from the sunlit southernmost regions of the Earth.

However, it could be that the models are not accurate enough to detect any anisotropy bias. Thus, the possibility of an anisotropy bias in the Earthshine measurements remains and needs to be explored in future work.

CHAPTER 12

THE BOND ALBEDO DURING 1999-2002

Figure 12.1 illustrates the change in $m(p^*)$, (defined as $= -2.5\log p^*$) vs. absolute value of the lunar phase angle as determined from the nightly Earthshine observations -- with the morning and evening observations presented separately, and combined. In the plots, each data point represents a nightly averaged p^* value, with which the group studied the changes in p^* for different nights, months and seasons. One may first note that while p^* is relatively flat near the quarter Moon, the flatness implies a near Lambertian Earth for most lunar phase angles (see Equation (2.6)). However, with the Moon approaching full phase and θ getting close to 180°, the Earth as seen from the Moon, becomes a thin crescent, and so Earth-reflected radiation reaching the Moon is more dominated by forward scattering in the atmosphere. For lunar phase angles much below about 40°, the group presently regards the results as unreliable because of the proximity of the Earthshine fiducial patches and the terminator (the transition from the Moonshine to the Earthshine is not sharp). Further, there is no reliable Earthshine data near the new Moon (much beyond a lunar phase angle of about 140°) because the Earthshine is visible for only a brief time near sunset or sunrise, depending on whether the Moon is in its waxing or waning phase. Thus, the Earthshine observations at lunar phase larger than 140° are made at large airmass and the extrapolation to zero airmass is unreliable. For large lunar phase angles, it is also difficult to find a fiducial patch that is confined inside the thin lunar crescent.
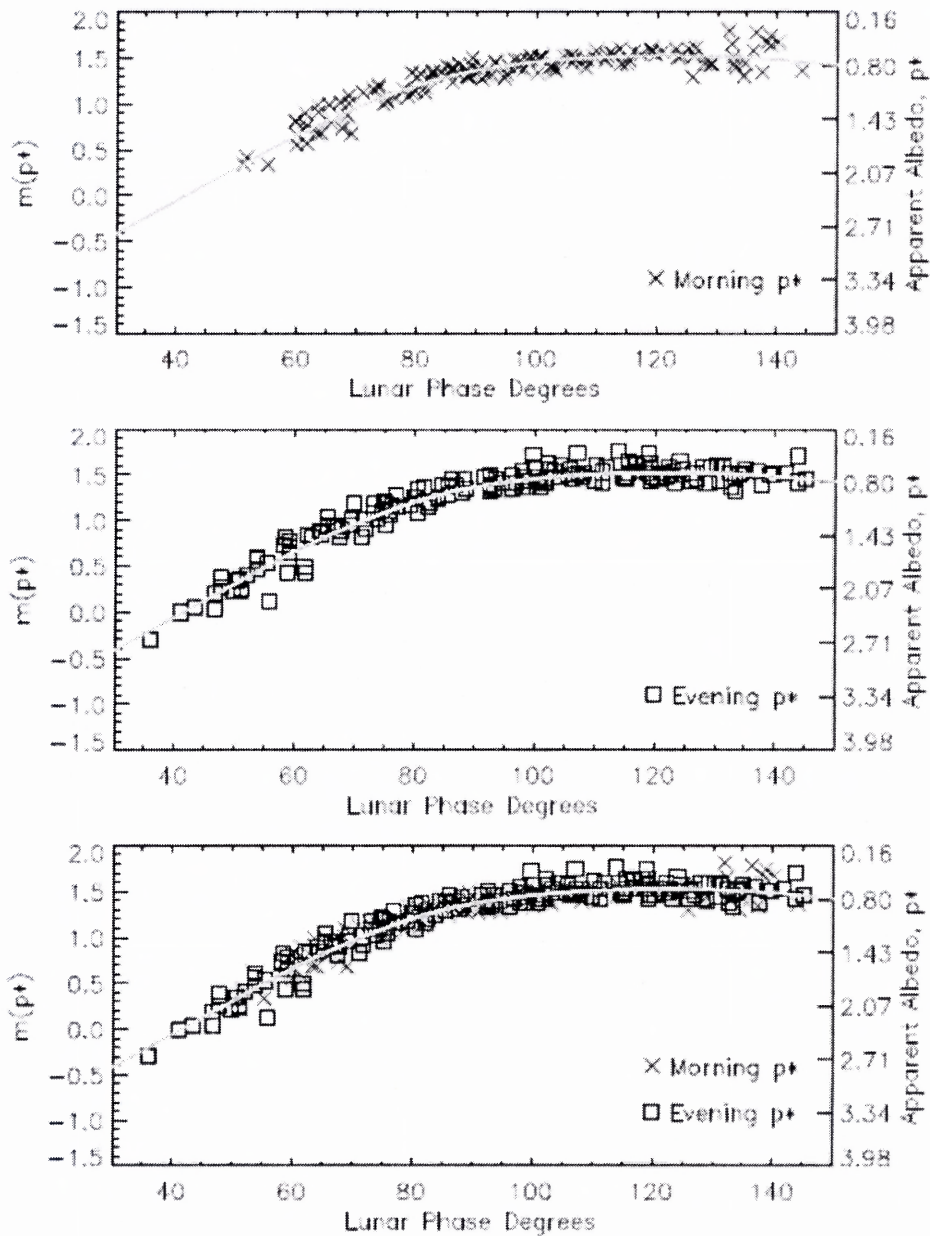
Figure12.1 Plot of the mean m(p*), which is determined from 25 sets for each night, for (top) morning and (middle) evening observations. The bottom panel gives the combined results for mornings and evenings. In the figure, 340 nights of observations are included (150 nights of morning observations and 190 evening). The solid line in all panels indicates the curve from the fit to the data in the bottom panel. The right y-axis is in units of p*.

A detailed examination of Figure 12.1 reveals that, with respect to the fitted mean,

the *p** determined from the local Big Bear Solar Observatory (BBSO) morning

observations (lunar phase angle > 0) are not apparently distinct from those determined from the local evening observations (lunar phase angle < 0); i.e., the Earthshine data from BBSO nights implies that the contemporaneous sunlit parts of the Earth are equally shiny in the evening and in the morning (note that evening and morning refer to local time at BBSO). Ultimately, from the Earthshine data it was determined that a mean albedo of 0.293±0.003 was found for the evenings and a mean albedo of 0.296±0.002 for the mornings. The lack of a significant difference may seem somewhat surprising because the Earthshine observed in the mornings and in the evenings comes from the reflection of sunlight from different parts of the Earth. In the evening observations, the Earthshine is dominated by Southeast Asia. In the mornings, the Earthshine is dominated by Africa, Europe and the Atlantic.

One might think that the agreement between evening and morning determinations results from fortuitous compensations from the afternoon/evening development of deep convection versus morning maxima of low stratified clouds. But most likely, the agreement is due to the large area-average in the Earthshine Bond albedo integrations, which contains a wide mix of different land, ocean, ice and cloudy areas.

Bearing in mind that a change in $m(p^*)$ of $0^m.01$ corresponds to about a 1% change in p^*, observations show a (roughly) ±5% variation within a season in the apparent albedo, p^*, even near the quarter Moon where the data is most reliable. This variation is primarily associated with changes in the cloud cover and/or changes in the lunar phase, rather than some error in the data collection/reduction process. In Figure 12.1, the spread about the mean is even larger. This is primarily associated with seasonal and long-term variations in the reflectance (Figures 10.1 and 10.2).

To better understand the influence of the Earth's varying topography and cloud cover on p^*, the albedo is plotted as observed throughout single nights in Figure 12.2. This plot comes from using Equation (2.14) after each point is corrected for airmass, and inputting the proper lunar phase for each observed time point. Note that the lunar phase function changes by about 0.5° per hour. In Figure 12.1, each point represents the mean of a single night. In each panel of Figure 12.2, the mean for the night is given as a number. In Figure 12.2a and Figure 12.2b, observations of two nights with almost the same lunar phase, but from different months, are compared. They demonstrate a common tendency of an early decrease in $m(p^*)$, or a brightening Earth, as the sun is rising over Asia, increasing the contribution from the relatively bright Asia. Although this trend a brightening Earth is more apparent in Figure 12.2a. The sun rising over a cloudy Asia causes a 5-10% change in p^* over the period of the observations. Even though the temporal evolution of the points in Figures 12.2a and 12.2b closely resemble each other, the mean value of p^* in Figure 12.2a is 5% smaller. This difference reflects a greater Asian cloud cover on March 24 than July 20. However the fact that daily and seasonal variation is mixed makes the analysis difficult. Some part of the appreciable difference is probably due to seasonal changes in cloud cover, rather than differences in the part of the world measured. In Figures 12.2c and Figure 12.2d, the observations are from two mornings at similar phases of the Moon, and covering comparable local times. One notices immediately, that the p^* in Figures 12.2c and 12.2d are about 10% smaller that their counterparts in 12.2a. In Figures 12.2c and 12.2d, each panel shows an

increasing $m(p^*)$, or a darker Earth, as time goes on. This is because the sunrise over the Atlantic is increasing the role of the darker, and less cloudy, ocean in the Earthshine.
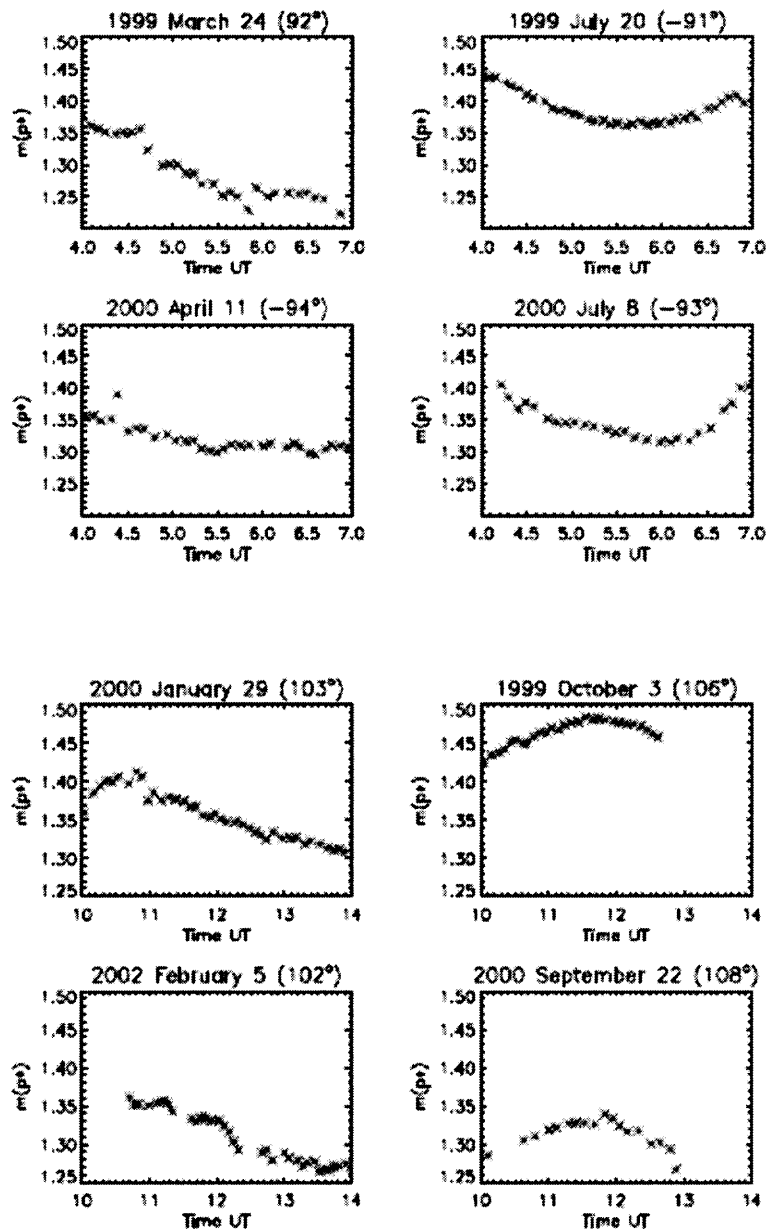
Figure 12.2 Plots of m(P*) observed for several nights of data, against the time of observations (UT). Top four panels (pairs a & b in the text): All nights have almost equal lunar phase angle. Note how the variability along the night is the same in all panels, but the mean value depends on the seasons. Note also that the two top right panels correspond to the same month (July, one year apart) and have almost equal values. Bottom four panels (pairs c & d in the text: The difference in lunar phase angle between the right and left panels is quite small (~5°), but it is enough to make the nightly variation slightly different (or delayed). Again the average albedo value depends on the season.

As shown earlier for one night, if the nights are combined to obtain a yearly average, then the total deviation from all sources of uncertainty will be smaller, but no smaller than that associated with the mean values of the various lunar phase functions and the ratio of the geometrical albedos. For instance, there are 340 nights of data for which the fit to Beer's Law has a standard deviation of less than 1% for the single pair of fiducial patches used by Goode et al. (2001). These are regarded as "good" nights. Calculating the standard deviation of the mean for the 150 (190) morning (evening) pairs, one gets 0.8% (0.7%). Combining this with the uncertainty in the lunar phase, one finds a deviation of less than 1% in the binned p^*'s. Such error bars would be well within the symbols of Figure 12.1. The most likely source of systematic errors is the determination of the geometrical albedos, coming from a single lunar eclipse, but such systematic errors would not change the spread in the points. If the presumed systematic errors were comparable to the measurement errors reasonably identifiable, they are still considerably smaller than the spread in the $m(p^*)$'s that appear in Figure 12.1.

In Figure 10.2, the daily mean global albedos were shown from the simulations of the whole Earth covering 1999.0-2002.3, and calculated using Equation (8.1) and WSI daily cloud maps. Roughly, the figure shows peaks in the Earth's reflectivity in the fall and spring, while showing minima in the winter and summer. From this, a mean Bond albedo of 0.3 was determined over that period. Note that the size of the spread in night-to-night variations is comparable to the amplitude of the seasonal variability.

Applying Equation (8.3), the observed apparent albedo shown in Figure 12.1 is simulated covering the same parts of the Earth at the same time. The results are shown in Figure 12.3. Note that the distribution is tighter to the fit than in Figure 12.1. Thus, the

greater scatter in Figure 12.1 cannot be due to different nights for the same lunar phase seeing different parts of the Earth, because each night's simulation covers exactly the parts of the Earth which are observed. However, like the observational results, there is no clear distinction between the simulations for morning and evening. As in Figure 12.1, it is also clear from the simulations shown in Figure 12.3 that the evening data have a greater scatter about the mean than do the morning data. This implies a more variable cloud cover over Asia. Figure 12.4 shows the same kind of plot as in Figure 12.3, but covering the entire Earth for nights for which there are observations and cloud cover data (see the difference in coverage between the solid lines and solid boxes in Figure 9.1). Since the whole Earth simulations average more of the globe, it is not a surprise that these simulations show considerably less scatter than those of a part of the Earth. Also note that the mean apparent albedo in the simulations, is higher for the whole Earth than it is for the part seen at BBSO by 0.016 ± 0.017 (1.3%) in p^*, i.e. the albedo increases when the third of the Earth invisible to Big Bear is added. That may be a consequence of including the American land mass, although the result is not statistically significant.
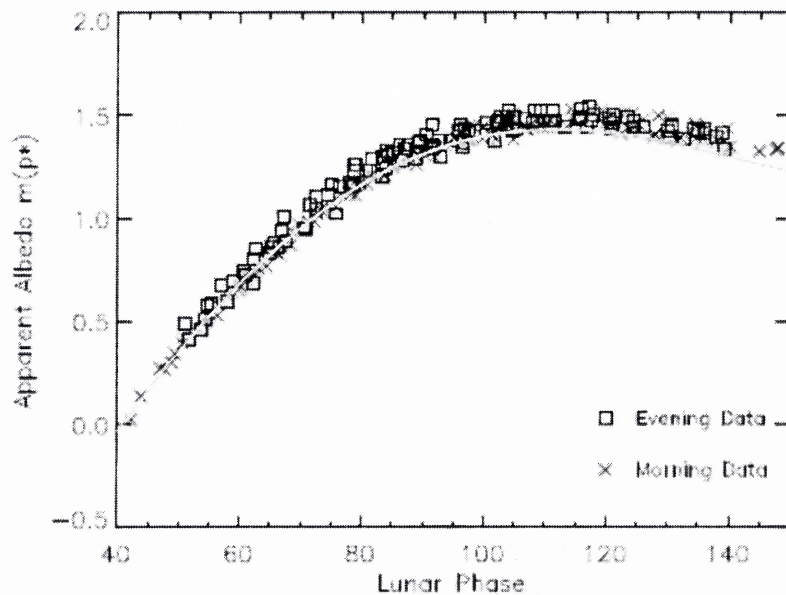
Figure 12.3 Plot of m(p*) vs. absolute value of the lunar phase from simulations covering the same phases of the Earth as the observational results in Figure 12.1; i.e., the simulations are looking at the regions of the Earth visible from the Moon at the times of the Earthshine observations. Each data point represents the averaged m(p*) value throughout one night; an "x" indicates morning observation (lunar phase > 0) and a "square" indicates evening observation (lunar phase < 0). For reference, the solid curve shown is fit to the data in Figure 12.1.
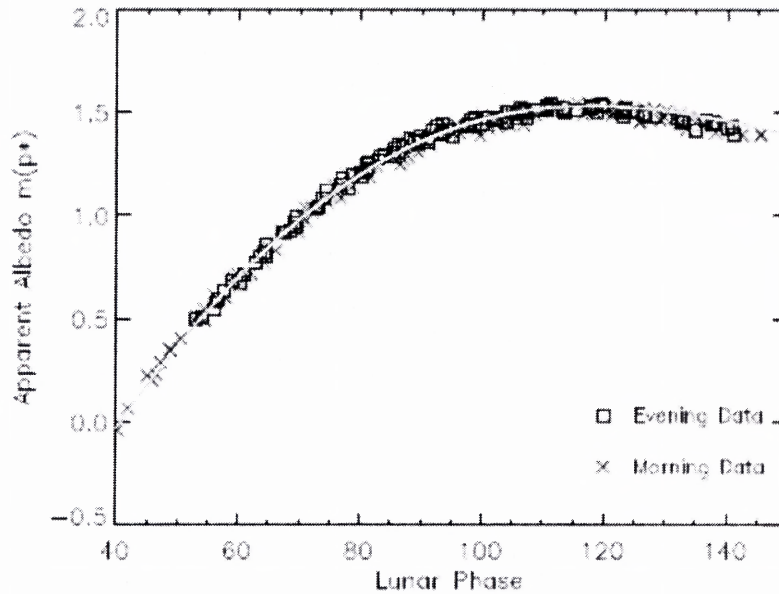
Figure 12.4 Plot of m(p*) vs. absolute value of the lunar phase from simulations covering the whole Earth for all days for which there are observations. Each point represents the 24-hour average of UT defined days for which there is Earthshine data. The "x's and "squares" are given to show whether the 24-hour average is connected to observations at positive or negative lunar phase. For reference, the solid curve is the fit to the data shown in Figure 12.1.

CHAPTER 13

SOME CONCLUSIONS ABOUT THE PHOTOMETRIC OBSERVATIONS AND THE MODELING

From BBSO, the ES group has observed the Earthshine for more than three years. The large scale average of the Earth's albedo has been determined for major areas of the Earth, including Europe, Africa and the Atlantic Ocean in the morning observations, when the sun is high over Africa and the Atlantic Ocean, and the Moon is in its declining phase. The albedos for large areas in Southeast Asia and the Pacific have been measured in the evening observations during the rising phase of the Moon. From the Earthshine data, it is seen that Southeast Asia and West Africa/Southern Europe have very nearly the same albedo.

The albedos determined are as precise as determined from satellites. Thus the Earthshine method provides a different way to measure the Earth's albedo. One of the obvious advantages of Earthshine observations is having an absolute calibration coming from the brightside of the Moon. This is because the ES group makes use of relative photometry as opposed to satellite instrumentation, which normally makes use of absolute measurements more prone to calibration errors.

The BBSO results have been compared with models of the Earth's scenes inputting contemporaneous snow/ice cover from models and cloud cover from satellites. A general agreement is found between the observed and modeled results, with the model results uniformly showing milder amplitude variations. The greater spread of the observations, such as seen in Figure 12.1, does not result from errors in the observations, but rather from seasonal and long-term changes in reflectance that are not captured by the

models. In sum, it can be concluded that the ES group models, using daily mean cloud cover and a simplified model of the cloud radiative properties, are overly smoothed.

With the quoted level of precision, the ES group can track long-time frame changes in the Earth's albedo, if they are at a climatologically significant level. Both from the observations and simulations it has been found that there are strong seasonal variations and an annual increasing trend during the 1999-2002 period.

CHAPTER 14

OBSERVATIONS OF THE EARTH'S VISIBLE SPECTRAL ALBEDO

14.1 Introduction

Ground-based measurements of the Earthshine (ES), which allow one to view the Earth as if it were another planet in the solar system, have become a valuable tool for studying the Earth's global climate. A precise determination of changes in the Earth's total or Bond albedo is essential to understanding Earth's energy balance. While measuring the reflectivity for other planets is a direct task, the indirect observation of Earthshine, after its reflection from the Moon, is the only ground-based technique that allows one to measure the albedo of this planet. As detailed above and in previous publications, long-term photometric observations of the Earthshine have been used to determine variations in the Earth's reflectance from 1998 to 2003 (Goode et al. 2001; Qiu et al. 2003; Palle' et al. 2003; Palle' 2004b), and by comparison with International Satellite Cloud Climatology Project (ISCCP) data sets, the ES group reconstructed the Earth's global reflectance variations over the past two decades (Palle' et al. 2004a). Those variations in albedo depend on changes in global cloud amount, cloud optical thickness, and surface reflectance of the Earth contributing parts of the Earthshine.

In this Chapter the potential of spectroscopic studies of the Earthshine in climate studies is demonstrated. This is done by quantifying the wavelength dependence of Earth's albedo through a single night of observations. A determination of the longer-term evolution of the spectrum awaits more spectral data. Secondarily, a spectral study enables one to measure the strength of the "red" or "vegetation" edge in the Earthshine. Knowing the strength of this latter signal is critical in evaluating the utility of exploiting

the spectral vegetation edge in the search for Earthlike extrasolar planets. Previous efforts to estimate the globally averaged spectrum of Earth (Arnold et al. 2002; Woolf et al. 2002) have aimed to give a qualitative description of its astrobiological interest.

The albedo on November 19, 2003 was measured over the sunlit part of the Earth, centered for that night over the Atlantic Ocean, by doing spectrophotometry (R = $\lambda/\Delta\lambda$ ~ 1000) of the ES (reflected from the dark side of the Moon) and Moonshine (MS; reflected from the bright side of the Moon) from Palomar Observatory. The appropriate lunar geometry corrections were applied in order to determine a mean spectral dependence comparable to photometric albedos simultaneously taken at Big Bear Solar Observatory. Synthetic simulations of the photometric albedo (Palle´ et al. 2003) were also made, and compared favorably.

14.2 Data Acquisition and Analysis

The observations of the ES and MS spectra for November19, 2003, a clear night over Palomar Observatory, were between 10.47 and 13.08 hr. UT. The Moon was observed with a single-order, long-slit spectrograph, using the Palomar 60" (1.5 m) telescope. The instrument known as the 60" Echelle can be operated in either Echelle or long-slit modes. An entrance slit of 1.32 arcsecond by 6 arcminute on the sky was selected; for comparison, the mean lunar apparent diameter during the time of observations was 32.24 arcminute. This configuration covers the spectral region between 460 and 1040 *nm*. However, this range was limited by the poor CCD quantum efficiency below 500 *nm* and by the fringe interference patterns in the red. The fringing starts to appear at about 800 *nm* (although they were reduced when taking the ratio of ES to MS) and is always

important above 980 *nm*. Thus, the final effective range was limited to between 480 and 980 *nm*.

The slit was east-west oriented and positioned in such a way that about half of it was over the lunar disk near the limb, and the other half was over the adjacent sky (see Figure 14.1). Two lunar patches were selected near the bright and dark lunar limbs in the highland regions of the Moon. These patches were alternatively measured as the air mass varied through the night. During each MS-ES cycle, the Moon was tracked in right ascension and declination at a fixed rate. To account for the Moon's motion relative to the stars, rates were updated every 15 minutes, to minimize the deviation from the original patch. The updates were done after each MS-ES cycle was completed. A total of eight MS-ES cycles were obtained during observations from Moonrise to sunrise.

The basic reduction steps were performed with the Image Reduction and Analysis Facility (IRAF) software system. The alignment between the dispersion direction and the CCD rows was verified, and the necessary geometrical corrections were applied to all images in order to preserve the maximal possible spectral resolution during the extraction of the spectra; laboratory argon lamps were used for this purpose, as well as for wavelength calibration.

The spatial profiles within the region covered by the slit for each MS and ES exposure are shown in Figure 14.1. These profiles are affected by three correctable and/or ignorable types of variations: (1) a large gradient due to the overall Lambert-like illumination of the MS, (2) light scattered from the Moonshine into the ES (which decreases linearly with the distance to the MS limb), and (3) small features due to the varying reflection index over the lunar surface within the region covered by the slit. Eight

apertures of equal size were initially extracted from every image, four over the sky side and four over the lunar side. The background due to the scattered light was corrected by subtracting a linear extrapolation of the sky spectrum to the position of each of the four ES and MS lunar apertures. The extrapolation was done point by point across the spectral direction. Then all spectra were normalized to a unit exposure time.

Because Moonshine and Earthshine exposures were not exactly simultaneous, each MS spectral transmission was interpolated to the air mass of its temporally closer ES spectrum. The ratio ES/MS, $(I_{a,\lambda}/T_{a,\lambda})$ / $(I_{b,\lambda}/T_{b,\lambda})$ in Equation (9.1), could then be calculated to obtain the implied top of the atmosphere ratio.

14.3 Measuring the Lunar Relative Reflectivity

To determine the Earth's reflectance on November 19, 2003 requires two quantities from observations on other nights: the Moon's geometrical albedo (determined from total eclipse data) and the lunar phase function (determined over several years of photometric observations covered in Chapter 4). To apply these to each of the eight pairs of measurements, one requires the accurate selenographic coordinates for the regions where the Earthshine and Moonshine are reflected (Qiu et al. 2003).

For each of the eight MS-ES spectral observing pairs, one must re-point the telescope and in the subsequent analysis make a precise, ex post facto determination of the location of the narrow slit for each observation (rather than always looking at the same fiducial patch, as is done in the photometric observations). A deviation of up to 10 arcsecond in the east-west direction and up to 20 arcsecond in the north-south direction is estimated. This assessment is consistent with changes in the slit position shown in Figure 14.1 (top

panel) where each narrow white line (best viewed just off the limb) represents the location of the spectrograph's slit for each observation. The magnitude of the changes in the lunar profile observed for different exposures is shown in the same figure for lunar phase +1.23° (middle panels) and lunar phase +117° (bottom panels).

Earlier it was argued that the lunar geometrical albedos for the Earthshine and Moonshine differ by only a small spectral offset; equivalently, one can assume here that $p_{b,\lambda}/p_{a,\lambda} = p_b/p_a$. In the data reduction, the relative photometric reflectivity of patches b and a was determined for each of the eight pairs of MS and ES images via an ex post facto approach to precisely eliminate the error introduced by small deviations from the initial selenographic coordinates (fiducial patch) when re-pointing the telescope for each MS-ES observing cycle. To measure each ratio, p_b/p_a, photometric observations of the full Moon were used, interpolating at lunar phase angle 0° during the lunar eclipse on November 29, 1993. This eclipse was observed during 11 hr (before and after totality) from Big Bear Solar Observatory (BBSO) using the 25 cm solar telescope that is now part of BBSO's global Hα network. Between four and five images were taken, approximately every 30 minutes. Sixteen lunar patches of 3 arcminute by 2 arcsecond centered on each ES and MS slit position were selected. The different Earth–Moon distance and lunar polar axis orientation for the eclipse night and for observations on November 29, 1993 was taken into account. The differences in lunar libration were considered by properly modifying the projected size of the observed patches for each eclipse image.
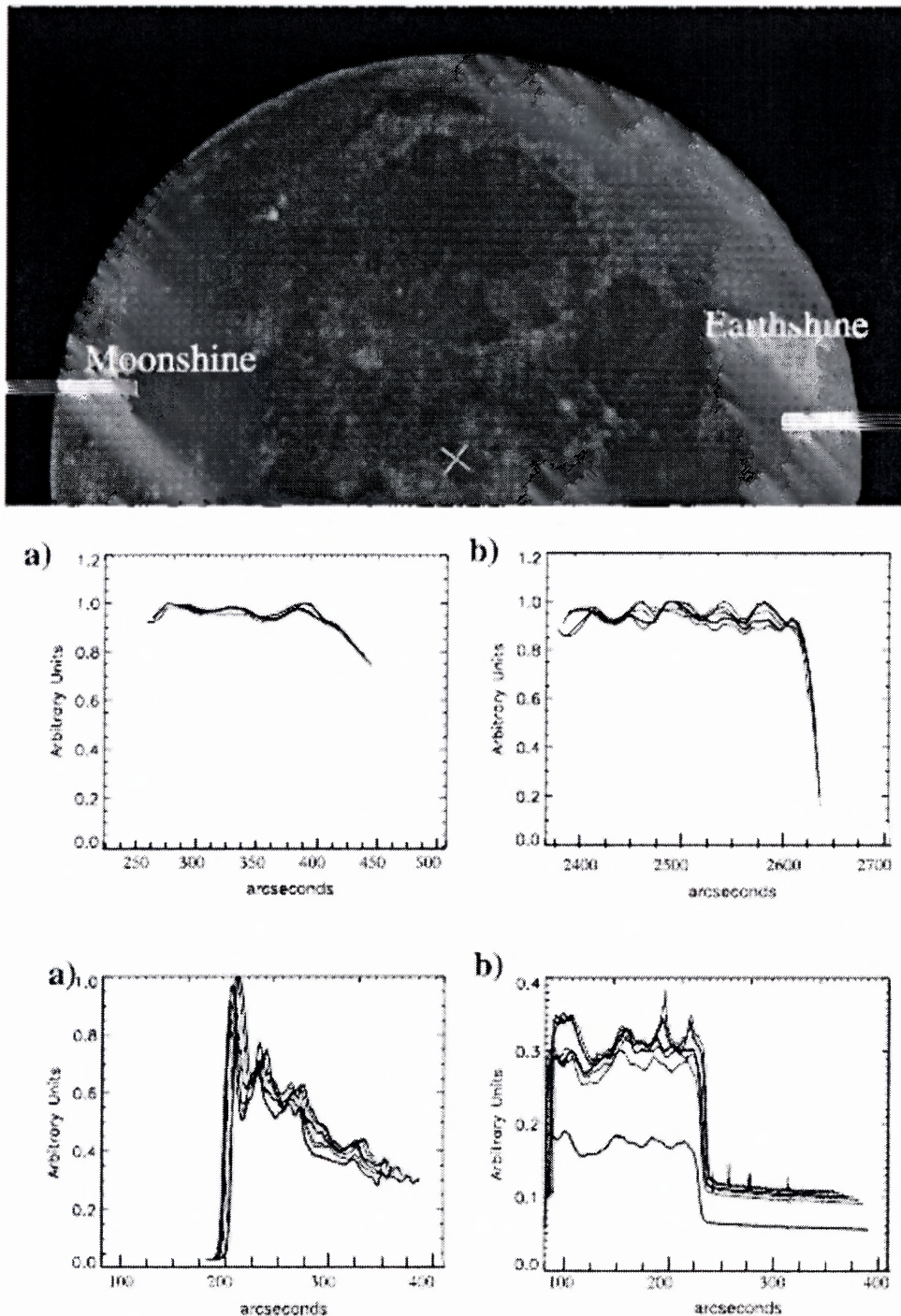
Figure 14.1 Top: image taken during the Nov. 29, 1993 eclipse. The slit positions during observations on Nov. 19, 2003 are shown for each cycle (eight individual fine white lines just off the limb). Middle: (a) MS and (b) ES limb profiles at lunar phase angle +1.23° (during eclipse) for the slit positions on November 19, 2003. Bottom: (a) MS (showing limb brightening) and (b) ES (showing Earthshine flatness on the disk) as actual image profiles along the slit during observations on Nov. 19, 2003.

Intensities were normalized to 1 sec exposure, and the mean reflectivity for each patch was then calculated to obtain a pair of p_b and p_a values for each MS-ES observed cycle. Figure 14.2 shows the variation of the ratio $p_b f_b(\theta_b)/p_a f_a(\theta_a)$ for each of the eight location pairs corresponding to the eight pairs of observations on November 19, 2003. To extrapolate "p_b/p_a" (quotation marks serve to remind that the ratio is actually defined only for lunar phase angle 0°) observations to zero phase angle, a polynomial fit was done for all ratio values just before and after the Moon was within the Earth's penumbral shadow. Note that one set of points does not come close to the curves because this set was taken when the Moon was partly in Earth's shadow. For the lunar phase function, the values of Qiu et al. (2003) were used. After evaluating the phase function for the bands in Figure 14.1, it was found that the phase functions are all essentially the same after removing the ratio p_b/p_a , which provides the overall normalization.
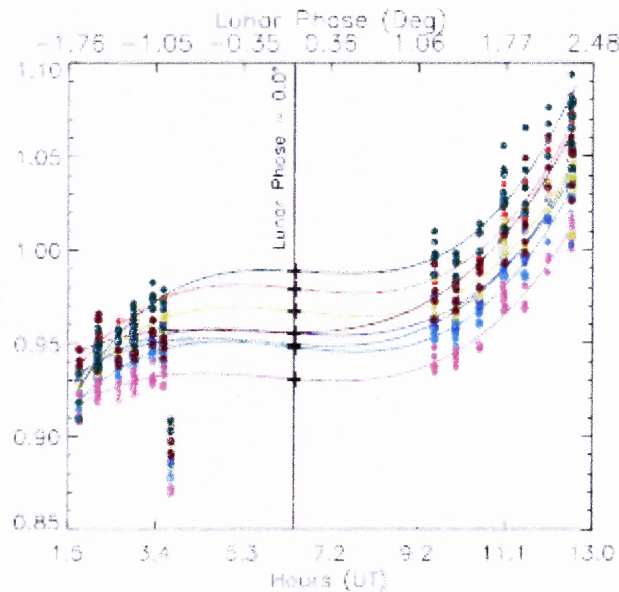
Figure 14.2 Variation of $p_b f_b / p_a f_a$ for all eight lunar patches (different colors) during the Nov. 29, 1993 eclipse. The ratio only takes its textbook meaning when the lunar phase angle is zero. The penumbral shadow region is shaded in the figure, and the best polynomial fit for each patch is also shown. The ratios at lunar phase equal to zero interpolated from each fit are given in Table 14.1. Penumbral shadowing causes one set of points to be well below the fitted lines.

14.4 Results

The atmospheric absorption bands in the Moonshine spectrum are formed when the Moonlight passes through the local atmosphere. The bands in the Earthshine spectrum additionally contain the absorption formed when the sunlight passes through the global terrestrial atmosphere twice, on the sunlit part of the Earth, before being reflected from the Moon toward the telescope. Thus, absorption lines in the ES spectrum are deeper than those in the MS spectrum (Montañés Rodriguez et al. 2004). Since the effect of the local atmosphere is present in both MS and ES, it is removed when the ratio ES/MS is calculated. In Figure 14.3, the Earth's atmospheric spectral features, primarily due to molecular oxygen and water vapor, are appreciable for the ES, MS, and their ratio. As one would expect, ES features are deeper than MS features, whereas lines formed in the

solar photosphere, such as Hα, remain invariant for ES and MS and therefore disappear in the ratio, which is further convincing evidence that the last pass through the atmosphere is also canceled out in the ratio. Only the cloud patterns in the global atmosphere will affect the shape of the ES/MS spectra by altering the optical path of the ES, depending on cloud altitudes and optical thicknesses.
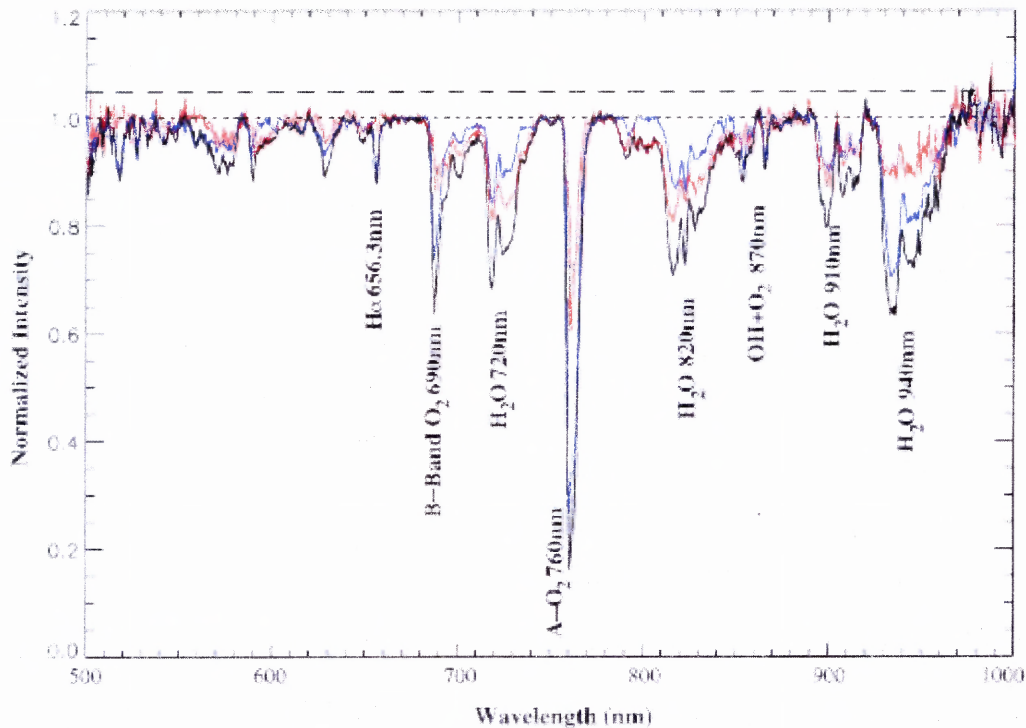
Figure 14.3 Normalized Moonshine spectra (blue), Earthshine (black), and their ratio (red) for Nov. 19, 2003. The main gas absorption bands as well as other features and their central wavelengths are indicated. Note how the solar Hα line disappears in the ES/MS ratio.

The measured apparent albedos, $p^*(\lambda)$, are shown in Figure 14.4, where different colors indicate its temporal evolution through the night, while different land and cloud distributions move into the sunlit side of the Earth and are visible from the Moon. During

the observing night, the Earth's spectral reflectance over the area shown in Figure 14.5 was monitored. Because ISCCP data are still not updated through 2003, cloud data for November 19, 2000 were used in the figure, for illustration. South America was only partially visible at 10.47 UT hr but was near the center of the sunlit area at 13.08 UT hr. The total covered area during the 2.6 hr of observations, without considering cloud cover, is composed of 79%–71% ocean, 8%–11% snow or ice covered areas, and 13%–18% land, 9%–14% of which are vegetated areas mainly located in the Amazon rain forest, equatorial Africa, and Europe. The range of percentages for each surface type corresponds to 10.00 and 13.00 UT hr, respectively.

The possibility of using the red-edge signature of vegetation as a tool to detect Earth-like extrasolar planets has been discussed in the literature. The red edge has been detected in surface spectral albedo measurements from airplanes at low altitude and from the Galileo spacecraft (Sagan et al. 1993); all these measurements were taken with some spatial resolution. The detected signal shows a step in the Earth's spectrum starting at about 720 *nm*, coinciding with an important water absorption band in the atmosphere, and continues to the near-infrared (Wendisch et al. 2004).

Woolf et al. (2002) observed the Earthshine on an evening in June 2001 (therefore they were monitoring the Pacific Ocean), and they report an inconclusive vegetation signature above 720 *nm*, although at the time of their observations no large vegetated area of the globe was visible from the Moon. More detailed observations of the Earthshine were undertaken by Arnold et al. (2002). They concluded in their study that the vegetation edge was difficult to measure in their Earthshine data due to clouds and the effect of atmospheric molecular absorption bands. One of the purposes in this work was

to confirm these results and to report any diurnal variability in the vegetation edge or other Earthshine signatures, if any.

During the night of November 19, 2003, there was found no notable red-edge enhancement, even at the times when the South American continent was in full view, or in November, when the "greenery" was abundant. This is not a surprise because one should expect some, if not all, of the vegetated areas contributing to the Earthshine to be obscured by the presence of clouds. When globally monitoring the Earth, one should note that at all times about 60% of the planet (Rossow et al. 1993) is covered by clouds, with a mean global cloud amount variation of about 10% from autumn to spring.
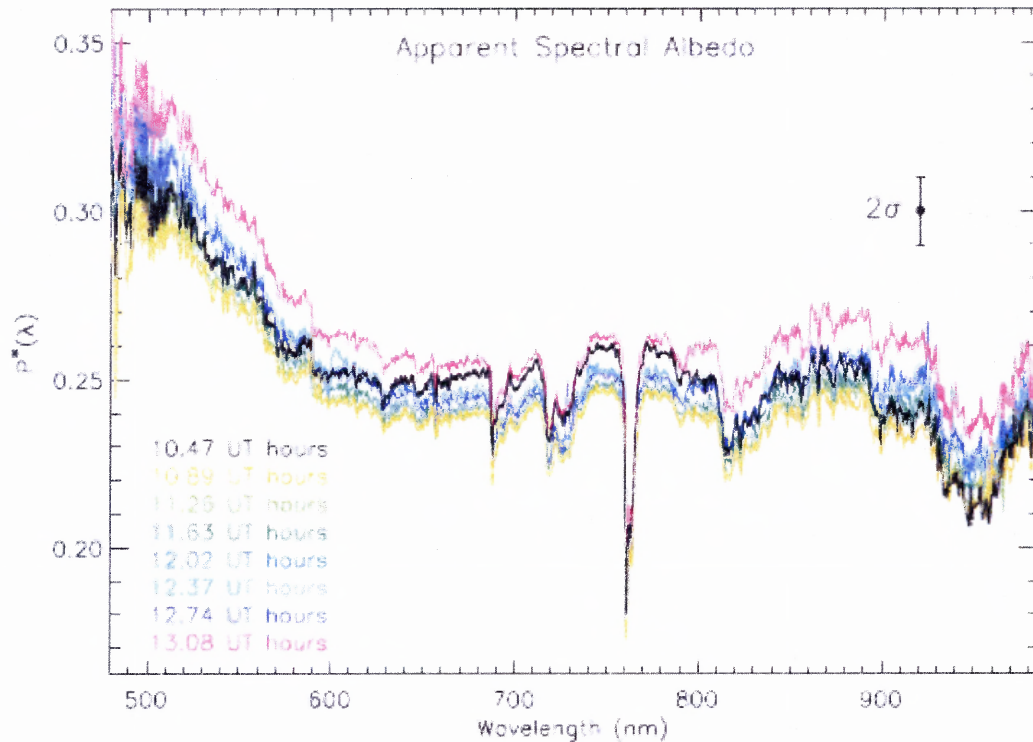
Figure 14.4 The apparent albedo p*(λ) for the night of observations. The main features of the Earth's reflectance in this region include an enhancement due to the Rayleigh scattering and part of the Chappuis O3 band in blue. Atmospheric absorption bands due to oxygen—the sharpest, A-O2 at 760 nm—and water vapor are clearly detected. The surface vegetation edge, which is expected to show an apparent bump in the visible albedo above 700 nm, is not strong, nor does it seem to vary appreciably or systematically throughout the night.

Thus, the possibility remains that the whole or a large part of the South American continent was covered by clouds at the time of observations, masking any vegetation signal. Mean monthly and annual cloud amounts from ISCCP indicate that this is frequently the case throughout the year (see http://isccp.giss.nasa.gov). This could easily be solved by analyzing cloud cover maps for the same night of the Palomar observations. If the night of November 19, 2003 had mostly clear skies over that area, then that would imply that the vegetation signal is too small to be detected in disk-integrated measurements of Earthshine. On the contrary, if it was mostly cloudy, the signal may be

strong enough to be detected if clear skies occur over a large enough portion of the rain forest regions of the Earth. However, this is not typically the case, as densely vegetated areas are associated with vegetation transpiration and enhanced cloud formation (Houghton et al. 2001).
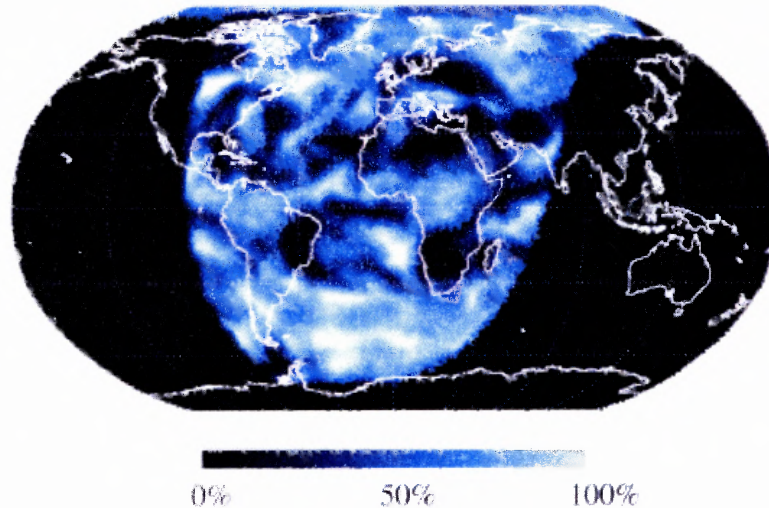

Figure 14.5 Earthshine contributing area of the Earth during morning observations from California on Nov. 19, 2003 (10.47–13.08 UT hr). The superimposed color map represents the mean cloud amount from ISCCP data over this area. Since ISCCP data for 2003 are not yet available, the cloud cover map for Nov. 19, 2000 (closest "equivalent" available) is shown here.

The enhancement of the reflectivity in the blue parts of the spectra, below 600 *nm*, due to the effect of atmospheric gas molecules producing Rayleigh scattering, is the most significant feature in the results. The albedo increase toward the blue is consistent with other surface spectral albedos measured from airplanes (Wendisch et al. 2004). From spatially resolved observations and spectral albedo models, a peak at around 310 *nm* would be expected if that spectral region were covered in the Palomar observations. This

is due to the combination of Rayleigh scattering, which decreases as λ^{-4}, and an ozone absorption.

An enhancement in the 600 to 900 *nm* region, or a decrease in the red and blue extremes of about 4% with respect to its mean spectral value, is found when one compares the first spectrum taken at 10.47 UT hr with the averaged temporal of the eight spectra (Figure 14.6). As can be seen in Figure 14.6, this relative bump systematically changes its curvature throughout the night (unlike for the 500–600 *nm* regime); thus, it cannot be attributed to any instrumental problem. Since the maximum enhancement is at the beginning of the night, when the Sun is still rising in South America, and it almost disappears two hours later, one cannot associate this enhancement with the signal of vegetation either, which should behave in the opposite fashion. Further, no signal of vegetation is expected below 700 *nm*. Thus, this variation is associated with the evolution of the surface and cloud pattern over the sunlit Earth during the time of observations.
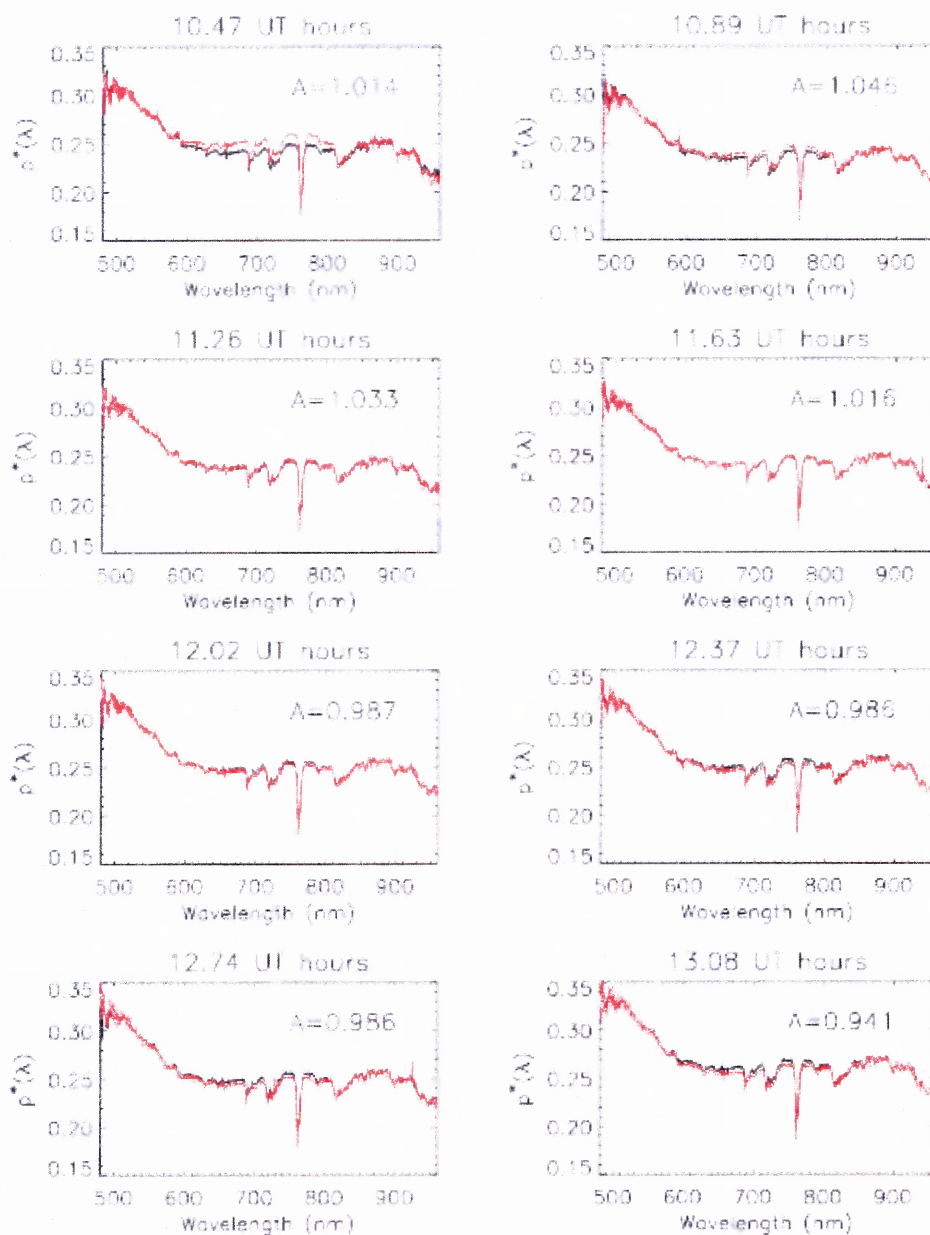
Figure 14.6 Apparent albedo p*(λ) as a function of wavelength taken during the night of observations (red). Also plotted is the mean spectrum for the night (black), <p(λ)>', the mathematical average of the eight p*(λ) spectra. The averaged spectra, p', has been artificially displaced by a factor A, also given in each panel, to match the mean value of each p*(λ) over the 500–550 nm interval. Note that for the first spectra, the observations were centered over Africa (top left panel), while the last observations were monitoring the Amazon rain forest (bottom right panel). A deviation from the mean value of up to 4% is appreciated in the first measurement.

14.5 Precision of Results

The accuracy of each $p^*(\beta,\lambda)$ derived from the Earthshine measurements was determined from Equation (2.13) and depends on the errors in the Earthshine to Moonshine ratio, the lunar reflectivity (which accounts for the relative reflectivity between two fiducial patches), the lunar phase function (which considers the geometrical dependence of the lunar reflectivity), and the opposition effect coefficient.

The measurement of the Earthshine-to-Moonshine ratio, after the sky subtraction and the Beer's law–fitting of the brightside spectra, is the biggest source of error, as can be seen in the photometric observations. It is estimated to be smaller than 2%. The error derived from the measurement of the (relative) lunar reflectivity was taken as the standard deviation of the polynomial fit to $p_b f_b(\theta_b)/p_a f_a(\theta_a)$, and has a value of 0.7% from a covariance calculation. The precision achieved for the lunar phase function (and opposition effect coefficient) can be determined down to 0.5%, as reported in Chapter 5. From the propagation of the errors into Equation (1.1), a standard deviation of the order of 3.7% is obtained for each individual spectral albedo measurement. This is shown in Figure 10.1 by a 2σ error bar. They are also represented for each data point in Figure 14.7

14.6 Comparison with Photometric Albedos

An evaluation of the results can be done with a comparison to photometric albedo measurements taken simultaneously at BBSO, and with effective albedo simulations for that night, following Palle' et al. (2003). To do that, each spectrum between 480 and 700 nm was averaged in wavelength. Photometric observations from BBSO cover the range between 400 and 700 nm, including a major part of the Rayleigh enhancement. The ES

simulations, however, cover the entire range of short-wavelength radiation, including ultraviolet, visible, and near-infrared (spanning 350 to 1500 *nm*).

Photometric observations at BBSO on November 19, 2003 were taken under a moderately hazy sky, which increases the light scattered by the Moonshine and causes a result that is too noisy for that night; however, on the following night, when the lunar crescent was smaller and the sky conditions clearer, the noise was substantially reduced. The retrieved photometric albedos, the spectrally averaged albedos, and computed photometric models are shown in Figure 14.7. Both sets of observations were linearly fitted showing a comparable increase from the beginning to the end of the night.

All of these results are regarded as being consistent because of the similarity of the increasing trend and because the offsets are those expected from the different wavelength coverage. In particular, the photometrically observed albedo includes more of the blue and less of the red, which would seem to account for that offset. Further, the simulations include much more of the IR, which roughly puts more weight toward an albedo of 0.25.
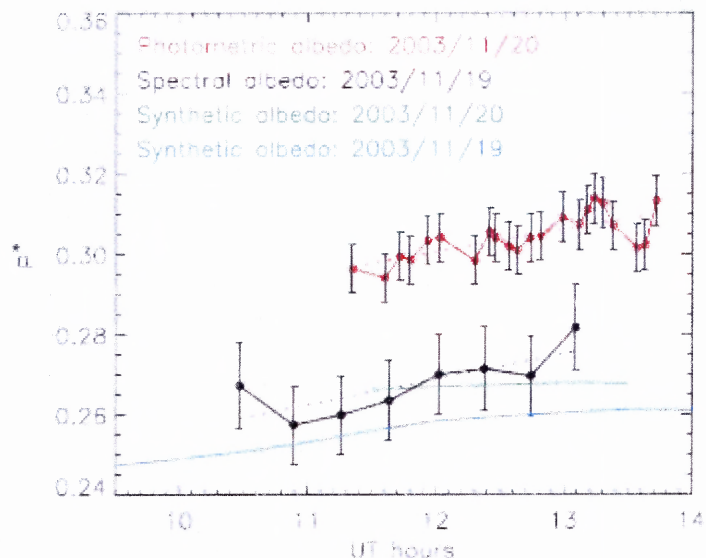
Figure 14.7 Temporal variation of the spectral albedo averaged between 480 and 700 nm (black solid line). The error bars show the 2σ deviation for each spectral measurement determined from the propagation of errors. A linear fit to all points throughout the night is also shown. The measured apparent albedos from photometric observations for a consecutive night are shown for comparison (red solid line), with error bars also representing twice the standard deviation achieved, but through photometry. Note that the spectral coverage for the photometric albedo is broader (between 400 and 700 nm) than for the spectral albedo. Also plotted are the modeled photometric albedos for Nov. 19, 2003 and Nov. 20, 2003 covering the entire short-wave region through the near-IR, using ISCCP data for Nov. 19, 2000 and Nov. 20, 2000 (blue and green, respectively). The differences in wavelength coverage probably account for much of the offsets.

14.7 Some Spectroscopic Conclusions

In Chapter 14, the ES group accurately determined the Earth's apparent, global spectroscopic albedo for the single night of November 19, 2003, as measured from Palomar Observatory in California. The main spectral features are shown derived from observations of the Earthshine spectrum in the visible region. The results are consistent with simultaneous photometric apparent albedo measurements from Big Bear Solar Observatory covering the same sunlit region of the Earth. The observations are also

consistent with the ES grooup albedo models using cloud patterns for the same day of the year, although for a different year due to the current unavailability of the necessary cloud cover data. The comparison with synthetic models of the Earth's spectrum that take into account a precise cloud cover pattern for the night, and its influence over surface and ocean distributions, will be carried out in future work. The measurements do not show any sign of vegetation red edge, at least for the night of November 19, 2003. If this result were confirmed with the analysis of subsequent Earthshine spectra taken at different seasons and the analysis of simultaneous cloud maps, it would strongly limit efforts to use the red edge as a probe for Earth-like extrasolar planets. It must be emphasized, however, that other features on the Earthshine spectra may still provide a powerful probe.

Observations of the Earthshine at different seasons are desirable not only to study other indirect biological signatures, such as the seasonal change of global abundances of oxygen, water vapor, carbon dioxide, or methane, but also for a better understanding of the influence of these species on the Earth's albedo and climate. Results derived from future observations of the Earthshine will be invaluable in the search for terrestrial-like extrasolar planets, in particular, the search of planetary atmospheres in chemical disequilibrium (as proposed by Hitchcock & Lovelock 1967).

CHAPTER 15

SOME CONCLUSIONS AND ACKNOWLEDGEMENTS

In this paper, the author has described in some detail the methods followed during the Earthshine group observations, modeling, and analysis conducted during the author's time at Big Bear Solar and Palomar Observatories. There is of course much more to tell about Earthshine research, past and future. However to keep this thesis at manageable length The author has omitted many details including, more instrumentation details, more modeling concerns, the evolving global Earthshine network, and future possible IR spectral observations, just to name a few.

The ES group has proven that one can derive the Earth's albedo photometrically down to an accuracy of 1%. It has also been shown that the albedos determined by the observations are as precise as those of satellites. The group has accurately determined the Earth's global spectroscopic albedo for a single night, which was consistent with simultaneous photometric observations. These and other achievements have given the climate field new, inexpensive, and powerful tools for future investigations.

In completion of this thesis the author has borrowed heavily from the work of the other members of the Earthshine team. While the author has been an active participant in the Earthshine observations, one must be fair and acknowledge that the author's role was minor compared to the insights and hard work of a large number of people. As they are probably the only ones who might read this document, it is fitting to name them. In no particular order; Phil Goode, Steve Koonin, Jiong Qiu, Vasyl Yurchyshyn, Pilar Montañés Rodriguez, Enric Palle', Titus Brown, and Bill Marquette. It has been a pleasure.

REFERENCES

1. Allen, C. W., *Astrophysical Quantities*, A.N. Cox (ed), AIP Press (Springer-Verlag), New York, ISBN 0- 387-98746-0, p.125, 1973.

2. Arnold, L., s. Gillet, O. Lardiere, P. Riaud, J. Schneider, A test for the search for life on extrasolar planets, *Astronomy & Astrophysics*, 392, 231-237, 2002.

3. Betts, R.A., Offset of the potential carbon sink from boreal forestation by decreases in surface albedo, *Nature,* 408, 187-190, 2000.

4. Buratti, B.J., J.K. Hillier, and M. Wang, *Icarus*, 124, 490-499, 1996.

5. Cess, R.D., and 33 co-authors, Cloud feedback in atmospheric general circulation models: an update, *Journal of Geophysical Research,* 101(D8), 12791-12794, 1996.

6. Charlson, R.J., S.E. Schwartz, J.M. Hales, R.D. Cess, J.A. Coakley Jr, J.E. Hansen, D.J. Hofmann, Climate forcing by anthropogenic aerosols, *Science*, 255, 423-430, 1992.

7. Danjon, A., Recherches sur la photométrie de la lumière cendrée et l'albedo de la terre, *Ann. Obs. Strasbourg*, 2, 165-180, 1928.

8. Danjon, A., Albedo, color, and polarization of the Earth, *The Earth as a Planet*, ed. Kuiper, Chicago, 726-738, 1954.

9. Dubois, J., Le photométre à oeil-de-chat et ses applicatons, *Ciel et Terre*, 58, 350-361, 1942.

10. Dubois, J., Sur l'albedo de la terre, *Bull. Astron.*, 13, 193-196, 1947.

11. Eddy, J., The Maunder Minimum, *Science*, 192, 1189-1202, 1976.

12. ERBE Data Management Team, ERBE Data Management System, Earth Radiant Flux and Albedo, Scanner S-9, Nonscanner S-10 *User's Guides*. NASA/Langley, Hampton, Virginia, 1985.

13. Flatte, S., S.E. Koonin., and G. MacDonald, *Global Change and the Dark of the Moon*, JSR-91-315 (McLean, VA: The MITRE Corporation), 1991.

14. Franklin, F.A., Two-Color Photometry of the Earthshine, *J.Geophys.Res.*, 72, 2963-2967, 1967.

15. Fritz, S., The albedo of the planet Earth and of clouds, *J. Meteor.*, 6, 277-282, 1949.

16. Fröhlich, C., Observations of irradiance variations, *Space Science Reviews*, v. 94, 15, 2000.

17. Gibson, G. G., F.M. Denn, D.W. Young, E.F. Harrison, P. Minnis, B.R. Barkstrom, O.C. Smith, D.J. Travers, Characteristics of the Earth's radiation budget derived from the first year of data from the Earth Radiation Budget Experiment, *SPIE*, 1299, 253-256, 1990.

18. Goode, P.R., Internal rotation and structure of the sun, *ESA SP-376*, 121-136, 1995.

19. Goode, P.R., J. Qiu, V. Yurchyshyn, J. Hickey, M.C. Chu, E. Kolbe, C.T. Brown, and S.E. Koonin, Earthshine observations of the Earth's reflectance, *Geophys. Res. Lett.*, 28 (9), 1671-1674, 2001.

20. Hapke, B., *Physics and Astronomy of the Moon*, 2nd edition, ed. Z. Kopal, Academic Press, New York, 155, 1971.

21. Hapke, B.W., R.M. Nelson, and W.D. Smythe, The opposition effect of the Moon - the contribution of coherent backscatter, *Science*, 260, 509-511, 1993.

22. Hapke, B., R. Nelson, and W. Smythe, The opposition effect of the Moon: coherent backscatter and shadow hiding, *Icarus*, 133, 89-97, 1998.

23. Harrison, E. F., P. Minnis, B. R. Barkstrom, V. Ramanathan, R. D. Cess, and G.G. Gibson, Seasonal variation of cloud radiative forcing derived from the Earth Radiation Budget Experiment, *Journal of Geophysical Research*, 95, 18687-18703, 1990.

24. Helfenstein, P., Veverka, J., and Hillier, J., The lunar opposition effect: A test of alternative models, *Icarus*, 128, 2-14, 1997.

25. Hitchcock, D. R., & Lovelock, J. E., *Icarus*, 7, 194, 1967.

26. Houghton, J. T., et al., *Climate Change 2001*, Cambridge University Press, Cambridge, 944, 2001.

27. Houghton, J., *The physics of atmospheres*, 3rd edition, Cambridge University Press, Cambridge, 320, 2002.

28. Huffman, D., C. Weidman, and S. Twomey, *Colloq Andre Danjon*, Jounées 1990, Capitaine and S. Débarbat, eds. (Paris: Paris Observatory), 111, 1990.

29. Intergovernmental Panel on Climate Change (IPCC), Climate Change 1992, *Suppl. Rep IPCC Sci. Assess*, ed. J.T. Houghton, B.A. Callender, S.K. Varney, Cambridge, MA: Cambridge University Press, 1992.

30. Intergovernmental Panel on Climate Change (IPCC), 1995, Climate Change 1994, *Radiative Forcing of Climate Change and an Evaluation of the IPCC 1992*

Emission Scenarios, ed. J.T. Houghton, L.G. Meira Filho, J. Bruce, H. Lee, B.A. Callender, E. Haites, N. Harris, K. Maskell, Cambridge, MA: Cambridge University Press, 1994.

31. Jayne, S.R., and J. Marotzke, The Dynamics of Ocean Heat Transport Variability, *Reviews of Geophysics*, 39, 385-411, 2001.

32. Kato, S., N.G. Loeb, and C.K. Rutledge, Estimate of top-of-atmosphere albedo for a molecular atmosphere over ocean using Clouds and the Earth's Radiant Energy System measurements, *Journal of Geophysical Research*, 107 (D19), 4396, doi:10.1029/2001JD001309, 2002.

33. Kennedy, J.R., M.S. Thesis, Fresno State College, unpublished, 1969.

34. Lean, J., The sun's variable radiation and its relevance for Earth, *Ann. Rev. Astron.*, 35, 33, 1997.

35. Liou, K.N., An introduction to atmospheric radiation, second edition, *International Geophysics series}*, eds. R. Dmowsca, J.R. Holton and H.T. Rossby, Academic Press, Elsevier Science, 80, 2002.

36. Lockwood, M., 2002, private communication.

37. Loeb, G.L., N. Manalo-Smith, S. Kato, W.F. Miller, S.K. Gupta, P. Minnis, and B.A. Wielicki, Angular distribution models for top-of-atmosphere radiative flux estimation from the clouds and the Earth's radiant energy system instrument on the tropical rainfall measuring mission satellite. Part I: Methodology, *Journal of Applied Meteorology*, 42, 240-265, 2003.

38. Montañés Rodriguez, P., et al., 293, *Adv. Space Res.*, 34, 2004

39. Pallé, E., P.R. Goode., V. Yurchyshyn, J. Qiu, J. Hickey, P. Montañés Rodriguez, M.C. Chu, E. Kolbe, C.T. Brown, and S.E. Koonin, Earthshine and the Earth's albedo II: Observations and simulations over three years, *J. Geophys. Res.*, 108, ACL 13-1, 2003.

40. Palle′, E., Goode, P. R., Montañés Rodriguez, P., & Koonin, S. E., *Science,* 304, 1299, 2004.

41. Palle. , *Adv. Space Res.*, 34, 288, 2004.

42. Qiu, J., P.R. Goode, E. Pallé, V. Yurchyshyn, J. Hickey, P. Montañés Rodriguez, M.C. Chu, E. Kolbe, C.T. Brown, and S.E. Koonin, Earthshine and the Earth's albedo I: Precise and large-scale nightly measurements, *J. Geophys. Res.*, 108, ACL 12-1, 2003.

43. Randall, D.A., and 26 more authors, Analysis of snow feedbacks in 14 general circulation models, *Journal of Geophysical Research*, 99(D10), 20757-20771, 1994.

44. Ram, M., and M.R. Stoltz, Possible solar influences on the dust profile of the GISP2 ice core from Central Greenland, *Geophys. Res. Lett.*, 26, No. 12, 1763, 1999.

45. Ramanathan, V., R. D. Cess, E. F. Harrison, P. Minnis, B. R. Barkstrom, E. Ahmad, and D. Hartmann, Cloud-Radiative Forcing and Climate: Results from the Earth Radiation Budget Experiment, *Science*, 243, 57-63, 1989.

46. Raval, A., and V. Ramanathan, Observational determination of the greenhouse effect, *Nature*, 342, 758-761, 1989.

47. Ridley J., Variations in planetary albedos', *4th annual ROE Workshop*, Royal Observatory Edinburgh, ed W.R.F. Kent, 2001.

48. Rossow, W. B., Walker, A. W., & Garder, L. C. , 2394, *J. Climate*, 6, 1993.

49. Rossow, W. B., A. W. Walker, D. E. Beuschel, and M. D. Roiter, International Satellite Cloud Climatology Project (ISCCP): Documentation of New Cloud Datasets, *WMO/TD-No. 737*, World Meteorological Organization, Geneva, 115, 1996.

50. Sagan, C., Thompson,W. R., Carlson, R., Gurnett, D., & Hord, C., *Nature*, 365, 715, 1993.

51. Suttles, J.T., R.N. Green, P. Minnis, G.L. Smith, W.G. Staylor, B.A. Wielicki, I.J. Walker, V.R. Young, and L.L. Stowe, Angular Radiation Models for Earth-Atmosphere Systems, *Vol. I: Shortwave Radiation, NASA Reference Publication RP-1184*, 26, 1988.

52. Tikhoff, G.A., *Mitteilungen der Nikolai-Hauptsternwarte zu Pulkovo*, No. 62, Band VI_2, 15, 1914.

53. Wendisch, M., et al., D08203, *J. Geophys. Res.*, 109, 2004.

54. Wielicki, B.A., and R.N. Green, Cloud identification for ERBE radiative flux retrieval, *Journal of Applied Meteorology*, vol 28, no 11, 1133-1146, 1989.

55. Willson, R.C. and H.S. Hudson, Solar luminosity variations in solar cycle-21, *Nature*, 332, 810, 1988.

56. Willson, R.C. and H.S. Hudson, The suns luminosity over a complete solar-cycle 1991, *Nature,* 351, 42, 1991.

57. Woolf, N.J., P.S. Smith, W.A. Traub, and K.W. Jucks, The Spectrum of Earthshine: A Pale Blue Dot Observed from the Ground, *Astrophysical Journal*, 574, 430-433, 2002.